The Dissertation Committee for Nicholas John Whitelonis Certifies that this is the approved version of the following dissertation:

Investigation of High-Frequency Propagation Channels Through Pipes and Ducts for Building Interior Reconnaissance

Committee:

Hao Ling, Supervisor

Andrea Alù

Dean Neikirk

Edward Powers

Preston Wilson

Investigation of High-Frequency Propagation Channels Through Pipes and Ducts for Building Interior Reconnaissance

by

Nicholas John Whitelonis, B.S.E.E.; M.S.E.

Dissertation

Presented to the Faculty of the Graduate School of

The University of Texas at Austin

in Partial Fulfillment

of the Requirements

for the Degree of

Doctor of Philosophy

The University of Texas at Austin

May 2012

Acknowledgements

Many people have been integral to the success of this dissertation. I should thank everyone in my life, as I have yet to meet anyone who has discouraged my pursuit of a PhD. However, here I would like to thank those who have made a direct contribution to this dissertation. First, I would like to thank my supervisor and mentor, Dr. Hao Ling, for his contribution. His teaching, guidance, patience, and encouragement have been enlightening and motivating. Dr. Ling's support was critical to the success of this dissertation, and for that I will always be grateful. I would also like to thank my committee members Dr. Dean Neikirk, Dr. Edward Powers, Dr. Andrea Alù, and Dr. Preston Wilson for their contributions and helpful suggestions.

I would also like to acknowledge my fellow research group members over the years: Dr. Adrian Lin, Dr. Yang Li, Mr. Ick-Jae Yoon, Mr. Shang-Te Yang, and Mr. Aale Naqvi. Their questions and comments have given me perspective, their discussions have always inspired, and their help has been invaluable.

Last, I would like to thank my parents, Christine and Michael, for all of the support they have provided for my education. Finally, thanks to my fiancée, Amanda, for her love, support, and patience while I pursued my PhD.

NICHOLAS JOHN WHITELONIS

The University of Texas at Austin

May 2012

Investigation of High-Frequency Propagation Channels Through Pipes and Ducts for Building Interior Reconnaissance

Nicholas John Whitelonis, Ph.D.

The University of Texas at Austin, 2012

Supervisor: Hao Ling

Recently, there is strong interest in the through-wall sensing capabilities of radar for use in law enforcement, search and rescue, and urban military operations. Due to the high attenuation of walls, through-wall radar typically operates in the low GHz frequency region, where resolution is limited. It is worthwhile to explore other means of propagating radar waves into and back out of a building's interior for sensing applications. One possibility is through duct-like structures that are commonly found in a building, such as metal pipes used for plumbing or air conditioning ducts. The objective of this dissertation is to investigate techniques to acquire radar images of targets through a pipe.

First, using the pipe as an electromagnetic propagation channel is studied. A modal approach previously developed for computing the radar cross-section of a circular duct is modified to compute the transmission through a pipe. This modal approach for transmission is validated against measured data. It is also shown that a pipe is a high-pass propagation channel. The modal analysis is then extended to two-way, through-pipe propagation for backscattering analysis. The backscattering from a target is observed through a pipe in simulation and measurement.

Next, methods to form two-dimensional radar images from backscattering data collected through a pipe are explored. Four different methods previously developed for free-space imaging are applied to the problem of imaging through a pipe: beamforming, matched filter processing, MUSIC, and compressed sensing. In all four methods it is necessary to take into account the propagation through the pipe in order to properly generate a focused radar image. Each method is demonstrated using simulation and validated against measurement data. The beamforming and matched filter methods are found to suffer from poor cross-range resolution. To improve resolution, the MUSIC algorithm is applied and shown to give superior resolution at the expense of more complicated data collection. The final method, compressed sensing, is shown to achieve good cross-range resolution with simpler data collection. A comparison of the tradeoffs between the four methods is summarized and discussed.

Two additional extensions are studied. First, a method for computing the transmission through an arbitrary pipe network using the generalized scattering matrix approach is proposed and implemented. Second, a new method for computing joint time-frequency distributions based on compressed sensing is applied to analyze the backscattering phenomenology from a pipe.

Table of Contents

List of Tables

List of Figures

Chapter 1: Introduction

There is a continuing interest in the capabilities of through-wall radar for use in law enforcement, search and rescue, and urban military operations [1]. Research in the field of through-wall radar has focused on the development of radar systems [2]-[9], propagation characterization of different walls [10]-[16], and mitigation of wall effects in radar imaging [17]-[20]. Ultra wideband (UWB) pulsed radar systems and continuous-wave (CW) Doppler radar have been demonstrated for through-wall operation [2]-[9]. UWB is advantageous in that the wideband signal provides good down range resolution. Doppler radar has the advantage that it only responds to moving objects within a building, such as people. In the study of propagation through walls it has been found that walls are quite lossy at higher frequencies, therefore walls are considered to be low-pass filters [10]. This has limited the operation of both CW Doppler and UWB radar systems to frequencies in the low GHz region. Operating at these lower frequencies allows propagation through the wall at the expense of cross-range resolution and Doppler sensitivity due to the low carrier frequency. Loss caused by walls is compounded when propagating through multiple walls, which limits the depth of penetration possible for through-wall radar. In addition to the wall attenuation, it has been found that walls also cause phase distortion [11]. Some efforts have been devoted to the mitigation of the distortion effects of walls in radar imagery [17]-[20]. Improved images were obtained by using a propagation model that better describes through-wall propagation in comparison to those based on free space propagation models. Due to the inherent limitations when

trying to image building interiors through walls, it would be worthwhile to explore alternate channels that overcome the low resolution and limited depth of penetration caused by through-wall propagation. It is known that waveguide-like structures such as pipes and ducts behave as high-pass, low-loss transmission channels. Therefore it would be useful to explore the potential of using existing infrastructure that resemble waveguides such as heating, ventilation, and air conditioning (HVAC) ducts to gain building interior information rather than attempting to propagate through the wall. The benefits would be that the radar system could operate at a higher frequency with more available bandwidth for improved resolution in cross-range, down-range, and Doppler; and the guidance of the electromagnetic waves offered by the ducts would provide deeper penetration into buildings. A recent study was performed to explore the feasibility of using HVAC systems to propagate wireless signals throughout a building for improved wireless communication coverage [21]. However in their proposed system a transceiver would be placed on each opening of the HVAC duct, which would not be possible in an uncooperative building reconnaissance scenario.

Original interest in propagation through metallic pipes was motivated by the desire for electromagnetic communication channels. Oliver Heaviside first considered the propagation of electromagnetic waves through a hollow metal tube in 1893 [22]. However, he dismissed the notion because he was convinced that guidance of electric and magnetic fields required two conductors. Later, in 1897, Lord Rayleigh predicted the existence of electromagnetic propagation inside a hollow metal cylinder [23]. In addition, Rayleigh showed that the fields inside the cylinder could be decomposed into an infinite

set of modes with transverse electric (TE) and transverse magnetic (TM) fields. Rayleigh also predicted the frequency cutoff phenomena of the modes and noted that propagation required high-frequency radiation and relegated the notion to scientific pondering due to the frequency limitations of sources at the time. Rayleigh's work on propagation through hollow metal cylinders was forgotten until 1936 when it was rediscovered by two independent researchers, G. C. Southworth at Bell Laboratory and W. L. Barrow at MIT [24]. Due to advances in electromagnetic sources, they were each able to experimentally verify the existence of propagation through hollow metal pipes. Barrow was studying feeds for horn antennas and Southworth was interested in the application of waveguides for communications. During World War II much effort was put into waveguides and most radar systems developed included waveguide devices. Their application as circuit devices in radio frequency applications was extensively studied as well as the radiation from waveguides. After the war, this work was published as volumes 10 [25] and 12 [26] of the Radiation Laboratory series by Marcuvitz and Silver respectively. After the war Bell Labs continued looking into waveguides as a communication channel [27], however this concept was eventually abandoned.

Subsequently, much of the work on the subject of electromagnetic propagation in pipes and ducts was focused on studying the radar cross section (RCS). Motivated by the study of scattering from jet engine intakes, there have been extensive studies of open-ended ducts. Unfortunately, there is very limited information from the literature on ducts with two open ends. As early as 1968 a semi-infinite circular duct was used to model the intake of a jet engine [28]. An open-ended circular duct was used because the geometry is

simple and an exact closed-form solution for the backscattering could be obtained using the Wiener-Hopf technique [29]. The limitation of the exact solution was that the final result was too complex to be useful given the numerical capabilities at the time. Chuang, Liang, and Lee later derived an asymptotic approximate of the Wiener-Hopf solution in the high frequency limit [30]. In the asymptotic expansion only the first and second order terms were considered, which reduced the numerical burden of the solution. In 1982 Johnson and Moffatt compared the approximate solutions of Wiener-Hopf to exact numerical computations [31]. At around the same time, Medgyesi-Mitschang and Eftimiu solved a finite circular pipe using the method of moments (MoM) with a body of revolution basis for modeling the pipe [32]. In 1983 Huang introduced a method for solving the backscatter from a circular duct by expanding the incident field in terms of the modes for a circular waveguide [33]. The modal expansion method based on Huang's work could be applied to any duct that behaved as a waveguide and maintained a constant cross-section. Burkholder, Chuang, and Pathak used a hybrid modal method and moment method technique to compute the backscatter from tapered ducts [34]. Later, Burkholder used a hybrid mode-asymptotic technique to solve for the backscatter from waveguide ducts with bends [35]. Boonzaaier and Malherbe developed a model for the termination at the backend of a duct that better represented what would be found in a jet engine intake [36].

In the late 1980's, advances in computational methods for approximating the backscatter from ducts allowed researchers to analyze structures other than waveguide type structures. In 1989 a new technique to compute the RCS from a duct or cavity was

presented by Ling, Chou, and Lee [37]. The technique, referred to as shooting and bouncing rays (SBR), uses ray tracing to account for multiple bounces inside the duct structures and then applies physical optics on the rays exiting the duct to compute the backscatter. The SBR technique was useful for high-frequency scattering and arbitrary cavities and ducts, but deviated from experimental results at low frequencies where modal methods had been successful in the past [38]. The generalized ray expansion (GRE) method was subsequently proposed to improve the accuracy of SBR [39]. The work done in the late 1980's allowed for high fidelity modeling of intakes on different aircraft.

Despite the extensive work done on the computation and measurement of backscattering from pipes and ducts there has been limited work done on transmission through pipes and ducts. The research here will address the feasibility of obtaining building interior information by propagating an electromagnetic signal through waveguide-like structures such as HVAC ductwork. Previously, it was shown that a waveguide does indeed act as a high frequency propagation channel especially in comparison to walls [40]. It was also shown that a target on the other side of the pipe could be detected through the pipe. Continuing from this original work, imaging techniques used for free space imaging will be adapted for imaging through waveguide-like channels. The goal of this research is to develop methods for obtaining radar images through complex waveguide channels. Techniques will be developed in such a way that they could potentially be applied to a real-world HVAC system to obtain building interior information remotely. However, while building interior reconnaissance is stated as the

motivating factor, the techniques and methods developed in this research can be applied to any data collection scenario that propagates a signal through a complex waveguide-like channel. Other potential applications may include search and rescue in mines and tunnels, and mapping out caves and underground facilities.

In this dissertation, the potential of radar imaging using a circular metal pipe as the propagation channel is explored. The remainder of this dissertation is divided into 8 chapters. In Chapter 2 the methods used for simulating transmission and backscattering through a pipe are presented. The following four chapters discuss different methods for imaging through a pipe. In Chapter 3 a method using beamforming is developed. Chapter 4 shows how matched filter processing can be used for imaging through a pipe. Chapters 5 and 6 discuss advanced imaging procedures using MUSIC and compressed sensing (CS) respectively. Chapter 7 describes a technique for computing the transmission through an arbitrary pipe structure using the generalized scattering matrix and shows results obtained from the technique. Chapter 8 discusses a new joint time-frequency distribution based on CS. This new time-frequency distribution can be applied to analyze backscattering phenomenology from a pipe. The final chapter presents conclusions and discusses potential future studies that could follow from the work presented here.

Chapter 2: Analysis of Electromagnetic Transmission Through a Pipe

2.1 INTRODUCTION

Substantial research has been reported on the backscattering from a circular pipe that is open on one end and terminated at the other end. As mentioned above, this structure served as a model for jet engine intakes, and was of great interest to the radar signature community throughout the 1980s. Despite the extensive work done on the scattering from pipes with one open end, little has been reported in the literature about pipes that have two open ends. Mitschang and Putman solved a pipe with two open ends using the method of moments [41]. However the pipe was electrically small and the solution was done for the purpose of code validation.

In this chapter a method is developed for computing the transmission through a conducting circular pipe with two open ends. The remainder of this chapter is divided into five sections. In Section 2.2 a mode-based analysis approach is presented to characterize wideband transmission through a pipe. The transmission analysis considers the pipe as a circular waveguide, and the modal approach previously used by Huang [33] for computing backscattering from a circular pipe with a closed termination is extended to solve for the transmission through a circular pipe with two open ends. Then, in Section 2.3, the transmission computed using the mode-based method is compared with measurement data. In Section 2.4 the mode-based method is extended in order to compute the backscattering of a target through a pipe. Section 2.5 shows simulation and

measurement results for backscattering collected through a pipe. The 6th and final section discusses conclusions.

2.2 TRANSMISSION THROUGH A PIPE

To begin, an analysis of the circular pipe as a transmission channel is developed. As previously mentioned, much of the research done on the electromagnetic propagation through pipes and ducts was devoted to determining the RCS of the structure. Fig. 2.1 shows the geometry of a straight open-ended pipe that is open on one end and closed on the other. Huang showed that the RCS of the pipe in Fig. 2.1 could be solved by expanding the incident plane-wave in terms of the propagating modes supported by the pipe, propagating the modes down the pipe and back to the open end, and then radiating the modes back into free space to calculate the backscattering [33].

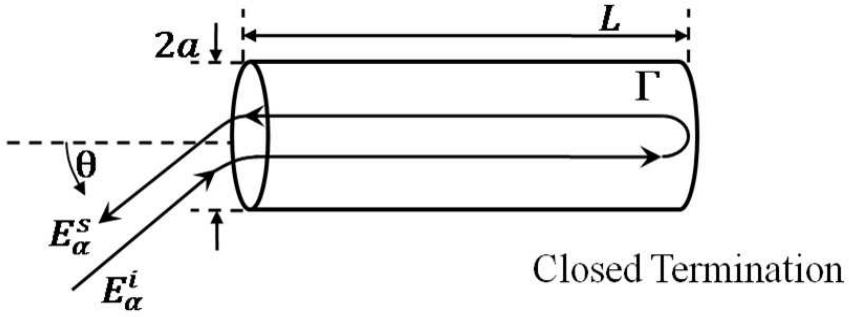

Figure 2.1: Pipe geometry with closed termination used for RCS analysis.

In order to solve for the transmission through a circular pipe the geometry in Fig. 2.1 is modified as shown in Fig. 2.2. By using Huang's approach and ignoring higher order interactions between the two ends of pipe the transmission through the pipe can be

solved in three steps. 1) The incident field E_α^i, where α represents either φ-polarization or θ-polarization, is expanded in terms of the right-traveling propagating circular waveguide modes supported by the pipe geometry. That is, the coupling of the incident field into the waveguide modes is computed. 2) The modes are propagated from the left end of the pipe to the right end. 3) Each mode is radiated into free space on the right. The total transmitted field E_α^{tx} is the superposition of the radiation from each mode.

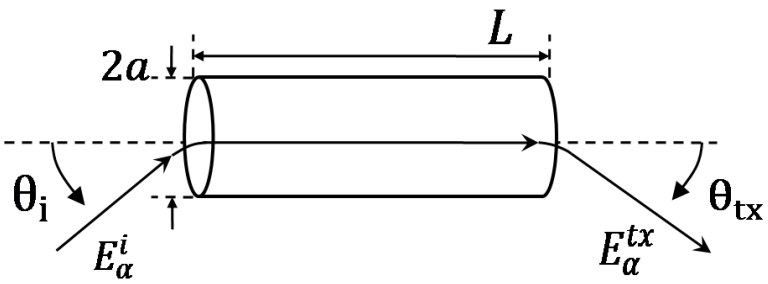

Figure 2.2: Pipe geometry with two open ends used for transmission analysis.

Here the details of each step in the analysis procedure are discussed. To begin, the pipe is considered to be an over-moded circular waveguide. The set of TE modes inside the pipe are defined as follows:

$$H_z = \beta_\rho^2 \cos m\varphi' J_m(\beta_\rho \rho) e^{-j\beta_z z}, \quad E_z = 0 \tag{2.1}$$

$$H_\rho = -\left(\frac{\beta_z}{\omega\mu}\right) E_\varphi = -j\beta_z \beta_\rho \cos m\varphi' J_m'(\beta_\rho \rho) e^{-j\beta_z z} \tag{2.2}$$

$$H_\varphi = \left(\frac{\beta_z}{\omega\mu}\right) E_\rho = \left(\frac{j\beta_z m}{\rho}\right) \sin m\varphi' J_m(\beta_\rho \rho) e^{-j\beta_z z} \tag{2.3}$$

where $\omega^2\mu\epsilon = \beta_\rho^2 + \beta_z^2$, $\beta_\rho = \chi'_{mn}/a$, and χ'_{mn} is the nth zero of the derivative of the mth order Bessel function of the first kind. There also exists a set of TM modes, but the discussion will first be limited to the TE modes. In the first step of the analysis the strength of the propagating modes excited by an impinging plane wave is sought. A useful method to solve this problem is through reciprocity as shown by Johnson and Moffatt [31]. The coupling problem is shown in Fig. 2.3(a) where the strength of the modes A'_{mn} is sought. The reciprocal problem, which is the radiation problem, is shown in Fig. 2.3(b), where the strength of the mode is known and the resulting plane wave is sought.

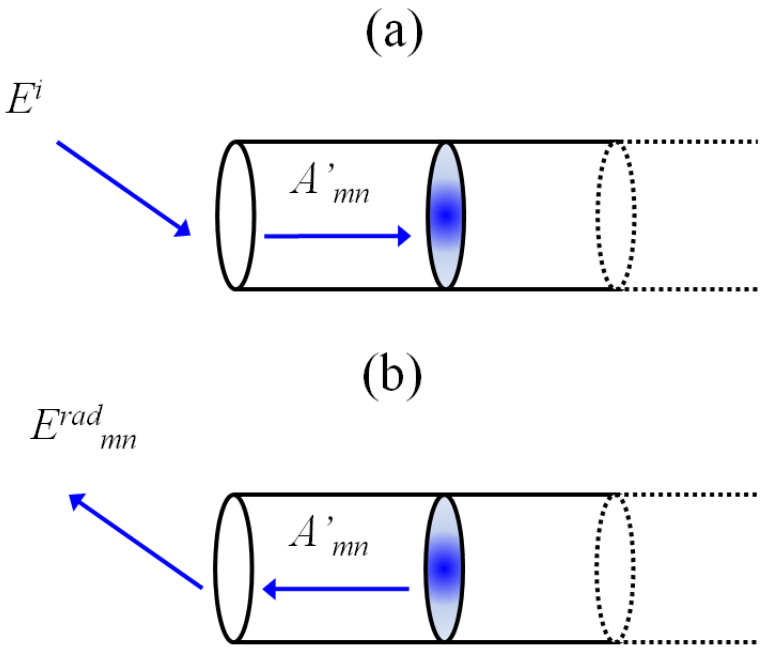

Figure 2.3: Reciprocity formulation for pipe: (a) coupling problem (b) radiation problem.

The radiation problem, Fig. 2.3(b), has an approximate closed-form solution that is valid for electrically large pipes [42][26]. The radiation of the modes from the pipe

opening is determined through the standard Kirchhoff approximation using the Stratton-Chu integral [42]. For TE modes the resulting radiation is

$$E_{\varphi,mn}^{rad} = A_{mn} \cdot j^{m+1} \frac{ka\omega\mu}{2} \left(\frac{\beta_z}{k} + \cos\theta_{tx} \right) \frac{\mathrm{J_m}(\beta_\rho a)\, \mathrm{J'_m}(ka \sin\theta_{tx})}{1 - (k \sin\theta_{tx}/\beta_\rho)^2} \cos m\varphi \frac{e^{-jkr}}{r} \tag{2.4}$$

$$E_{\theta,mn}^{rad} = A_{mn} \cdot j^{m+1} \frac{m\omega\mu}{2} \left(1 + \frac{\beta_z}{k} \cos\theta_{tx} \right) \frac{\mathrm{J_m}(\beta_\rho a)\mathrm{J_m}(ka \sin\theta_{tx})}{\sin\theta_{tx}} \sin m\varphi \frac{e^{-jkr}}{r} \tag{2.5}$$

where k is the free space propagation constant, $(r, \varphi, \theta_{tx})$ are the free-space coordinates of the observer, $E_{\varphi,mn}^{rad}$ is the φ-polarized radiated electric field, and $E_{\theta,mn}^{rad}$ is the θ-polarized radiated electric field. Reciprocity is applied by assuming the impinging plane wave in Fig. 2.3(b) is excited by an infinitesimal dipole source and the strength of the modes in the radiation problem, $\mathrm{A_{mn}}$, is unity. Using the solutions in (2.4) and (2.5) for the radiation from the pipe and applying reciprocity results in the following equation:

$$(I_\alpha \Delta l) E_{\alpha,mn}^{rad} = -2A'_{\alpha,mn} \iint_{\Sigma} \left(\bar{E}_{t,mn} \times \bar{H}_{t,mn} \right) \cdot \hat{z}\, ds \tag{2.6}$$

where Σ is the cross-sectional surface of the pipe, $\bar{E}_{t,mn}$ and $\bar{H}_{t,mn}$ are the transverse electric and magnetic fields of the $\mathrm{TE_{mn}}$ mode ((2.2) & (2.3)), and $I\Delta l$ is the infinitesimal dipole source that generates the incident field E_α^i. The strength of the field radiated by the infinitesimal dipole is

$$I_\alpha \Delta l = \frac{4\pi r e^{jkr}}{jk\eta} E_\alpha^i. \tag{2.7}$$

Plugging (2.7) into (2.6) and solving for $A'_{\alpha,mn}$ yields a solution for the strength of the modes excited by a φ-polarized plane wave

$$A'_{\varphi,mn} = E_\varphi^i \cdot j^m \frac{2a}{\eta\beta_z \epsilon_{0m} \mathrm{J_m}(\beta_\rho a)\left((\beta_\rho a)^2 + m^2\right)}\left(\frac{\beta_z}{k} + cos\,\theta\right)\frac{\mathrm{J'_m}(ka\sin\theta)}{1-(k\sin\theta/\beta_\rho a)^2} e^{-jkr_n} \tag{2.8}$$

or a θ-polarized plane wave

$$A'_{\theta,mn} = E_\theta^i \cdot j^m \frac{2m}{k\eta\beta_z \epsilon_{0m} \mathrm{J_m}(\beta_\rho a)\left((\beta_\rho a)^2 + m^2\right)}\left(1 + \frac{\beta_z}{k}\cos\theta\right)\frac{\mathrm{J'_m}(ka\sin\theta)}{\sin\theta} e^{-jkr_n} \tag{2.9}$$

where $\epsilon_{0m} = \{1 \;\; m = 0; 2 \;\; m \neq 0\}$. The total strength of the modes excited in the pipe is simply $A'_{mn} = A'_{\varphi,mn} + A'_{\theta,mn}$.

The second step of the analysis is to propagate the modes down the length of the pipe. This is done by including a phase delay using the appropriate propagation constant β_z. The third and final step is to compute the radiation of the modes into free space. As mentioned above, the radiation of each mode has a closed-form solution, (2.4) and (2.5). The total field is the superposition of all the propagating modes inside the pipe. Combining all three steps of the analysis yields the following equation for finding the transmission through a straight circular pipe:

$$E_{\varphi}^{tx} = E_{\varphi}^{i} \sum_{m} \sum_{n} A'_{\varphi,mn} \cdot e^{-j\beta_z L} \cdot A_{\varphi,mn} \tag{2.10}$$

The approach here showed the procedure for the TE modes, the solution using TM modes follows the same methodology. Using the analysis procedure above, the major physics of the pipe are captured. The benefit of this approach is that a closed-form solution can be derived allowing for very fast computation of the transmission through a pipe.

2.3 TRANSMISSION THROUGH A PIPE WITH TWO OPEN ENDS

Here the analysis procedure from the previous section is used to compute the transmission through a pipe and the results are verified against measurement data. First, the transmission through a pipe with a radius a of 1.8 cm and length L of 60 cm is computed for θ_i and θ_{tx} set to zero. The results are shown in Fig. 2.4. It is observed that below 14 GHz energy is carried through the pipe by the dominant TE_{11} mode. Above 14 GHz the TE_{12} mode is above cutoff and therefore propagates. The difference in the propagation constants between the TE_{11} and TE_{12} modes results in the interference pattern observed. The cutoff phenomena can be clearly seen when the short-time Fourier transform (STFT) [43]-[45] is taken, as seen by the resulting spectrogram in Fig. 2.5. A dispersion curve is clearly observed near 14 GHz, which is characteristic of cutoff phenomena in waveguides.

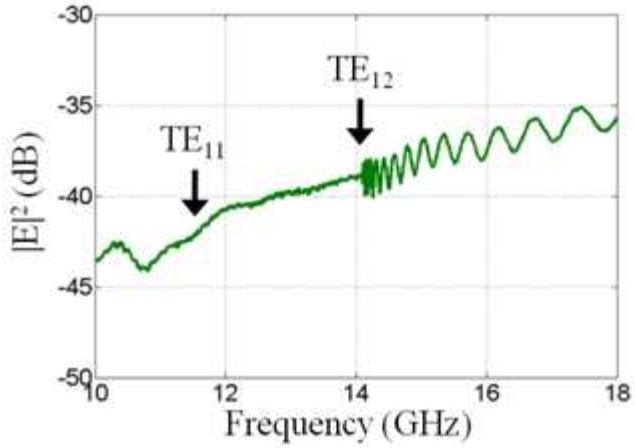

Figure 2.4: Transmission through a pipe computed for $\theta_i = 0°$ and $\theta_{tx} = 0°$.

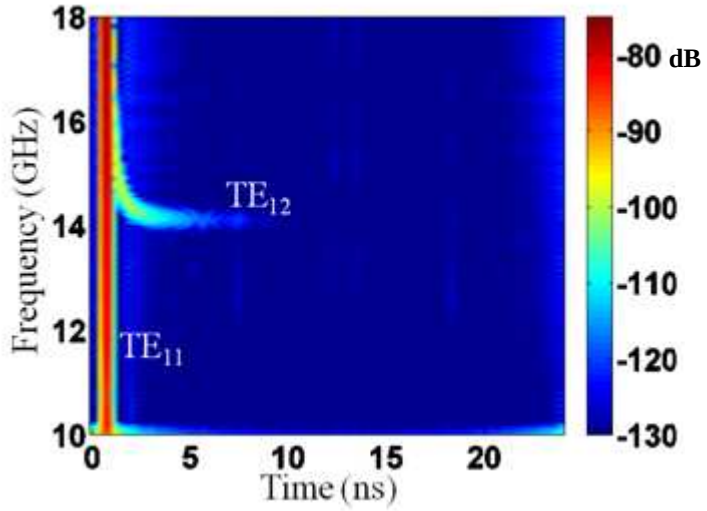

Figure 2.5: Spectrogram of data in Fig. 2.4.

Measurements were made in the laboratory to verify the simulation results. Details of the measurement equipment used can be found in Appendix A. The measurement setup is shown in Fig. 2.6, where a pipe is embedded in absorbers to ensure that propagation only takes place through the pipe. The pipe has a radius of 1.8 cm, a

length of 60 cm, and data are collected from 1 to 18 GHz. Two broadband horns are placed on both sides of the pipe to measure transmission. Fig. 2.7 shows the three measurements that are made, first the free space transmission between the horns is measured and shown in blue, then the transmission with the absorbers in place is measured and shown in green, the third and final measurement shown in red is the transmission with the pipe in place. It is observed that below cutoff the transmission through the pipe tracks well with the transmission through the absorbers, which implies no power is propagating through pipe. At 4.6 GHz the TE_{11} mode is above cutoff and power is transmitted through the pipe. As the frequency increases the transmission through the pipe approaches that of the free space measurement. This implies that the insertion loss improves with increasing frequency.

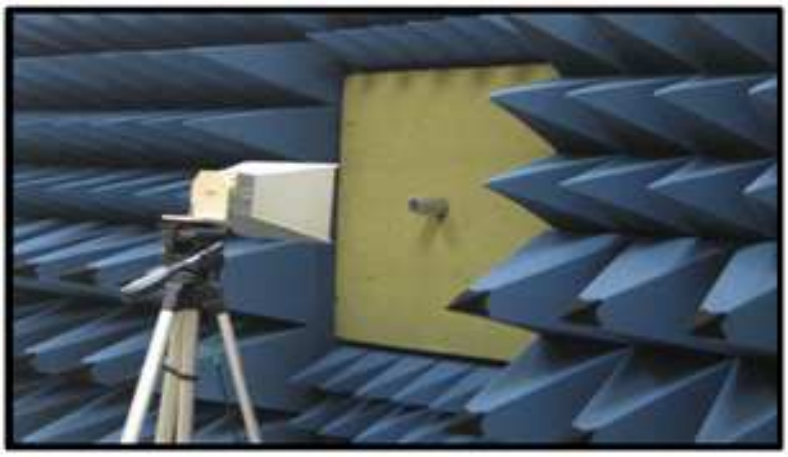

Figure 2.6: Setup used for transmission measurements.

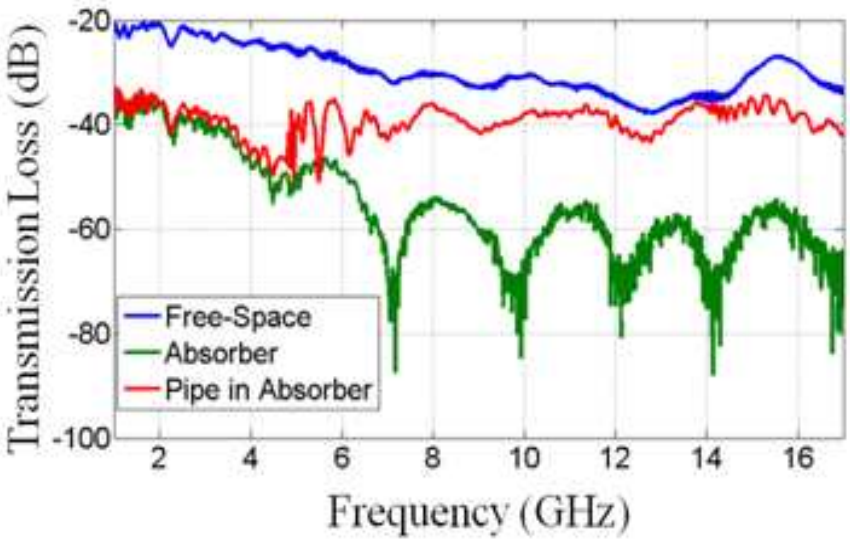

Figure 2.7: Comparison of transmission through free space, absorbers, and a pipe [40].

Fig. 2.8 shows a comparison of spectrograms between the measurement of the transmission through the pipe and the transmission computed using the analysis procedure. As predicted by the analysis, the dispersion curve due to the TE_{12} cutoff is clearly seen in both measurement and simulation. A key difference in the measurement is the presence of a second dispersion curve later in time. This second dispersion curve is a result of higher order interactions between the two ends of the pipe, which were ignored in the analysis. However, it is clear that this higher order effect is much weaker and disappears when the operating frequency is well above the cutoff of the TE_{12} mode. Therefore, the higher order interactions will have a limited effect on the final transmission through the pipe.

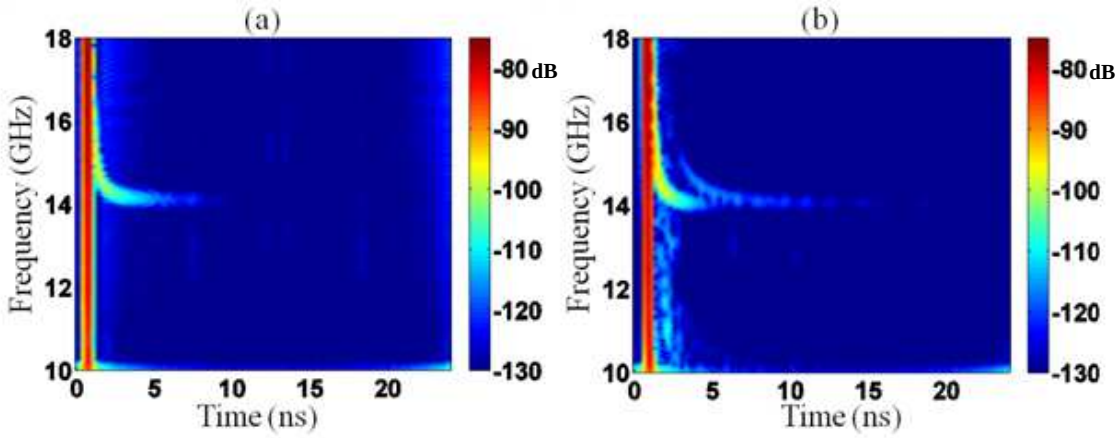

Figure 2.8: Spectrogram of transmission through pipe for (a) simulated data (b) measurement data.

Next the radiation pattern from a pipe is simulated and compared with measurement. The pipe in this case has a radius of 2.55 cm and a length of 76.5 cm. Simulations and measurements are carried out from 12 to 18 GHz. For simulation and measurement the source is placed at 0° in azimuth and the radiation pattern is measured on the opposite side of the pipe between -65° and 65° in azimuth. Figs. 2.9(a) and 2.9(b) show the simulated and measured radiation patterns respectively. The radiation patterns are plotted in dB. Between 12 and 16 GHz, the TE_{11} and TE_{12} modes are excited, which result in the interference pattern observed in frequency. Around 16 GHz the TE_{13} mode is above cutoff and excited. Because the mode is near cutoff, the modal interference results in the rapid oscillations seen in Fig. 2.9. In simulation the cutoff interference is strong near cutoff, whereas in measurement the strength of the interference gradually increases as frequency increases above cutoff. This indicates that in the measurement, the transmission of the TE_{13} mode is weaker near cutoff than predicted by simulation. This

could be due to reflection of the TE_{13} mode from the end of the pipe or conductor loss, which are both strongest near cutoff. However, the effect of the reflection coefficient is limited and the bulk of the physics are properly accounted for. Overall the simulation and measurement are seen to be in strong agreement.

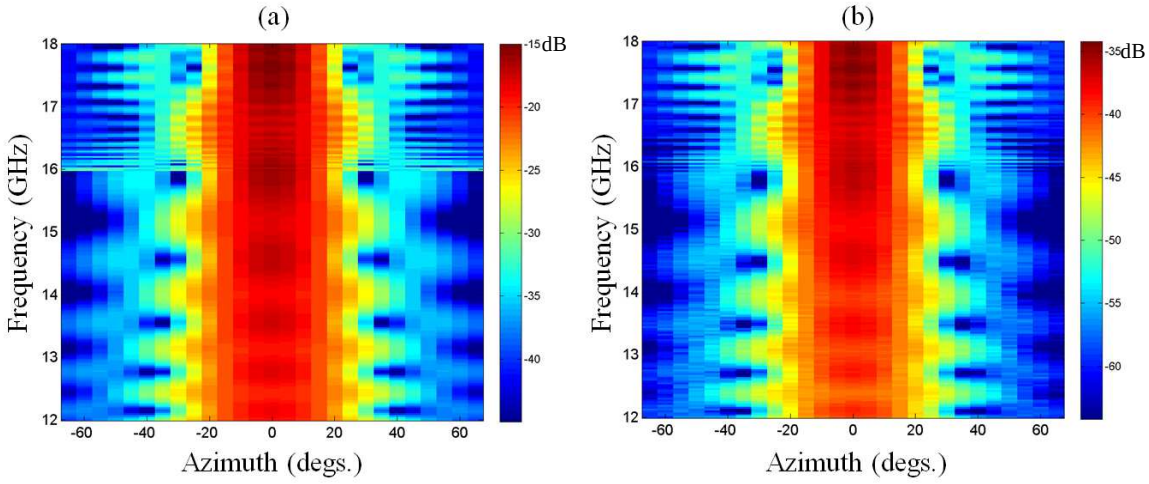

Figure 2.9: Radiation pattern from a pipe for a source at 0° azimuth in (a) simulation (b) measurement.

Next, the simulation and measurement of the radiation patterns are repeated on the same pipe, but the source is moved to 30° in azimuth. Figs. 2.10(a) and 2.10(b) show the simulation and measurement results respectively, both plotted in dB. Again, the simulation and measurement are seen to be in good agreement, further validating the analysis procedure for computing the transmission through a pipe. The off angle source excites more modes, which results in the irregular radiation pattern.

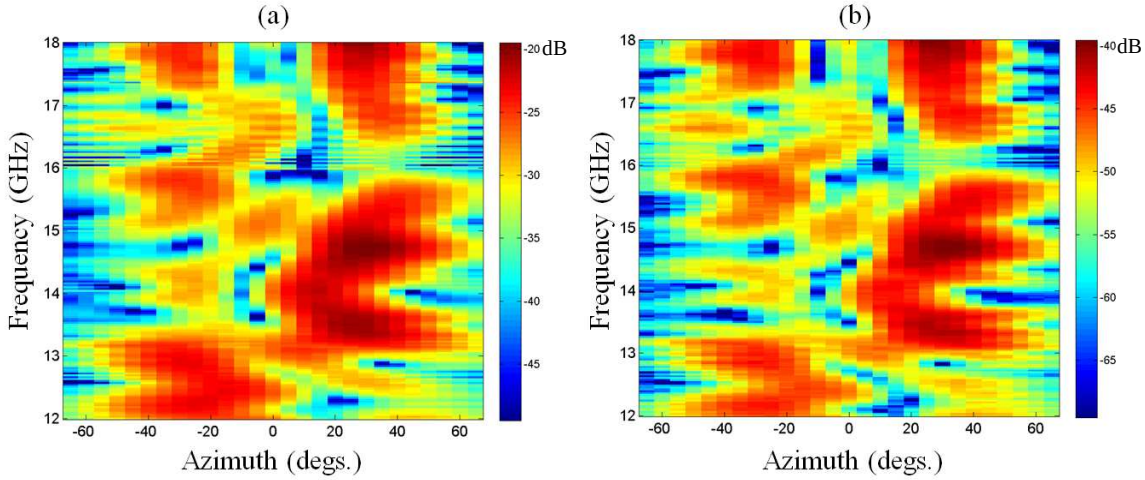

Figure 2.10: Radiation pattern form a pipe for source at 30° azimuth in (a) simulation (b) measurement.

Having verified the analysis approach against measurement data, the insertion loss is computed in order to determine the feasibility of using the pipe as a high frequency propagation channel. Insertion loss for a pipe is computed using:

$$IL = \frac{|E_{\alpha}^{tx}|^2}{|E_{\alpha,fs}^{tx}|^2} \tag{2.11}$$

where E_{α}^{tx} is the transmitted field through a pipe and $E_{\alpha,fs}^{tx}$ is the strength of the field transmitted in free space. Insertion losses for pipes of radii 4.5 cm, 5.5 cm, and 6.5 cm are computed and shown in Fig. 2.11. The results are compared to the insertion loss of a concrete wall as reported by Gibson and Jenn [10]. As previously mentioned, the insertion loss of a wall worsens as the operating frequency increases. Two observations about the insertion loss of the pipe are that the insertion loss improves with increasing frequency and with increasing pipe radius. The conclusion is that a straight pipe can indeed be used as a high frequency propagation channel.

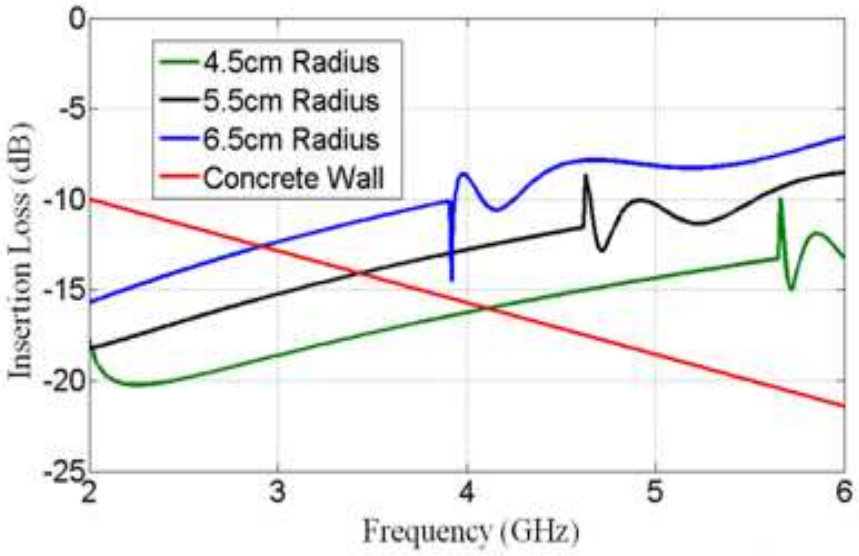

Figure 2.11: Insertion loss of straight pipes of different radii compared to a concrete wall [40].

Two physical effects that were not considered in the analysis are reflections from the ends of the pipe and conductor losses. The reflections from the end of the pipe result in higher order interactions between the two ends of the pipe, which were observed in measurement. In Fig. 2.8(b) and Fig. 2.9(b), the effect of reflections was observed. To account for reflections requires a reworking of the radiation equations shown in (2.4) and (2.5), which will also influence the coupling in (2.8) and (2.9). Unfortunately a closed-form solution for the reflection from a circular pipe opening does not exist. The reflection coefficient for a pipe with radius 2.4 cm is computed using the method of moments solver in the commercial software FEKO [46]. The magnitude of the reflection coefficient is shown in Fig. 2.12. The primary result of Fig. 2.12 is that the reflection coefficient is high near the cutoff of a mode and decreases exponentially with frequency. This confirms what has been observed in measurement.

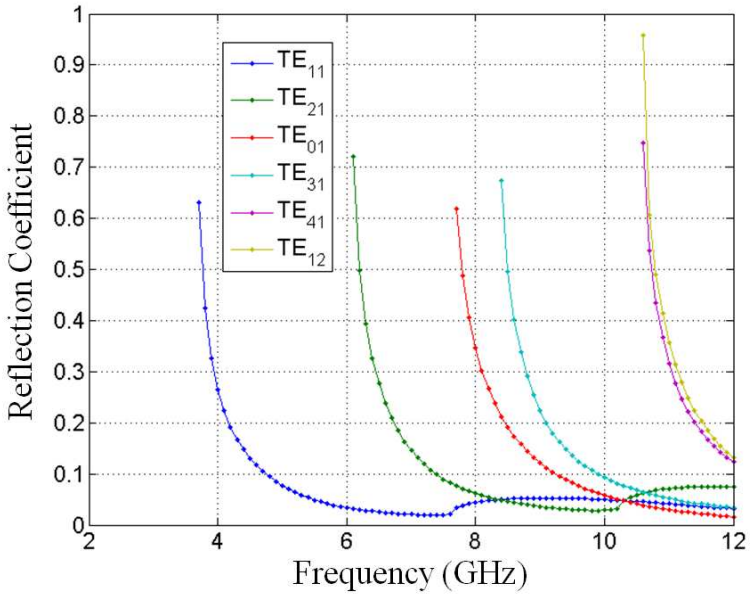

Figure 2.12: Reflection coefficient computed using FEKO for a pipe radius of 2.4 cm.

Conductor losses in the pipe can be accounted for using the power loss method, which is a perturbation approach [47]. In general it would be necessary to solve a new boundary value problem that includes the conductivity of the pipe. The perturbation method assumes that the modal fields do not change when the pipe is not a perfect conductor, which is a reasonable assumption for most metals. The resistance of the pipe is computed as

$$R_s = \sqrt{\frac{\omega}{2\sigma}} \tag{2.12}$$

where σ is the conductivity of the metal. The perturbation approach was used to find the attenuation coefficient for a circular waveguide in [47]. The result was that the

attenuation coefficient for each mode can be computed using the following two equations:

$$\alpha_{mn} = \frac{R_s}{a\eta\sqrt{1-\left(\frac{f_c}{f}\right)^2}}\left[\left(\frac{f_c}{f}\right)^2 + \frac{m^2}{(\chi'_{mn})^2 - m^2}\right] \tag{2.13}$$

for TE modes and

$$\alpha_{mn} = \frac{R_s}{a\eta\sqrt{1-\left(\frac{f_c}{f}\right)^2}} \tag{2.14}$$

for TM modes, where f_c is the mode cutoff. The modified transmission formulation is

$$E_{\varphi}^{tx} = E_{\varphi}^{i}\sum_{m}\sum_{n} A'_{\varphi,mn}\cdot e^{-\alpha_{mn}L}e^{-j\beta_z L}\cdot A_{\varphi,mn}. \tag{2.15}$$

The attenuation coefficient is computed using (2.13) and (2.14) for several lower order modes and shown in Fig. 2.13. From Fig. 2.13 two observations are of interest. First, the TE_{0n} modes have an opposite trend from the other modes, as frequency increases the attenuation coefficient decreases. Second, the TM modes have very high attenuation.

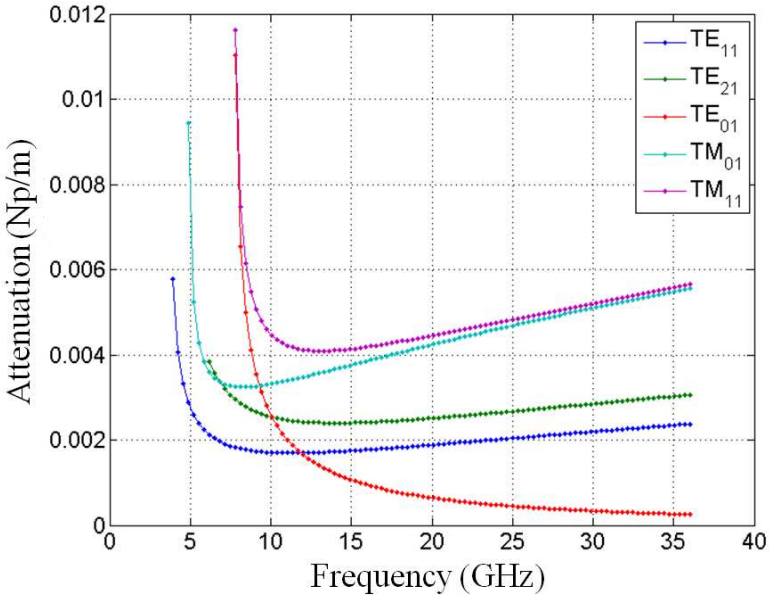

Figure 2.13: Attenuation coefficient for a pipe with radius 2.4 cm.

2.4 BACKSCATTERING THROUGH A PIPE

Having developed an analysis procedure for computing the transmission through a pipe, verified that our analysis captures the pipe physics through measurement, and concluded that the pipe will indeed allow high frequency propagation, the one-way transmission analysis is extended to two-way transmission in order to determine backscattering from a target through the pipe. The two-way backscattering transmission geometry is shown in Fig. 2.14. The incident field is transmitted through the pipe and radiates to the right-hand side. This radiation reflects off a target and the backscattered field becomes a secondary incident field on the pipe, which is then transmitted through the pipe for a second time and radiates back towards the observer on the left-hand side of the pipe.

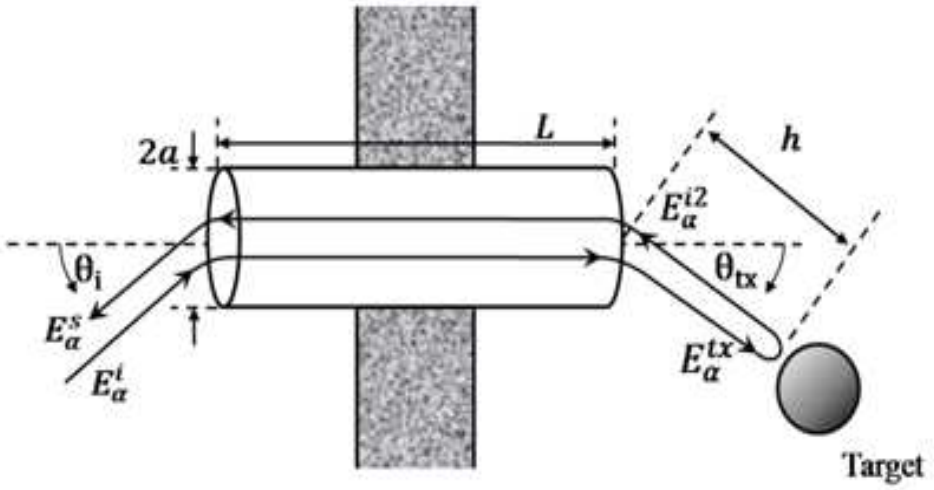

Figure 2.14: Geometry for backscattering from a target propagating through a straight pipe with two open ends.

The specifics of the method for computing the backscattering through a pipe are outlined here. First, the one-way transmission through the pipe is computed from strength of the incident field using (2.10). The transmitted field is scattered by the target

$$E_\alpha^{i2} = \frac{\sqrt{\sigma}}{\sqrt{4\pi}h}|E_\alpha^{tx}|e^{-jkh} \tag{2.16}$$

where σ is the radar cross-section (RCS) of the target. In writing (2.16), it is assumed that the target is well described as a point scatterer, and that there is no higher order interaction between the pipe and the target. The field scattered from the target is now the field incident on the pipe opening from the right-hand side. The one-way transmission through the pipe from right to left is computed using (2.10). By combining the steps outlined here, the backscattering through a pipe is found.

2.5 BACKSCATTERING RESULTS

Using the two-way analysis procedure the scattering from a point target as seen through the pipe is computed and compared to measurement data. Backscattering through a pipe with radius 1.8cm and length of 60cm is simulated. The transceiver is placed 50cm from the pipe opening. The target is a point scatterer with $\sigma = 1$ and placed 1m down-range. Backscattering is simulated using the two-way analysis from the previous section. Figs. 2.15(a) and 2.15(b) show the range profile of the backscattering data for θ_i and θ_{tx} equal to 0° and for θ_i and θ_{tx} equal to 45°, respectively. The backscattering from the pipe is suppressed, which implies that only backscattering from the target is present in Fig. 2.15. In free space it is anticipated that a point scatterer will show up as a sharp peak in the range profile. However, in Fig. 2.15 the return from the target is extended in range due to the pipe dispersion. The range spread is more severe for the off-angle case in Fig. 2.15(b). Fig. 2.16 shows the spectrograms of the backscattering in Fig. 2.15. In Fig. 2.16 it is seen that below the cutoff of the dominant TE_{11} mode there is no return from the target. Once above cutoff the target is seen, however the pipe has injected its physics into the backscattering as indicated by the dispersion curves present. The final observation is that the off angle configuration in Fig. 2.16(b) excites far more modes than in the boresight configuration of Fig. 2.16(a).

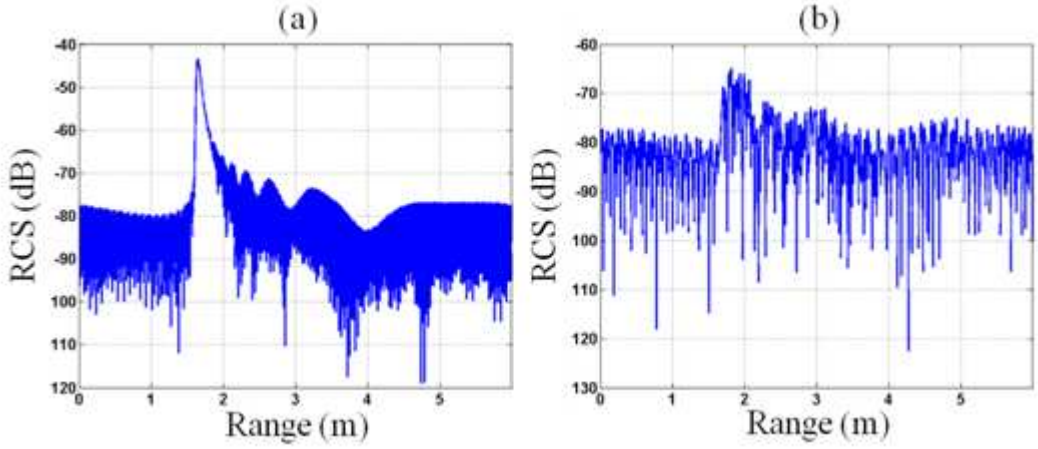

Figure 2.15: Range profile of simulated backscattering through pipe for (a) $\theta_i = 0°$ and $\theta_{tx} = 0°$ and (b) $\theta_i = 45°$ and $\theta_{tx} = 45°$.

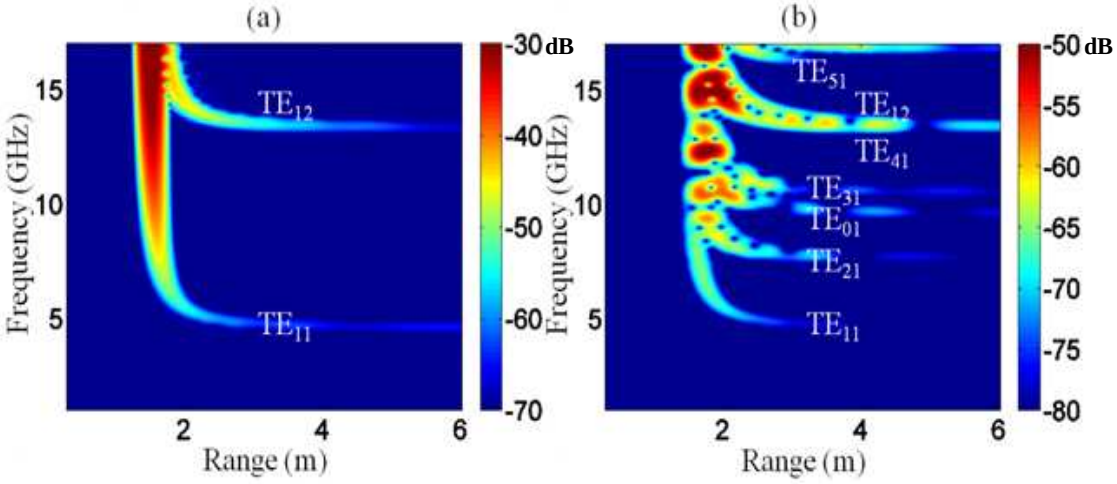

Figure 2.16: Spectrogram of simulated backscattering through pipe for (a) $\theta_i = 0°$ and $\theta_{tx} = 0°$ and (b) $\theta_i = 45°$ and $\theta_{tx} = 45°$ [40].

Fig. 2.17 shows the measured backscattering data for same configurations as in simulation. A corner reflector with an edge length of 17 cm is used as the target as it offers an angularly stable RCS and acts as a point scatterer for the given frequency range of 1 to 18 GHz. Background subtraction is used to suppress the backscattering from

everything except the target. It is clear that the pipe has added its physics to the backscattering data indicated by the dispersion curves. From the backscattering simulations and measurements it is clear that a target can indeed be seen through a pipe.

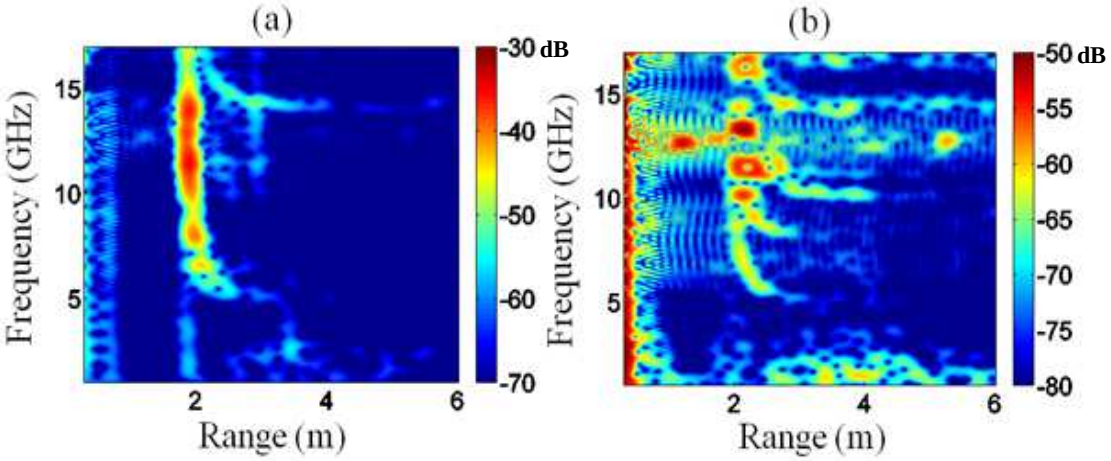

Figure 2.17: Spectrogram of measured backscattering through a pipe for $\theta_i = 0°$ and $\theta_{tx} = 0°$ and (b) $\theta_i = 45°$ and $\theta_{tx} = 45°$ [40].

2.6 CONCLUSIONS

In summary, a modal analysis procedure for the transmission through a straight pipe was developed. The accuracy of the analysis was confirmed through measurement and it was then shown that indeed the insertion loss through a pipe improves with increasing frequency. It was also shown that the insertion loss improves with increasing pipe size. The effect of the reflection coefficient on propagation and a method for accounting for conductor losses was shown. These effects were seen to have a limited influence on the transmission through a pipe. Having verified that the pipe is a feasible propagation channel an analysis was developed for two-way propagation and scattering through a pipe. The final demonstration showed that a target could be seen through the

pipe via simulation and measurement. These results serve as a feasibility study for detecting objects through a pipe. From the results here it is known that distance to the object can be found using frequency diversity. Subsequent chapters will address the problem of finding the cross-range position of the target in order to form two-dimensional radar images.

Chapter 3: Beamforming Through a Pipe

3.1 INTRODUCTION

In this chapter, the possibility of beamforming through a pipe using multiple antenna elements in an effort to obtain cross-range information about targets on the other side of the pipe is explored. While beamforming in free space is a well studied topic in antenna arrays, the presence of the pipe channel introduces an interesting twist to this classical problem. Here, it is shown that beam patterns can be formed through a circular pipe embedded in an opaque wall. The method presented by Mautz and Harrington [49] for free space beamforming is extended to account for the pipe propagation channel. A least squares fit was used in [49] to determine the excitations necessary to synthesize a desired transmit beam pattern using multiple sources radiating in free space.

The remainder of this chapter is divided into four sections. In Section 3.2 a one-way beamforming method is developed and demonstrated in simulation. Then, in Section 3.3, the one-way beamforming algorithm is extended to two-way beamforming. It is applied to simulated backscattering data from a target located on the other side of a pipe in order to obtain the azimuth location of the target. Combined with additional frequency diversity, it becomes possible to acquire both the range and azimuth location of a target through a pipe. In Section 3.4 measurements are made in the laboratory and the results are compared to simulation. It is shown that a two-dimensional image of multiple targets can be generated. The fifth and final section presents conclusions.

3.2 ONE-WAY BEAMFORMING THROUGH A PIPE

Fig. 3.1 illustrates the problem setup, a circular pipe of radius a and length L is embedded in an opaque wall. Multiple sources S_1, S_2,... S_n are located on the left-hand side of the wall. The location of each source is given in terms of its angle θ_n^i and distance R_n with respect to the pipe opening. It is assumed that each source is located at a sufficient distance so that the field incident on the pipe opening due to that source can be considered a plane wave. The position of the target on the right-hand side of the wall is given in terms of its range H^t and azimuth θ^t position. To simulate the backscattering from a target through a circular pipe with two open ends, the modal approach is used.

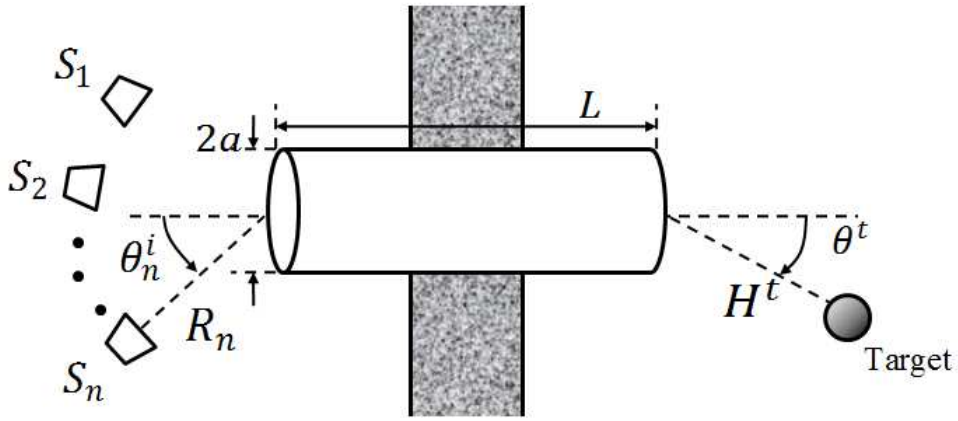

Figure 3.1: Pipe geometry used for beamforming through a pipe.

We begin by focusing our attention on one-way beamforming through the circular pipe. This entails controlling the beam pattern on the right-hand side of the wall using the sources on the left-hand side. Each right-traveling circular waveguide mode excited within the pipe has associated with it a radiation pattern on the right-hand side of the

wall. The amplitude of the waveguide modes that are excited within the pipe is a function of the angular source location θ_n^i, the source excitation strength, and the standoff distance R_n from the source to the pipe opening. Therefore, by using multiple source locations and controlling the complex excitations applied to each source, the beam pattern on the right-hand side of the wall can be controlled. To compute the proper complex excitations, the strength of each source is related to the radiation pattern on the right-hand side of the wall in the form

$$[T](f) = (g) \tag{3.1}$$

where $[*]$ denotes a matrix and $(*)$ denotes a vector. In equation (3.1), the elements of (f) are the complex excitations applied to the sources, (g) is the resulting beam pattern on the right-hand side of the wall, and the columns of $[T]$ are the beam patterns resulting from each source individually. For beamforming, (f) is solved in order to best approximate a desired beam pattern (g_o) using a least squares fit.

Fig. 3.2 shows simulation results for beamforming through a pipe with radius 1.8 cm and length 60 cm using three sources at 12 GHz. For the chosen pipe diameter there are 4 propagating TE modes at 12 GHz. More sources will lead to more control over the beam pattern, until the number of sources reaches the number of propagating modes. The sources are each placed 50 cm from the pipe opening and at angular locations $\theta_1 = 45°$, $\theta_2 = 0°$, and $\theta_3 = -45°$. Fig. 3.2(a) shows the individual radiation patterns resulting from each source observed for $-60^\circ \leq \theta_{obs} \leq 60^\circ$. The radiation patterns in Fig. 3.2(a) represent the columns of $[T]$. For beamforming a simple Kronecker delta function

$$g_o(\theta_{obs}) = \begin{cases} 1 \text{ if } \theta_{obs} = \theta_{max} \\ 0 \text{ if } \theta_{obs} \neq \theta_{max} \end{cases} \tag{3.2}$$

is used as (g_o). This choice ensures that the beam maximum occurs in the direction θ_{max}. While other choices for (g_o) were tested and shown to give better performance in terms of sensitivity and sidelobes, the Kronecker delta gave the best beamwidth performance. Fig. 3.2(b) shows the resulting beam patterns for $\theta_{max} = 0^{\circ}$, $\theta_{max} = 20^{\circ}$, and $\theta_{max} = 40^{\circ}$. The simulation results show that by using three sources the transmitted beam pattern on the right-hand side of the wall is successfully steered to the desired directions.

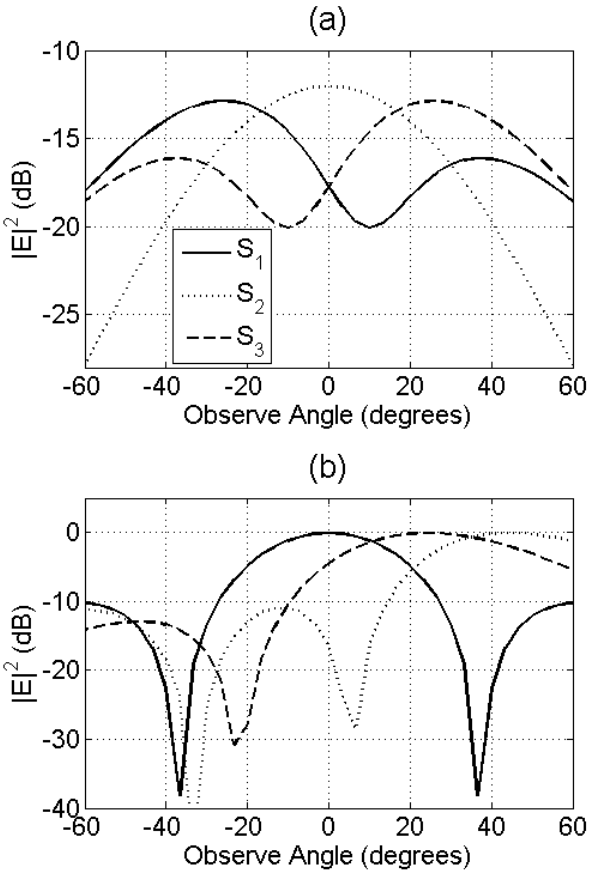

Figure 3.2: Three source beamforming at 12 GHz: (a) basis functions (b) beamforms steered to 0˚ with excitation (S_1 = -0.56-j0.23, S_2 = 1.00, S_3 = 0.56+j0.23), 20˚ (-0.93-j0.26, 1.00, 0.88-j0.13), and 40˚ (-0.62+j0.80, 1.00, -0.86+j0.08).

3.3 TWO-WAY BEAMFORMING THROUGH A PIPE

Having achieved one-way beamforming through a pipe, the concept is extended to two-way beamforming in order to determine the azimuth location of a target θ^t from its backscattering data through a pipe. Here, it is assumed that each source element acts as a transceiver. By operating on the transmitted and received signals, two-way beamforming is achieved. For the transmitted signal, one-way beamforming is applied so that the beam

maximum is steered to the desired direction. By reciprocity it is known that the excitations used to maximize transmission in a given direction can be used to maximize the backscattering from the same direction. Therefore, the signal received at each transceiver is weighted and summed using the same excitations used for transmission. The two-way beamforming procedure has the form:

$$(f_1 \quad \dots \quad f_n)\begin{bmatrix} S_{11} & \dots & S_{1n} \\ \vdots & \ddots & \vdots \\ S_{n1} & \dots & S_{nn} \end{bmatrix}\begin{pmatrix} f_1 \\ \vdots \\ f_n \end{pmatrix} = Az(\theta_{obs}) \tag{3.3}$$

where the $[S]$ matrix in equation (3.3) represents the backscattering matrix from the target. Each element S_{ik} represents the scattering from the target excited by the k^{th} source and received by the i^{th} source. Therefore the size of $[S]$ depends on the number of transceivers used. The vectors (f) are the complex excitations computed using equation (3.1). The excitations (f) are applied to the left-hand and right-hand side of $[S]$ for both receive and transmit beamforming respectively. The excitations are computed for each observation angle θ_{obs} of interest and applied according to equation (3.3). The resulting $Az(\theta_{obs})$ gives an estimate to the backscattering strength versus azimuth location. It should show a peak at the target azimuth θ^t. It is of course also possible to determine the range to the target H^t via frequency diversity. Therefore, by combining the range and azimuth information, the location of the target in two-dimensional space is determined. This is implemented by applying the beamforming procedure above across multiple frequencies and then applying the inverse Fourier transform across frequency at each observation angle θ_{obs}. The final result is a two-dimensional image in azimuth and range.

To demonstrate the above two-way beamforming procedure, target backscattering data are simulated and processed. For simulation the same configuration as the one-way beamforming is used with 3 transceivers. The target is a corner reflector with an edge length of 17 cm. Two target configurations are simulated. First the target is set such that $H^t = 2\,m$ and $\theta^t = 0^\circ$. Next the target is moved to $\theta^t = -25^\circ$ at the same range H^t. Target backscattering data are collected for 12-18 GHz. Figs. 3.3(a) and 3.3(b) show the results of applying beamforming to the target backscattering data for the two different target locations. Both beamformed results show strong backscattering centered about the expected target azimuths at 0˚ and -25˚ as expected. Above 14 GHz an additional mode is above cutoff which allows for more control in the beamforming operation. This is reflected in the reduced sidelobe level observed above 14 GHz in Figs. 3.3(a) and 3.3(b).

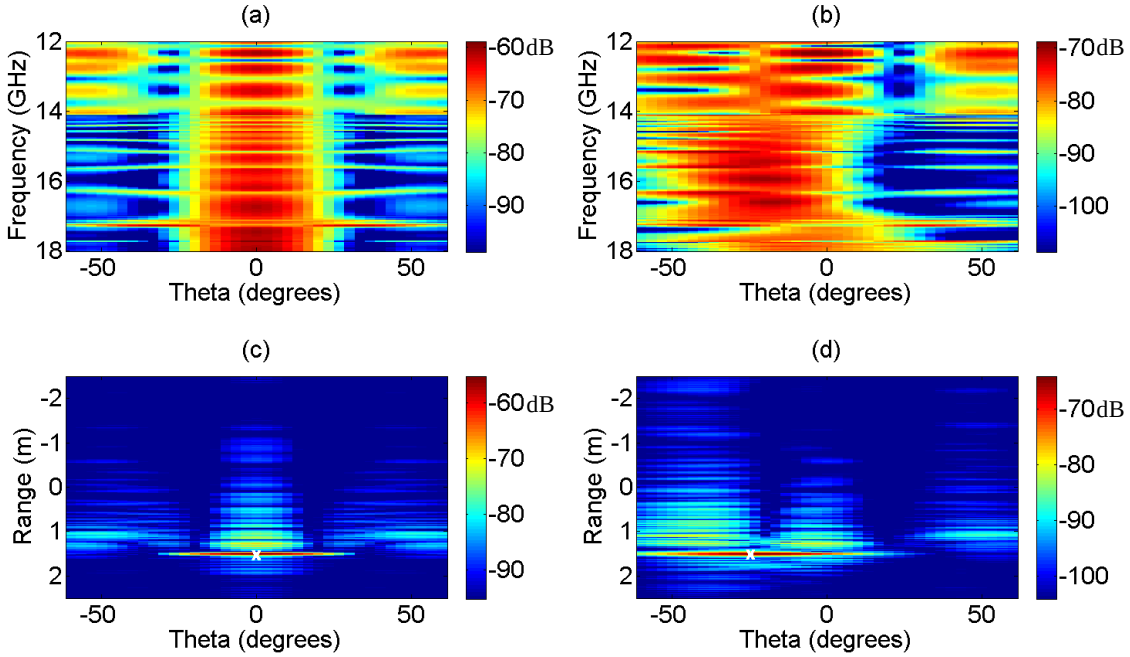

Figure 3.3: Simulation of target backscattering data for (a) beamforming with $\theta^t = 0^\circ$ (b) beamforming with $\theta^t = 45^\circ$ (c) beamforming and ranging with $\theta^t = 0^\circ$ (d) beamforming and ranging with $\theta^t = 45^\circ$.

Figs. 3.3(c) and 3.3(d) show the result of applying an inverse Fourier transform along the frequency dimension to Figs. 3.3(a) and 3.3(b) respectively. The target location is now given in terms of its range H^t and azimuth location θ^t. The white 'x' markers in Figs. 3.3(c) and 3.3(d) indicate the true location of the targets. It is clear that by combining beamforming and ranging, it is possible to generate a two-dimensional image of the target location through a pipe. One important comment is in order here. The images show that the target is 1.5 m down-range. However based on the dimensions of the problem one may expect the target to be 0.5 + 0.6 + 2 = 3.1 m down-range. This discrepancy is a result of the beamforming procedure. Since the fitting function (g_o) is chosen to be real (i.e. zero phase), the least squares fit adjusts the phase on (f) to

compensate for any phase delay present in $[T]$. When the columns of $[T]$ are computed for simulation, the phase delay from the transceivers to the pipe (0.5 m), down the length of the pipe (0.6 m), and from the pipe to the calibration plane (0.5 m) is included in the data. Therefore, after beamforming the phase delay from the transceivers to the calibration plane is not present in the final data, which is observed in Figs. 3.3(c) and 3.3(d). This phase compensation also accounts for the fact that the target is well focused in range, despite the highly dispersive nature of propagation through the pipe .

3.4 BEAMFORMING MEASUREMENT RESULTS

To confirm the simulation results are achievable in practice, measurement data are collected and processed using the equipment and techniques described in Appendix A. For measurement a metal pipe with the same dimensions as the simulations (radius 1.8 cm and length 60 cm) is used. The pipe is embedded in an absorbing wall to ensure that wave propagation only occurs through the pipe. Three sources are used each located 0.5 m away from the pipe opening at angular locations $\theta_1 = 45°$, $\theta_2 = 0°$, and $\theta_3 = -45°$. All measurements are taken using a vector network analyzer. Data are collected at 201 equally spaced points from 12-18 GHz. The measurement procedure involves three steps. First, a calibration measurement is made, where the radiation pattern on the right side of the wall is measured for each source individually. The radiation pattern is measured for $-60^{\circ} \leq \theta_{obs} \leq 60^{\circ}$ at 37 equally spaced steps using a receiver placed approximately 0.5 m from the pipe opening. Second, the target backscattering data are collected. Two corner reflectors are used as targets with locations ($H^t = 1.5\,m$, $\theta^t = 0^{\circ}$), and ($H^t = 0.7\,m$,

$\theta^t = -25^\circ$). Finally, the beamforming excitations are found using (3.1) and the backscattering data are processed using (3.3). For comparison the measurement setup is simulated and processed in the same manner.

Fig. 3.4(a) shows the simulation results and Fig. 3.4(b) shows the measurement results of beamforming and then applying the inverse Fourier transform along the frequency dimension. The resulting image gives the target locations in terms of azimuth and range and the white 'x' markers indicate the true locations of the targets. It is clear in both Figs. 3.4(a) and 3.4(b) that two targets are present and located at approximately 0˚ and -25˚ in azimuth. It is also clear that the target located at 0˚ is 0.8 m further down-range than the target at -25˚. The offset between the dimensions of the problem described and the range to the targets shown in Fig. 3.4 is again due to the phase compensation in beamforming discussed previously. The antenna effects and transmit power are not factored out of the measured results, which accounts for the discrepancy in the magnitude of the backscattering between simulation and measurement. However, normalizing the magnitude would not alter the conclusions drawn from the results. The measurement results confirm that it is possible to obtain an image of a target through a pipe using beamforming and frequency diversity. The agreement between measurement and simulation also indicates the possibility of using the simulation model to estimate an unknown pipe channel by tuning the pipe parameters.

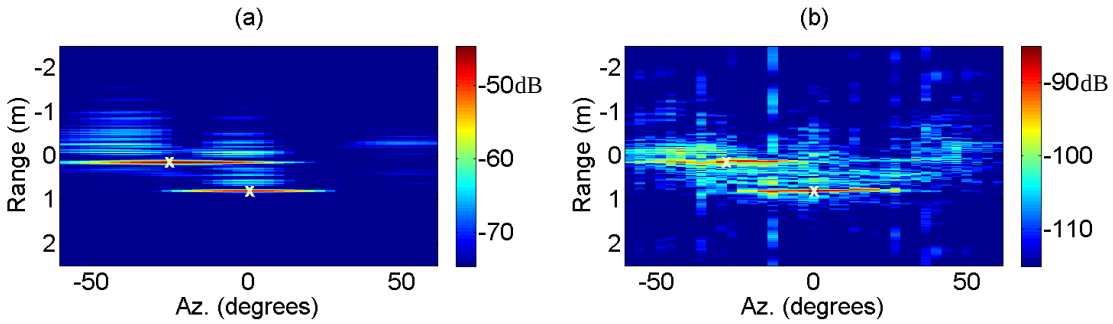

Figure 3.4: Backscattering from two targets processed using beamforming and ranging for (a) simulated data and (b) measured data.

3.5 CONCLUSIONS

In this chapter, the possibility of using beamforming to obtain the azimuth location of a target through a pipe was investigated. First, it was discussed how beamforming through a pipe is accomplished and provided simulation results for demonstration purposes. Then it was discussed how beamforming can be applied to target backscattering data through a pipe to determine the azimuth position of the target. By collecting data across multiple frequencies, the inverse Fourier transform can be applied and the down-range and azimuth position of the target is obtained simultaneously, thus giving a two-dimensional image. The imaging procedure was demonstrated through simulation and then confirmed with measurement data obtained in the laboratory. The beamforming method is fairly straight forward, but operates on bistatic data. In addition, it was difficult to use simulated patterns for beamforming with measurement data. Therefore a calibration procedure was conducted to obtain the pattern for each transceiver position. Ideally an imaging method would operate on monostatic data and it would be

possible to use simulated patterns to process measurement data. This leads us to the investigation of alternate imaging methods.

Chapter 4: SAR Imaging Through a Pipe

4.1 INTRODUCTION

In this chapter, imaging through a pipe using synthetic aperture radar (SAR) techniques is investigated. SAR imaging in free space is a well studied problem. It is shown that SAR techniques used in free space can be adapted to the problem of imaging through a pipe. In the previous chapter, a procedure was developed for beamforming through a circular pipe and two-dimensional images were obtained from bistatic scattering data collected through a pipe. However, the procedure required laborious bistatic data collection and was not very robust. Our approach to SAR imaging through a pipe is based on a matched filter projection process, where the matched filter is obtained through electromagnetic simulation. This is similar to methods that have been applied in through-wall imaging in order to account for the propagation effects of the wall [17]-[20]. This chapter is divided into three sections. In Section 4.2, a methodology for imaging through a pipe using SAR concepts and techniques is presented. In Section 4.3, a set of simulations are used to demonstrate the imaging methodology. The simulation results are corroborated with measurement data. Finally, conclusions are presented in Section 4.4.

4.2 SAR IMAGING THROUGH A PIPE METHOD

Fig. 4.1 illustrates the problem geometry and data collection procedure. In Fig. 4.1 a circular pipe with radius a and length L is embedded in an opaque wall, i.e., transmission only takes place through the pipe. The target to be imaged is located on the right-hand side of the pipe and its location is described by its polar coordinates $\bar{r}(r,\theta)$

where the origin is located at the right-hand pipe opening. To form a synthetic aperture, monostatic broadband backscattering data are collected on the left-hand side of the pipe at N positions along a scan line, as indicated in Fig. 4.1. The scan line in Fig. 4.1 is shown as a straight line. However, the scan line can be chosen to form any arbitrary aperture. The position of the antenna at each data collection point is described by its polar coordinates $\bar{r}_n(r_n, \theta_n)$ where the origin is located at the left-hand pipe opening.

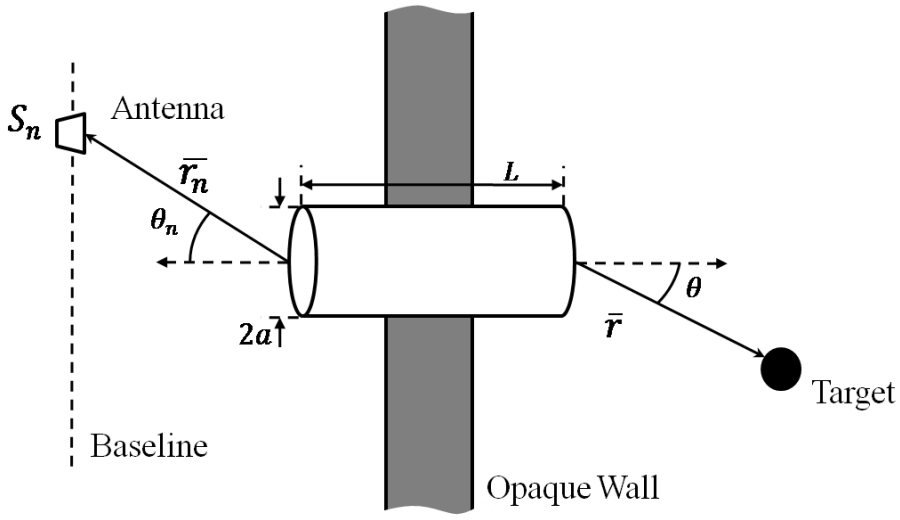

Figure 4.1: Geometry for SAR imaging through a pipe.

The objective is to form a two-dimensional image of the target on the right-hand side of the pipe from the monostatic backscattering data collected on the left-hand side of the pipe. Within the imaging volume V it is assumed that the target can be described by a reflectivity distribution $\sigma(\bar{r})$. The imaging volume V is chosen to be on the right-hand side of the pipe such that it does not include any backscattering from the pipe itself. By

only considering scattering from the target, the backscattering collected at each antenna location S_n can be described by

$$S_n(\bar{r_n}, k) = \int_V \sigma(\bar{r}) H(\bar{r}, \bar{r_n}, k) dV \tag{4.1}$$

where $H(\bar{r}, \bar{r_n}, k)$ is the two-way transmission response through the pipe, which is a function of the antenna position $\bar{r_n}$, target position $\bar{r}$, and the frequency k. $H(\bar{r}, \bar{r_n}, k)$ includes the two-way propagation from the antenna to the pipe opening e^{-j2kr_n} and the two-way propagation from the pipe opening to the target e^{-j2kr}. To form an image of the target the collected backscattering data are projected into the matched filter of the pipe channel, which is simply the conjugate of the two-way transmission through the pipe, $H^*(\bar{r}, \bar{r_n}, k)$. To form a two-dimensional image, the estimate of the reflectivity distribution $\tilde{\sigma}(\bar{r})$ is found through a two-dimensional projection of the form

$$\tilde{\sigma}(\bar{r}) = \iint_{K,\bar{r_n}} S_n(\bar{r_n}, k) H^*(\bar{r}, \bar{r_n}, k)\, dk d\bar{r_n}. \tag{4.2}$$

After the projection process of (4.2) the sidelobe level of the point spread response can often obscure the final image. Therefore, it is useful to apply an iterative procedure like the matching pursuit algorithm [50][51] to remove the point spread response from the image. Matching pursuit involves three steps. First, the image is formed using (4.2). The second step is to select the voxel within the image with the maximum strength, $\sigma_{max}^i = \max(\tilde{\sigma}(\bar{r}))$, and find the point spread response at that voxel

$H(\bar{r}_{max}, \bar{r}_n, k)$. The third and final step is to subtract the response due to the maximum scatterer $\sigma^i_{max} H(\bar{r}_{max}, \bar{r}_n, k)$ from the data

$$S_n^{i+1}(\bar{r}_n, k) = S_n^i(\bar{r}_n, k) - \sigma^i_{max}\, H(\bar{r}_{max}, \bar{r}_n, k) \tag{4.3}$$

where $S_n^{i+1}(\bar{r}_n, k)$ is the residual data for the next iteration. This procedure is repeated until the energy in the residual data S_n^{i+1} is smaller than the maximum tolerable error. By applying matching pursuit, a reflectivity distribution is obtained that only consists of σ^i_{max} from each iteration and the result is an image that is well localized in range and azimuth.

4.3 SAR IMAGING THROUGH A PIPE RESULTS

The imaging methodology outlined in Section 4.2 is demonstrated through simulation and the results are corroborated with measurement data collected in the laboratory. A straight circular pipe with radius 2.54 cm and length 31 cm is used for both simulation and measurement. For simulation and measurement, data are collected at 53 points along a synthetic aperture that forms a circular arc centered around the pipe opening. Each data collection point has a constant radial position $r_n = 0.5$ m and the angular position for each point is swept over angles $\theta_n = [-65°, 65°]$. Monostatic backscattering data from a single point scatterer located at $\bar{r}(1.2\text{ m}, 0°)$ are simulated for 201 frequency points between 12 GHz and 18 GHz. The simulations only consider backscattering that propagates through the pipe. The imaging space is divided into a grid

of 201x201 voxels placed at equally spaced radial points between 0.7 m and 1.7 m, and equally spaced angular points between -85° and 85°. The backscattering data are first processed using a matched filter for free space propagation and the resulting image is shown in Fig. 4.2. It can clearly be seen that the free-space propagation model is poorly matched to the data. The point target is not focused in either angle or range. This is due to the complex radiation pattern in angle and highly frequency dispersive nature of the pipe. Therefore, it is necessary to compute the correct matched filter for the pipe for image formation.

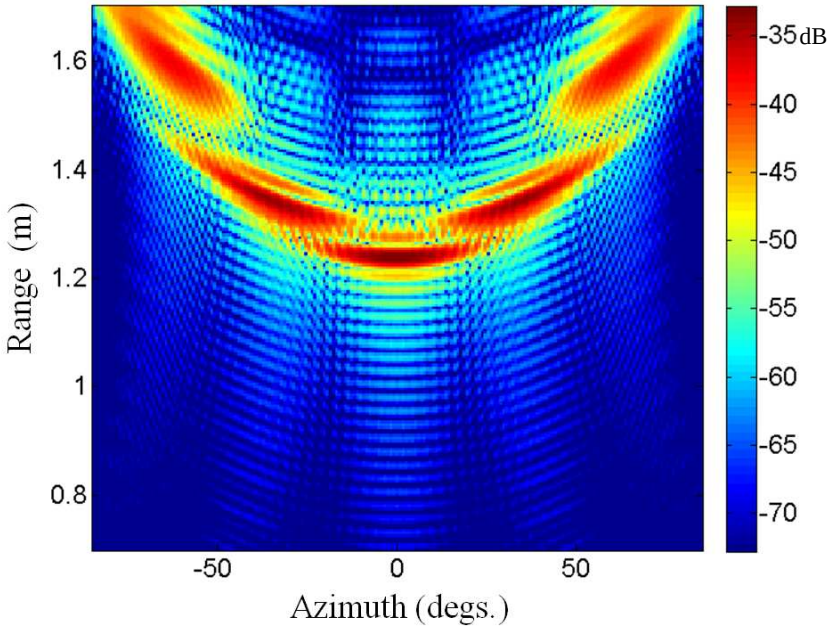

Figure 4.2: SAR imaging through a pipe of a point scatterer using a mismatched filter.

The matched filter for the pipe is found using the closed form solution to the transmission through a circular pipe described in Chapter 2. The result of projecting the simulated backscattering data into the matched filter for the pipe channel using (4.2) is

shown in Fig. 4.3(a) on a 40 dB dynamic range. All other images in the remainder of this section are also plotted on a 40 dB dynamic range. The peak in the image corresponds to the correct range and angle location of the point scatterer. To verify the simulation results, backscattering through a pipe is measured using the same data collection and imaging parameters. Measurement techniques and methods are described in Appendix A. As with the transmission measurements the pipe is embedded in absorbers to ensure propagation only takes place through the pipe. A corner reflector is used as the target and background subtraction is used to suppress clutter scattering. Fig. 4.3(b) shows the result of projecting the measurement data into the simulated matched filter for the pipe based on simulation. The resulting image agrees well with Fig. 4.3(a), again showing the correct location of the point scatterer. This result demonstrates that the simulated matched filter can be used robustly in image formation.

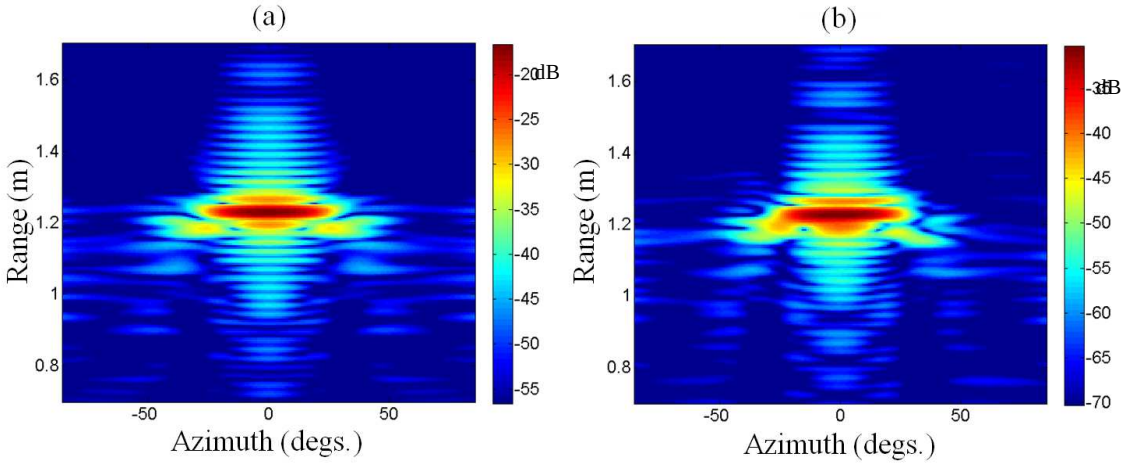

Figure 4.3: Matched filter point spread response through a pipe using (a) simulated and (b) measured data.

From Fig. 4.3 it is clear that the matched filter projection suffers from fairly high sidelobes in the point spread response, which may overshadow other scatterers when multiple targets are present. To remove the point spread response, matching pursuit is applied to both the simulation results of Fig. 4.3(a) and the measurement results of Fig. 4.3(b). The resolutions of the matching pursuit images are reduced to 50x50 in order to increase the clarity of the final image. The results of applying matching pursuit to the simulated and measured data are shown in Figs. 4.4(a) and 4.4(b), respectively. In the measurement results of Fig. 4.4(b), additional scattering centers are extracted around the strongest scatterer. The additional features are extracted due to mismatch between the simulated point spread response and the point spread response of the real target. However, these scattering centers are much weaker, at least 15 dB weaker, and the scattering center due to the corner reflector is dominant.

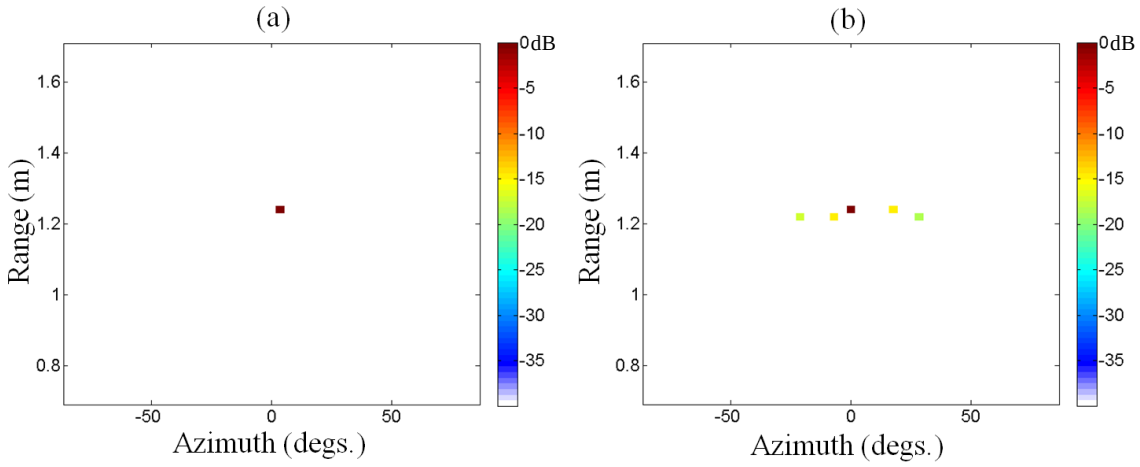

Figure 4.4: Matching pursuit point spread response through a pipe using (a) simulated and (b) measured data.

A second target configuration is simulated consisting of two points scatterers. The first point scatterer is located at $\bar{r}(1.15\text{ m}, -20°)$ and the second at $\bar{r}(1.5\text{ m}, 20°)$. The matched filter image from the simulation data is shown in Fig. 4.5(a). Measured backscattering data are collected from two corner reflectors at the same locations and the resulting matched filter image (again using the simulated matched filter response) is shown in Fig. 4.5(b). From Figs. 4.5(a) and 4.5(b) the two targets can be clearly seen from the strong scattering. However, due to the high sidelobe levels in the point spread response, there are what appear to be artificial scattering centers at approximately $\bar{r}(1.45\text{ m}, -40°)$ and $\bar{r}(1.45\text{ m}, -40°)$. This ambiguity is resolved by removing the point spread response via matching pursuit. The results of applying matching pursuit as before are shown in Fig. 4.6(a) for simulated data and Fig. 4.6(b) for measurement data. In Figs. 4.6(a) and 4.6(b) the two targets are clearly seen at the appropriate locations. Again, additional scattering centers are extracted in the measurement data of Fig. 4.6(b), but the extraneous centers are weaker than the actual target centers by approximately 10 dB. Although not shown here, it was found that the resolution in angle is intrinsically limited by the electric size of the pipe.

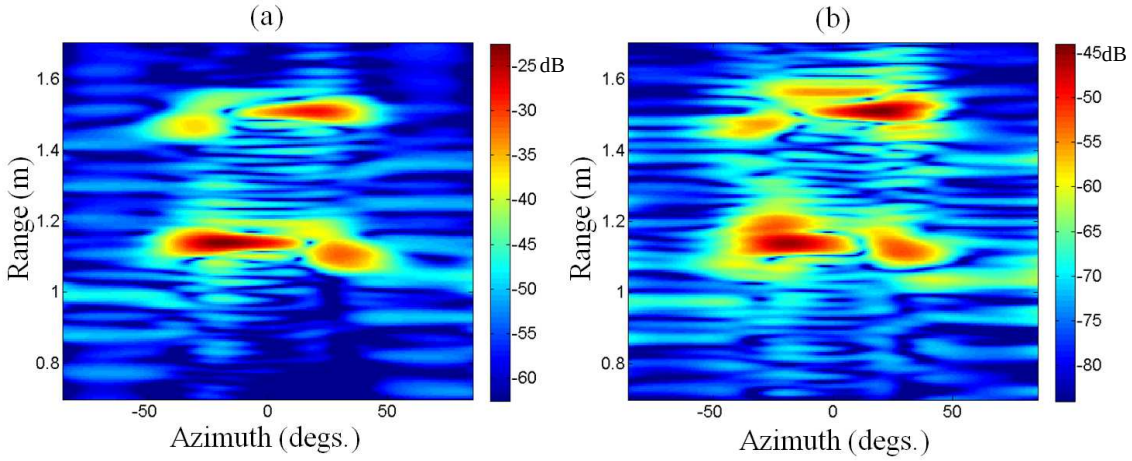

Figure 4.5: Two target matched filter image through a pipe using (a) simulated and (b) measured data.

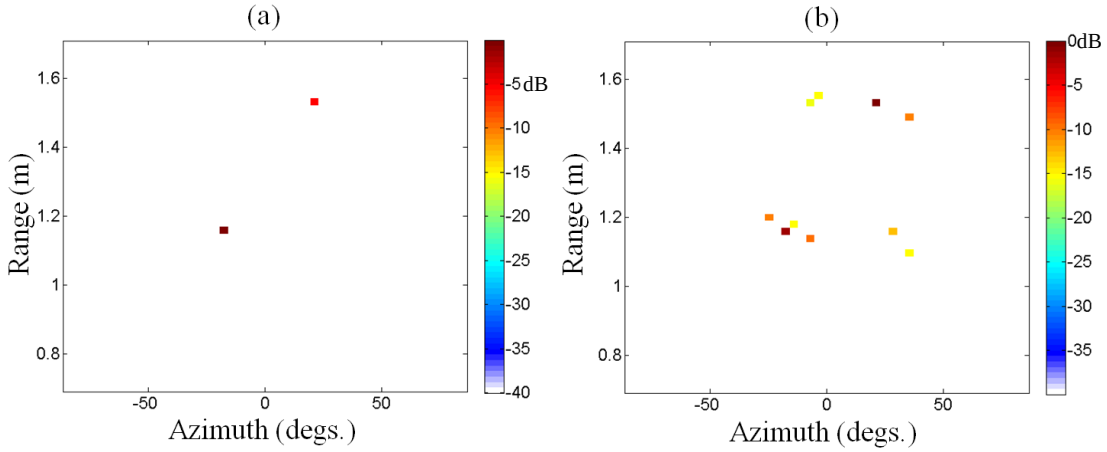

Figure 4.6: Two target matching pursuit image through a pipe using (a) simulated and (b) measured data.

4.4 CONCLUSIONS

In this chapter, a radar image of a scene on one side of an open pipe was generated using matched filter processing. To form the image in a robust manner, SAR techniques used in free space were adapted to the problem of imaging through a pipe. By

collecting monostatic data along a synthetic aperture and projecting the data into the matched filter of the pipe channel, an image was formed. The closed form solution for transmission through a pipe was used to compute the matched filter for a straight circular pipe, which was shown to be useful for processing both simulation and measurement data. The point spread response was subsequently removed using the matching pursuit procedure to reduce sidelobe interference. The imaging methodology was demonstrated through simulation and corroborated with measurement data collected in the laboratory. In this chapter and the previous chapter it was seen that the cross-range resolution is fairly poor. The cross-range resolution is intrinsically related to the size of the pipe. Therefore, to improve the cross-range resolution a bigger pipe would be needed if processing with beamforming or matched filter processing. However, a bigger pipe may not be available, which has motivated the exploration of higher resolution processing methodologies in the next two chapters.

Chapter 5: Superresolution Imaging Through a Pipe Using MUSIC

5.1 INTRODUCTION

In the previous chapters it was seen that the cross-range resolution for a pipe with a diameter on the order of a few wavelengths is poor when using delay-and-sum beamforming and matched filter processing. In this chapter, the MUSIC (MUltiple SIgnal Classification) algorithm [55][56] is applied to the pipe imaging problem in order to improve the cross-range resolution of the radar image. First, an overview of the MUSIC algorithm is presented in Section 5.2 with an explanation of how the method is applied to DOA estimation through a pipe. Then, a method for applying MUSIC to radar imaging through a pipe is developed in Section 5.3. The method using MUSIC is demonstrated with simulated and measured backscattering data and the results are compared to matched filter processing in Section 5.4. Section 5.5 discusses the effects of uncertainty on the MUSIC algorithm through a pipe. Conclusions are given in Section 5.6.

5.2 OVERVIEW OF MUSIC ALGORITHM

We begin with an overview of the MUSIC algorithm for direction of arrival (DOA) estimation using an array. In array processing the ability to unambiguously resolve the cross-range position of two targets is bounded by the size of the collection aperture. The aperture size sets a lower bound on resolution, superresolution methods aim to beat this bound and provide superior resolution. Early on, in 1969, Capon introduced the maximum likelihood estimator for spectral estimation [52]. Around the same time, Burg introduced a similar method known as maximum entropy [53]. Both the maximum

likelihood and maximum entropy methods use probabilistic solutions to provide superresolution. In 1973 Pisarenko introduced a spectral estimation method based on the eigen decomposition of the signal covariance matrix [54]. Pisarenko's method assumed free space propagation models and a linear array with uniform sampling. This early work using the covariance matrix spawned the two well-known superresolution methods, MUltiple SIgnal Classification (MUSIC) and Estimation of Signal Parameters via Rotational Invariance Techniques (ESPRIT). In 1979, Schmidt introduced the MUSIC algorithm [55][56], which is a generalization of Pisarenko's method. Later, in 1985, Roy, Paulraj, and Kailath introduced the ESPRIT algorithm [57]. While ESPRIT is useful, it assumes that the signal is modeled by weighted exponentials, which helps it to outperform MUSIC in computational efficiency at the expense of loss of generality. The methods of ESPRIT and MUSIC fall into the category of superresolving methods known as signal subspace methods.

The MUSIC algorithm was initially developed for DOA estimation of radiating sources. However, MUSIC has also been shown to be useful for radar imaging. In 1991, Walton et al. used MUSIC to enhance the cross-range resolution in a radar imaging scheme [58]. Later, in 1994, Odendaal, Barnard, and Pistorious showed that MUSIC could be used for two-dimensional superresolution imaging [59]. Recently, MUSIC has also been applied to through-wall radar imaging using UWB [60] and time-reversal methods [61]. The most appealing aspect of the MUSIC algorithm is that it was derived in a general sense. Many supperresolution algorithms make assumptions about the signal model or collection aperture, such as linear uniform sampling. However, the only

assumption made in the MUSIC algorithm is that the sources are decorrelated. This makes the MUSIC algorithm an excellent candidate to improve the resolution of DOA estimation in a complex propagation environment, specifically in our through-pipe problem.

To apply the MUSIC algorithm for DOA estimation, we assume the signal from D sources is collected using an array of M receivers. No constraints are placed on the sampling rate or shape of the array. The signal from D sources received on the array is modeled by the following linear equation:

$$\begin{bmatrix} Y_1 \\ Y_2 \\ \vdots \\ Y_M \end{bmatrix} = [a(\theta_1) \quad a(\theta_2) \quad \dots \quad a(\theta_D)] \begin{bmatrix} X_1 \\ X_2 \\ \vdots \\ X_D \end{bmatrix} + \begin{bmatrix} \epsilon_1 \\ \epsilon_2 \\ \vdots \\ \epsilon_M \end{bmatrix} \tag{5.1}$$

where Y are the received signals, X are the signal parameters, ϵ are additive noise, and $a(\theta_i)$ are the steering vectors, i.e. the response seen on the array due to a signal incident from the θ_i direction. The MUSIC algorithm consists of five steps. First, given the signal Y, the covariance matrix is computed

$$S = YY^* = AXX^*A^* + \epsilon\epsilon^* \tag{5.2}$$

where $(\cdot)^*$ is the conjugate-transpose. Second, the eigen decomposition of the covariance matrix is computed, which results in a set of eigenvalues, λ, and eigenvectors, E. In [56] Schmidt showed that of the M eigenvalues, there will be D dominant eigenvalues with large values that correspond to the signal subspace and N eigenvalues with minimal values that correspond to the noise subspace. The third step is to separate the noise

subspace of the eigenvectors, E_N, which corresponds to the N minimal eigenvalues. Fourth, the pseudo spectrum is computed by projecting the noise subspace, E_N, in to the continuum of steering vectors, $a(\theta)$, as follows:

$$P_{MU}(\theta) = \frac{1}{a^*(\theta)E_N E_N^* a(\theta)}. \tag{5.3}$$

The noise subspace is known to be orthogonal to the signal subspace, therefore the projection in (5.3) will result in a near-zero value when $a(\theta)$ corresponds to a signal direction. The result of taking the inverse of the projection is a spectrum with very sharp peaks in the signal directions and no sidelobes. The fifth and final step of the MUSIC algorithm is to solve for the signal parameters, X, in the direction of the peaks in the pseudo spectrum. The resulting equation is linear, so this step can be easily done by the linear least-squares algorithm.

5.3 DOA ESTIMATION THROUGH A PIPE USING MUSIC

To apply MUSIC for DOA estimation through a pipe requires that the steering vectors, $a(\theta)$, properly account for the transmission through a pipe. To demonstrate the performance of MUSIC through a pipe a simulation is performed. Two 10 GHz sources are located 20° apart in azimuth on one side of a pipe. The pipe has a radius of 5 cm and length of 50 cm. The sources are modulated with a random binary signal that is observed by a 20 element linear array with half-wavelength spacing on the other side of the pipe. The modulation is necessary to decorrelate the sources. The transmission data and the

steering vectors, $a(\theta)$, are simulated using the modal approach used previously. The covariance matrix of the received signal is computed using (5.2) and the eigen decomposition of the signal is found. Fig. 5.1 shows the magnitude of the resulting eigenvalues in dB. From Fig. 5.1 it is clear that there are two dominant eigenvalues, which is expected since there are two sources. The remaining 18 eigenvalues correspond to the noise subspace. The noise subspace is separated from the eigenvectors and the pseudo spectrum is computed using (5.3). Fig. 5.2 shows the pseudo spectrum of the received signal. The pseudo spectrum shows two sharp peaks at the azimuth positions of the two sources.

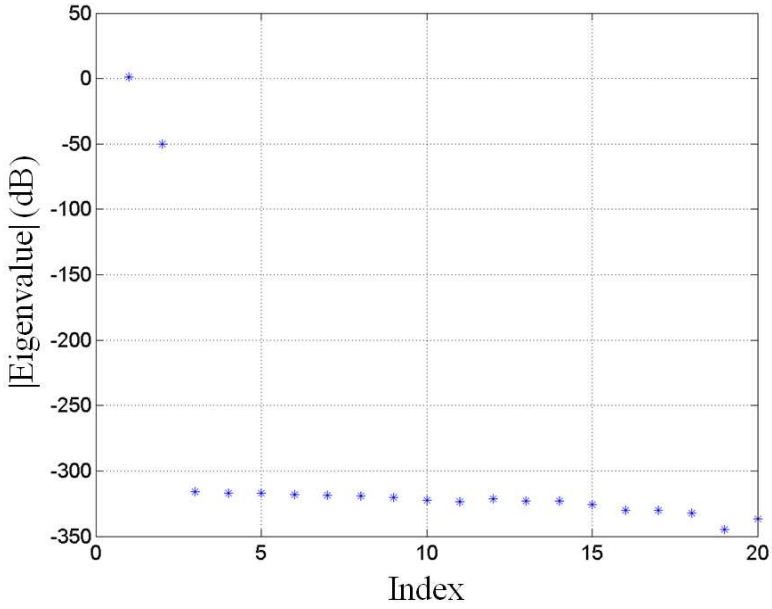

Figure 5.1: Eigenvalues from through-pipe simulation.

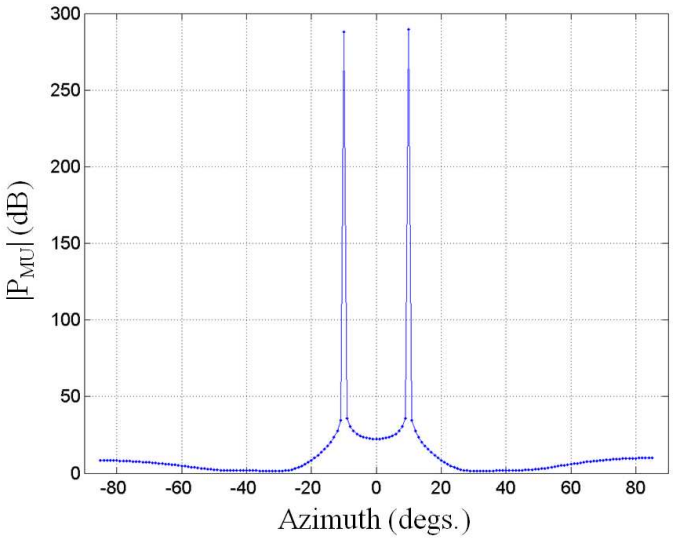

Figure 5.2: MUSIC pseudo spectrum for DOA estimation through a pipe.

For comparison, the signal data is also processed using a matched filter for DOA estimation. Fig. 5.3 shows the DOA result of processing the simulated data using a matched filter. It is clear that the two targets are not resolved by the matched filter. The simulation results show that MUSIC does indeed perform well for data collected through a pipe and that the resolution should be much improved over the performance of the matched filter results.

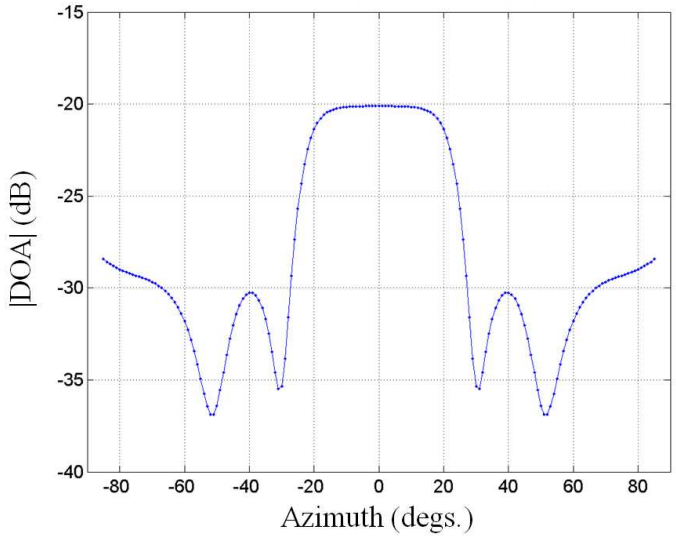

Figure 5.3: Matched filter for DOA estimation through a pipe.

At this point it is appropriate to point out one difference when using MUSIC with a pipe channel rather than free space. When using MUSIC in free space, the number of targets, D, that can be detected by an array of M elements is $M-1$. If the number of targets exceeds $M-1$, then it will not be possible to find the noise subspace. This condition is still true when propagating through a pipe channel, however the physics of the pipe channel introduces an additional constraint on the number of targets that can be detected. The number of targets that can be detected through a pipe channel must also be less than the number of propagating modes supported by the pipe. This property of the pipe channel is explained through the rank of the pipe channel. For D targets the covariance matrix is expected to have a rank of D. The rank of the transfer function that defines transmission through a pipe is equal to the number of propagating modes, K. If D is greater than the number of modes, K, then after transmission through the pipe, the covariance matrix will be reduced to a rank of K instead of the expected rank of D. This

results in fewer dominant eigenvalues, which leads to an incorrect extraction of the noise subspace. Therefore, when propagating through a pipe, the number of targets MUSIC can discriminate is limited to the smaller of $M-1$ and K.

The previous discussion was on the one-way DOA estimation problem from sources. Next, the MUSIC algorithm is applied to the two-way radar problem of DOA estimation of targets based on backscattering data collected through a pipe. Up to now it has been assumed that the sources are decorrelated. In the above example, binary modulation was used to decorrelate the sources. However, in the case of radar, the targets are inherently correlated since they are illuminated simultaneously by the same source. Spatial smoothing is a useful method for decorrelation that has been previously used on backscattering data in free space [59] and through-wall radar imaging [60]. Spatial smoothing operates on monostatic backscattering data collected along a uniformly sampled linear array. The method divides the array into a set of sub-arrays, computes the covariance matrix of each sub-array, and then estimates the global covariance matrix by averaging the covariance matrices of the sub-arrays. For spatial smoothing to work, the array must exhibit shift invariance, i.e. each sub-array differs from other sub-arrays by a complex constant. In the case of monostatic backscattering collected through a pipe, this is not the case. Therefore, it is not possible to use spatial smoothing for decorrelation and other methods of decorrelation must be used. It is possible to decorrelate the targets using transmitter diversity, such as what is done in Multiple-Input Multiple-Output (MIMO) radar [62]. MIMO radar involves the collection of bistatic backscattering data, which makes it possible to decorrelate the targets. The number of targets than can be

decorrelated is equal to the number of transmitters used. If the response due to two transmitters is measured, then at most two point scatterers could be detected. If the full bistatic response of an M element array is measured, which results in an $M \times M$ matrix, then M targets can be decorrelated. However, it is still only possible to detect at most $M - 1$ targets using MUSIC.

Given the need to decorrelate the targets by collecting bistatic data, it is not possible to use a synthetic aperture approach for data collection. Fig. 5.4 shows the problem geometry, which is the same data collection scheme used in the beamforming method. A point scatterer is described by polar coordinates $\bar{r}(r, \theta)$ with respect to the right-end of the pipe. It is assumed that wideband bistatic data are collected from an array at M elements. The position of each element is described by polar coordinates $\bar{r}_m(r_m, \theta_m)$ where the origin is located at the left-end of the pipe.

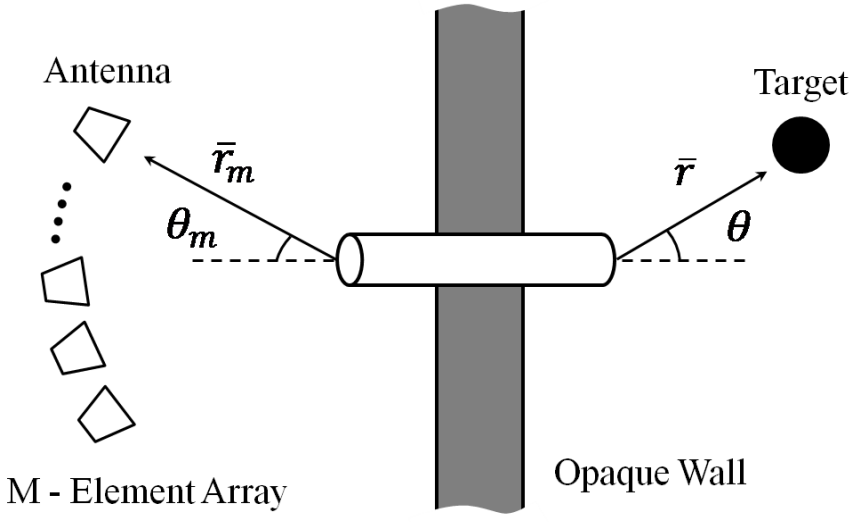

Figure 5.4: Data collection scheme for MUSIC.

The objective is to obtain the range, r, and azimuth, θ, positions of the point scatterer. The method here first estimates the azimuth direction of arrival (DOA) using MUSIC for each frequency, and then applies an inverse Fourier transform to obtain the range position. To apply MUSIC to the DOA estimation problem, single-frequency bistatic backscattered data collected through the pipe are divided into the three mechanisms shown in Fig. 5.5. The backscattering is modeled using the following linear equation:

$$\begin{bmatrix} Y_{1,1} & Y_{1,2} & & Y_{1,N} \\ Y_{2,1} & Y_{2,2} & & Y_{2,N} \\ \vdots & & \cdots & \vdots \\ Y_{M,1} & Y_{M,2} & & Y_{M,N} \end{bmatrix}$$
$$= [a(\theta_1) \quad a(\theta_2) \quad \ldots \quad a(\theta_D)] \begin{bmatrix} b_1(\theta_1)\cdot X_1 & b_2(\theta_1)\cdot X_1 & & b_N(\theta_1)\cdot X_1 \\ b_1(\theta_2)\cdot X_2 & b_2(\theta_2)\cdot X_2 & \ldots & b_N(\theta_2)\cdot X_2 \\ \vdots & & & \vdots \\ b_1(\theta_D)\cdot X_D & b_2(\theta_D)\cdot X_D & & b_N(\theta_D)\cdot X_D \end{bmatrix} \tag{5.4}$$

where $Y_{m,n}$ is the received signal on the mth element of the array from the nth transmitter. In (5.4), the three scattering mechanisms illustrated in Fig. 5.5 are present. The one-way propagation from the nth transmitter to the dth target are accounted for by the complex constant $b_n(\theta_d)$. The complex target parameters, X_d, account for the scattering strength of the point scatterer and the two-way propagation from the end of the pipe to the target. One-way propagation from the array to the pipe and the one-way transmission through the pipe are accounted for by the steering vectors $a(\theta_i)$. For DOA estimation, MUSIC is applied as before without modification. However, the target

parameter estimates given by MUSIC include the transmitter weights, $b_n(\theta_d)$. Therefore, to recover the correct target parameters, X_d, the result of MUSIC must be divided by the transmitter weights. The result of MUSIC will be an estimate of the azimuth position, θ_d, and the complex scattering strength associated with the backscattering from a target in that direction, X_d.

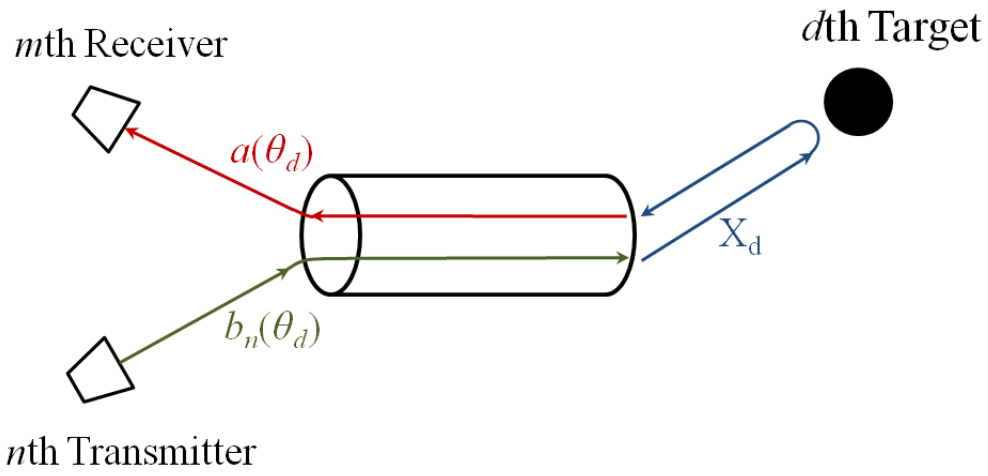

Figure 5.5: Bistatic scattering model.

The imaging procedure is summarized in three steps. 1) Wideband bistatic backscattering data are collected through the pipe for M receiver positions and N transmitter positions. 2) For each frequency, MUSIC is used to estimate the azimuth positions of the target and the target parameters. The results of MUSIC are placed in a vector, the target parameter estimations are placed at their corresponding azimuth positions and zeros are filled in for all other azimuth positions under consideration. These vectors are then stacked to form a matrix of frequency against azimuth position. 3) For each azimuth position of interest an inverse Fourier transform is taken across frequency

to give the range position of the target. The result is a two-dimensional image in azimuth and range.

5.4 MUSIC IMAGING RESULTS

To demonstrate the method outlined above, a set of simulations and measurements are performed. The proposed imaging method using MUSIC is compared to an imaging procedure using a matched filter for DOA estimation. To use a matched filter for DOA estimation step 2 of the method that uses MUSIC is replaced with a matched filter approach. The pipe used for simulations and measurements has a radius of 2.55 cm and length of 76.2 cm. The array has 9 elements located at a radius of 0.45 cm and evenly spaced in azimuth from -40° to 40°. The array forms a circular arc centered at boresight with respect to the pipe. Backscattering data are collected from 12 to 18 GHz. First, bistatic backscattering data for a single point scatterer located at $\bar{r}(2.5\mathrm{m}, 0°)$ are simulated using the modal approach. Backscattering data are simulated for three transmitter positions at -10°, 0°, 10° azimuth. Backscattering from the pipe is not simulated, i.e. only backscattering from the point scatterer is considered. The steering vectors, $a(\theta)$, and the transmitter weights, $b(\theta)$, are also simulated using the modal code. The steering vectors are simulated for 69 azimuth positions between -85° and 85°, which define the extent and sampling rate of the pseudo spectrum computed via (5.3). Figs. 5.6(a) and 5.6(b) show the resulting DOA estimations versus frequency using MUSIC and a matched filter respectively. The results show that both methods correctly identify the azimuth location of the target, however the matched filter exhibits sidelobes and a

much wider beamwidth in comparison to MUSIC. To form an image the inverse Fourier transform is taken across frequency and the results for MUSIC and the matched filter are shown in Figs. 5.6(c) and 5.6(d) respectively. Prior to taking the inverse Fourier transform, the frequency data are windowed with a Hamming window in order to suppress sidelobes at the expense of a broader peak in range. The final images further illustrate the superior localization and sidelobe performance from MUSIC as compared to a matched filter.

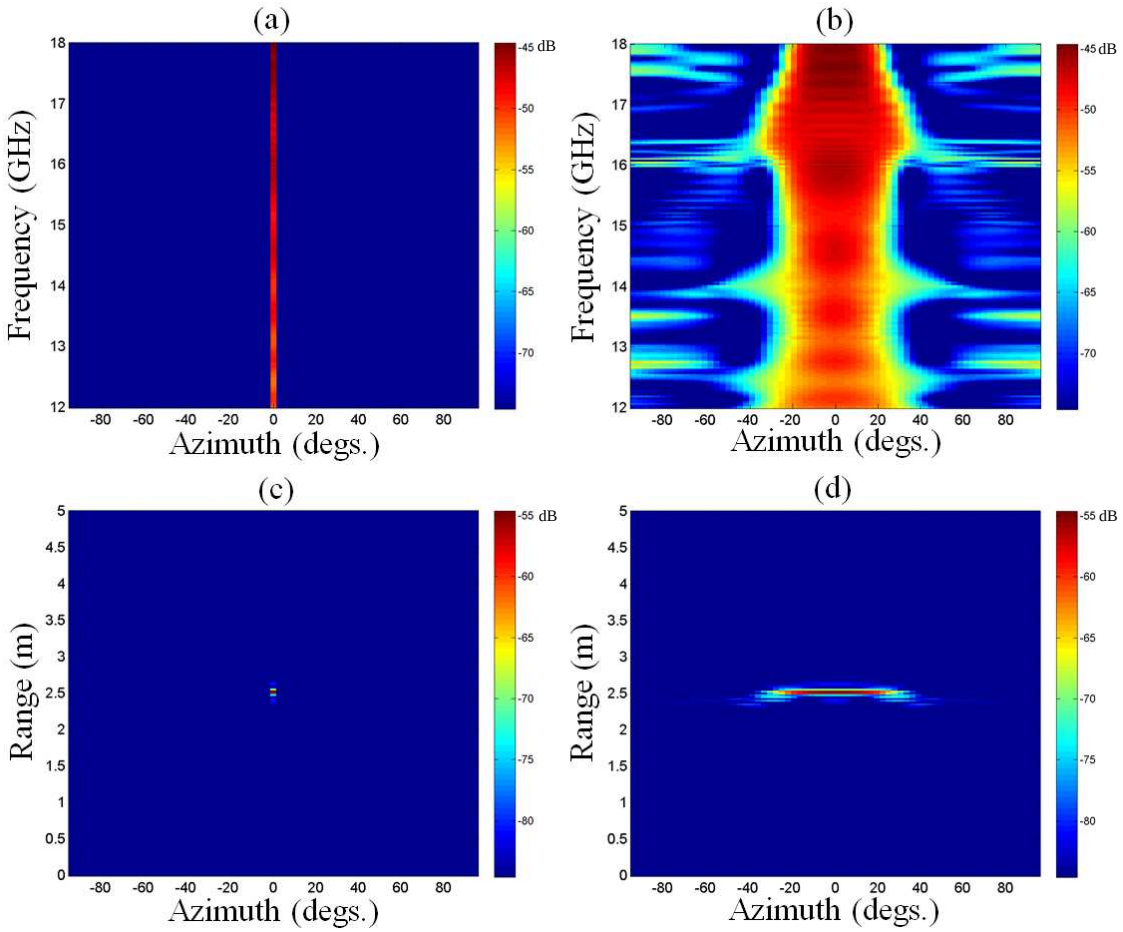

Figure 5.6: Simulated backscattering data with DOA estimation and image using (a) & (c) MUSIC and (b) & (d) a matched filter.

Next, backscattering data are measured in the laboratory as described in Appendix A. The pipe geometry and array geometry are the same as in simulation. A corner reflector with an edge length of 5 cm is used as a target and placed at $\bar{r}(2.5\text{m}, -15°)$. Three transmitter positions at -10°, 0°, 10° azimuth are measured. Again, The steering vectors, $a(\theta)$, and the transmitter weights, $b(\theta)$, are simulated using the modal code. This is analogous to the previous chapter, where measurement data are processed with a simulated basis. The alternative would be to perform a calibration measurement to determine $a(\theta)$ and $b(\theta)$. Background subtraction is used in conjunction with time gating in order to suppress backscattering from the pipe and clutter. Figs. 5.7(a) and 5.7(b) show the MUSIC and matched filter DOA versus frequency results. As before, the MUSIC algorithm gives much better azimuth localization than the matched filter. The final images are formed and shown in Figs. 5.7(c) and 5.7(d) for MUSIC and the matched filter respectively. The image in Fig. 5.7(c) shows substantial sidelobes in range, which is due to the azimuth estimate of the target varying slightly with frequency as seen in Fig. 5.7(a). However, the sidelobes are more than 15 dB lower than the target peak and the target location is clearly visible. The measurement images further support that MUSIC provides better localization than a matched filter.

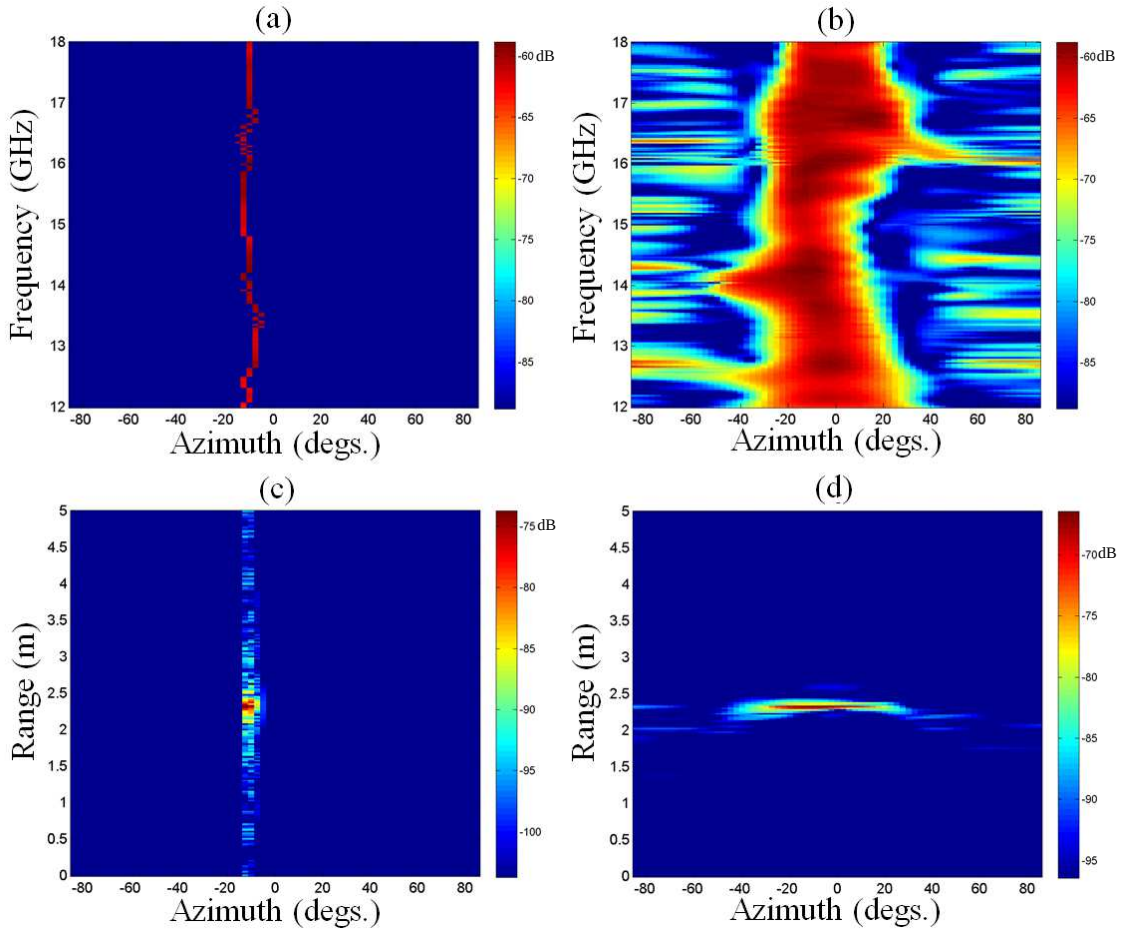

Figure 5.7: Single target measured backscattering data with DOA estimation and image using (a) & (c) MUSIC and (b) & (d) a matched filter.

Next, measurements are made with two corner reflectors located at $\bar{r}(1.8\text{m}, -25°)$ and $\bar{r}(3.1\text{m}, 25°)$. Figs. 5.8(a) and 5.8(b) show the DOA results using MUSIC and a matched filter. In Fig. 5.8(b) rapid oscillations are observed in frequency, which is interference caused by the range offset of the two targets. Figs. 5.8(c) and 5.8(d) show the final images where both targets are clearly seen. As before, the MUSIC image has increased sidelobes in range and superior localization compared to the matched filter.

These results also show that backscattering data from two targets can be successfully decorrelated using a bistatic data collection scheme.

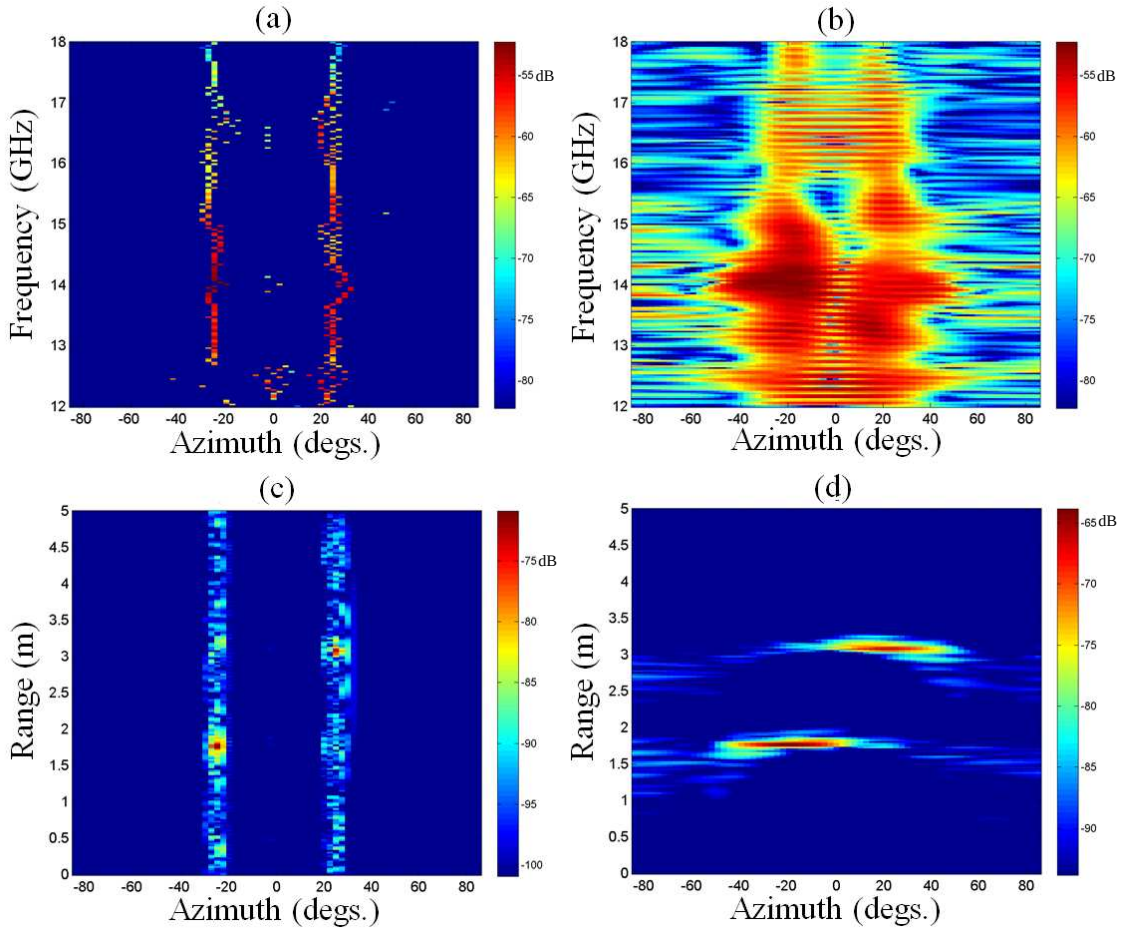

Figure 5.8: Two target measured backscattering data with DOA estimation and image using (a) & (c) MUSIC and (b) & (d) a matched filter.

The final demonstration is to show the superresolving capabilities of MUSIC. Noiseless backscattering data from two targets are simulated using the modal code. The targets are placed 30° apart and 1 m down-range. Figs. 5.9(a) and 5.9(b) show the DOA estimates for MUSIC and a matched filter respectively. The results show that MUSIC successfully identifies the two targets whereas it is not clear that two targets are present

in the matched filter result. The final images in Figs. 5.9(c) and 5.9(d) further support this, in that MUSIC processing shows two point scatterers and matched filter processing only shows one discernable peak.

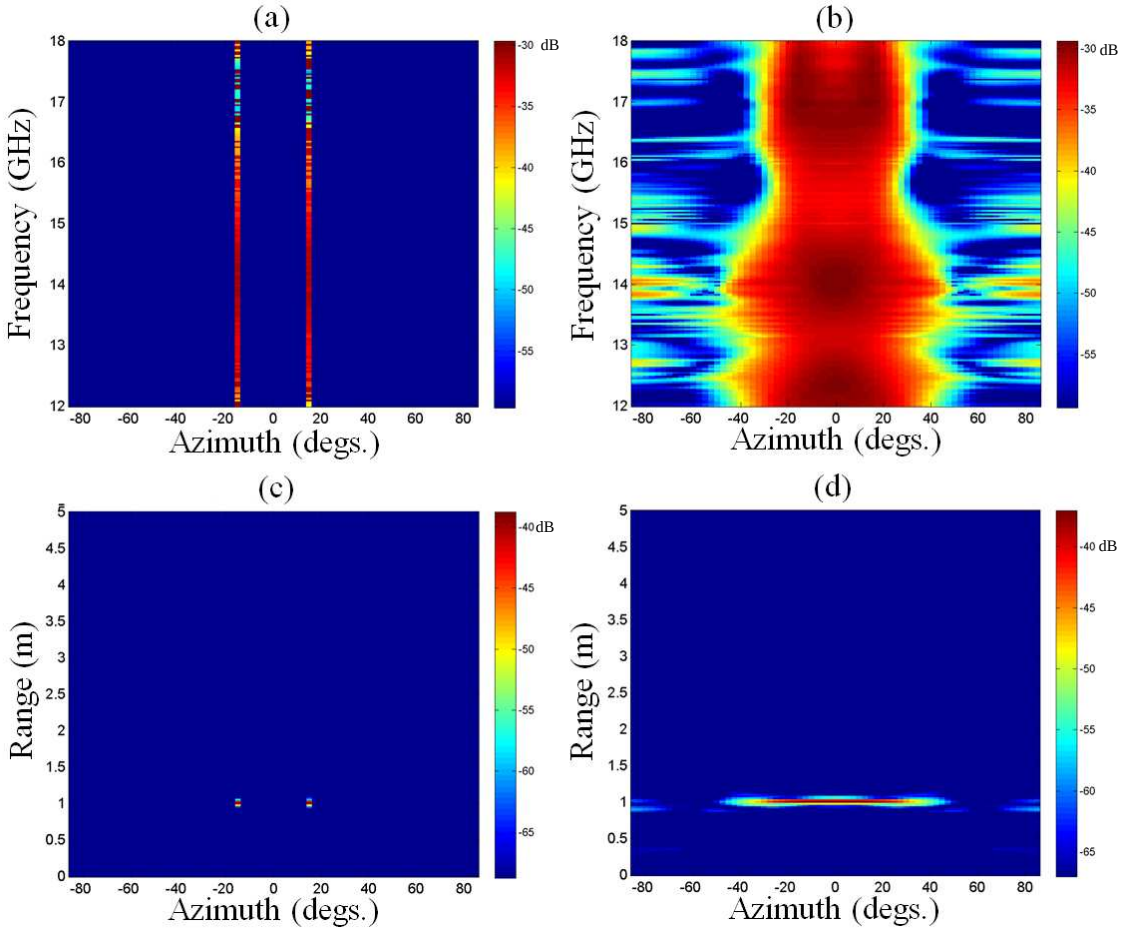

Figure 5.9: Simulated supperresolution demonstration with DOA estimation and image using (a) & (c) MUSIC and (b) & (d) a matched filter.

5.5 UNCERTAINTY EFFECTS ON MUSIC

The effects of uncertainty on the performance of MUSIC are explored through simulation. The two dominant sources of uncertainty are additive noise and array

positioning errors. Additive noise can obscure the signal, which degrades the performance of MUSIC. Array positioning errors create mismatch between the processing bases and the physical channel, which is also detrimental to MUSIC's performance. First, the effects of additive noise on DOA estimation are investigated followed by a study of the effects of positioning error.

To model additive noise, white Gaussian noise is added to the simulated backscattering data. First, the noise performance of MUSIC with respect to pipe radius is simulated. The simulation consists of three target positions of 0°, 45°, and 60° in azimuth and 1m from the target in each case. The array for each simulation contains 9 elements equally spaced in azimuth from -40° to 40° and 45cm from the pipe opening. Pipes with a length of 50cm and with radii of 2.5cm, 5cm, and 10cm are simulated. A Monte Carlo simulation is run with 5000 simulations for each noise power level ranging from -80 to 0 dB. The transmit power of each array element is set to unity. The DOA estimation error is measured for each run and averaged over all the runs for each noise power level. The results of the Monte Carlo simulations are shown in Fig. 5.10. Figs. 5.10(a), 5.10(b), and 5.10(c) are for a target at 0°, 45°, and 60° respectively. In addition to the DOA estimation error for MUSIC, the DOA estimation error of a random guess is also simulated and shown in Fig. 5.10. It is observed that the DOA estimation error tends to saturate to a random guess, indicating that MUSIC no longer works. Two conclusions can be drawn from Fig. 5.10. First, a target closer to 0° is easier to detect in the presence of noise and becomes increasingly more difficult to detect as the target moves off boresight. This is due to the fact that as the target moves off boresight the target is illuminated by a weaker

signal, which results in weaker scattering that is more susceptible to interference from noise. Second, a larger pipe improves the detection performance in the presence of noise because more of the scattered power from the target is captured by the pipe.

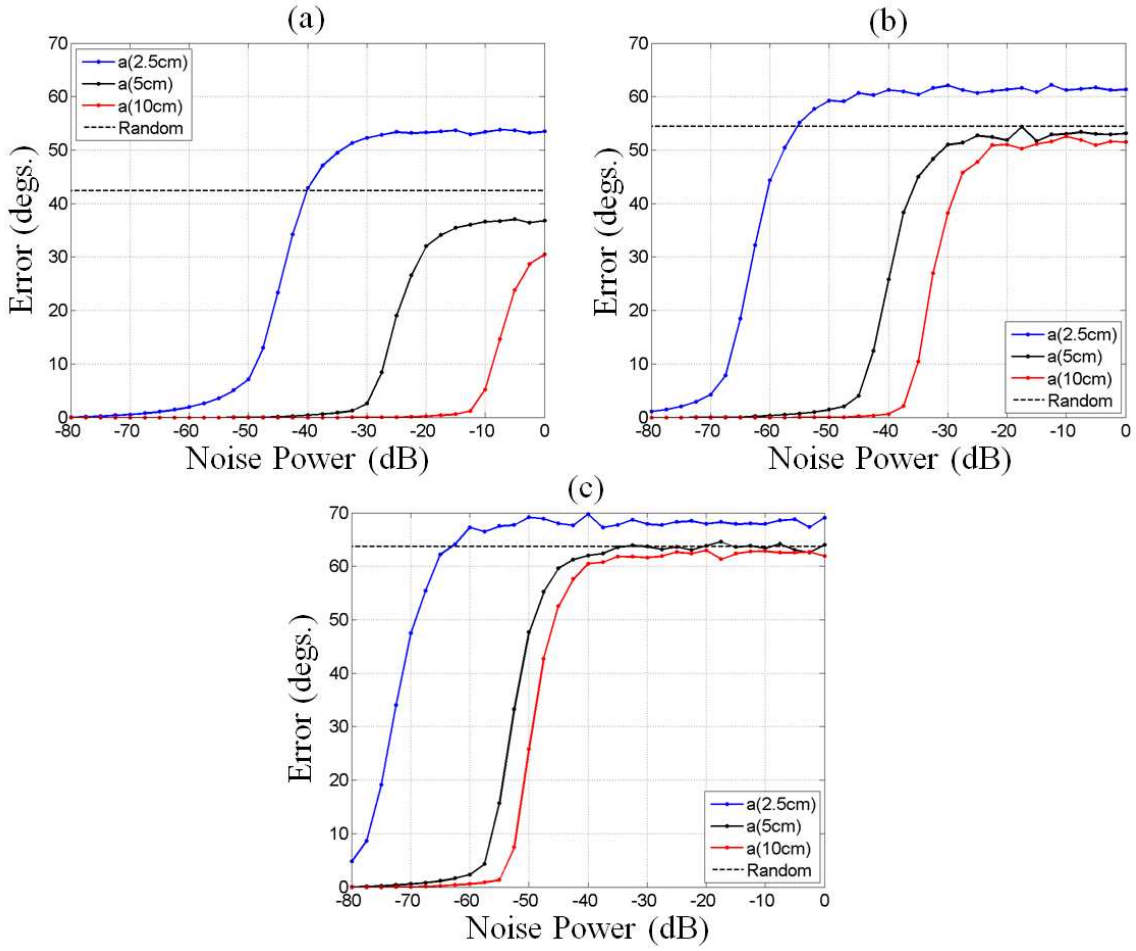

Figure 5.10: MUSIC DOA estimation error in the presence of noise with respect to pipe radius for a target located at (a) 0°, (b) 45°, and (c) 60° in azimuth.

Next, the effect of array sampling on the noise performance of MUSIC is simulated. The Monte Carlo simulation is performed the same as before. However, the pipe radius is set to 5cm with a length of 50cm and the extent of the array in azimuth is

set from -40° to 40° while the number of elements in the array was varied. The array elements are equally spaced in azimuth and the number of array elements is set to 9, 17, and 33. The Monte Carlo simulation results are shown in Figs. 5.11(a), 5.11(b), and 5.11(c) for a target at 0°, 45°, and 60° in azimuth respectively. Again it is observed that the detection of targets as they move away from boresight is increasingly more difficult in the presence of noise. It addition, it is observed that increasing the number of elements also improves DOA estimation performance. This is expected since more data samples improve the robustness to random noise.

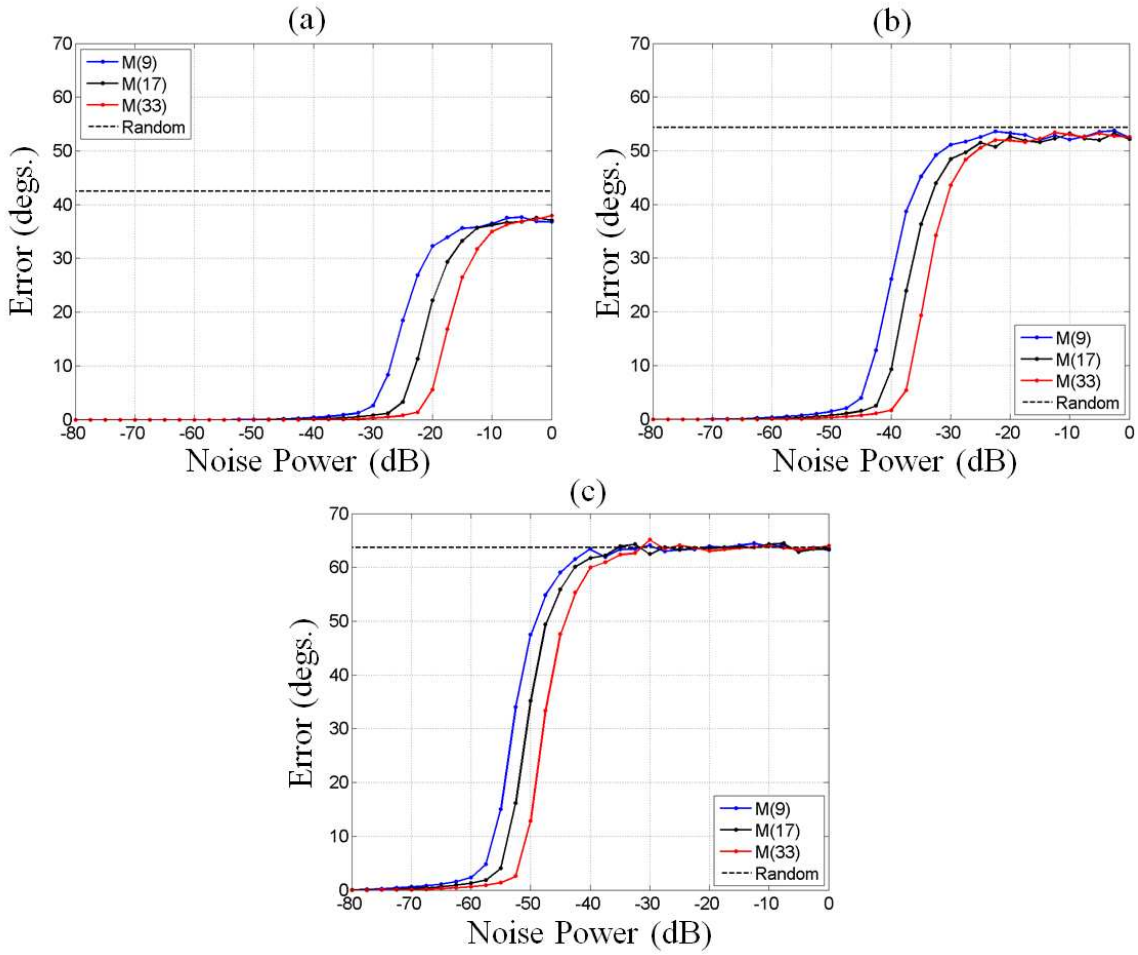

Figure 5.11: MUSIC DOA estimation error in the presence of noise with respect to array sampling for a target located at (a) 0°, (b) 45°, and (c) 60° in azimuth.

The third and final Monte Carlo simulation is to determine the effect of the array extent on noise performance. Here, the number of elements in the array is set to 17 and the elements are equally spaced in azimuth from -20°:20°, -40°:40°, and -70°:70°. The pipe radius is remains 5cm and the length is 50cm. Figs. 5.12(a), 5.12(b), and 5.12(c) show the simulation results for a target at 0°, 45°, and 60° in azimuth respectively. The

key observation here is that the detection of targets away from boresight in the presence of noise can be improved by increasing the azimuth extent of the array.

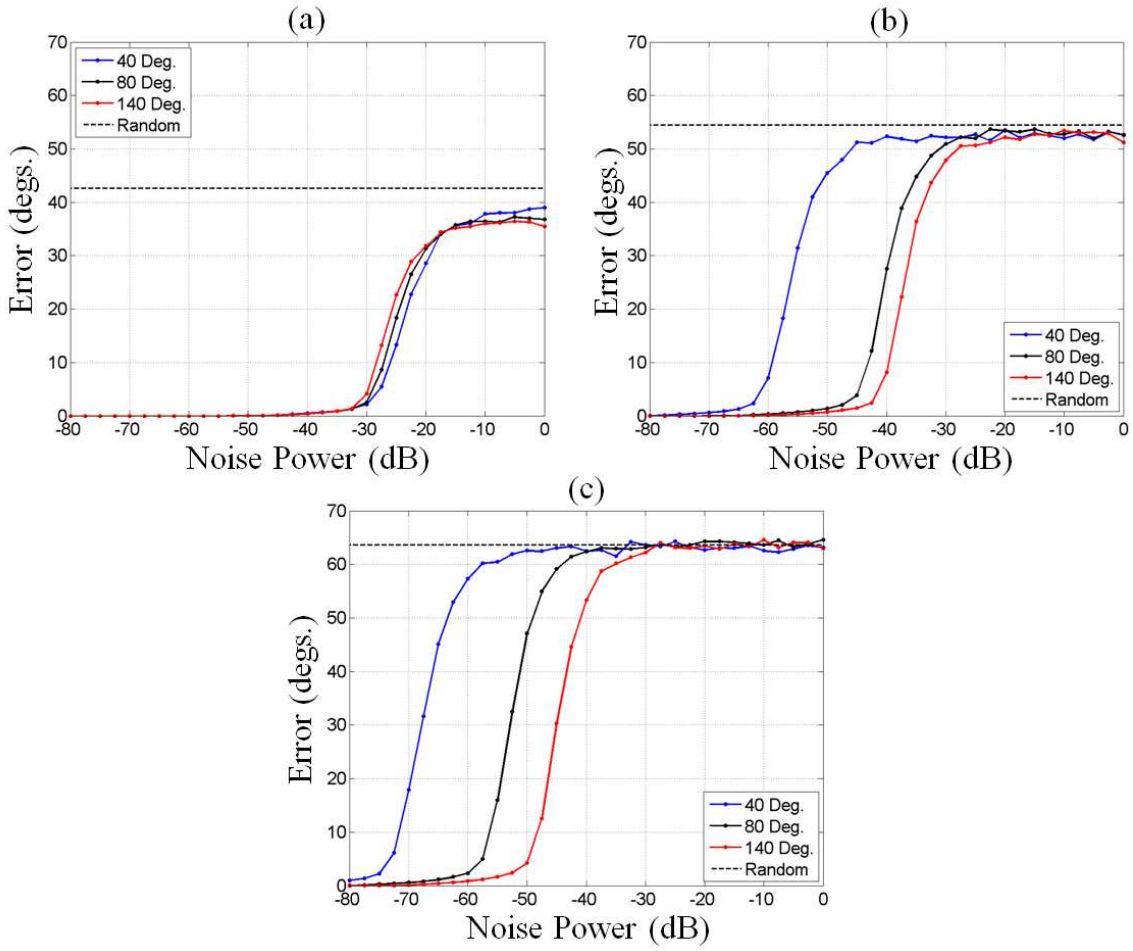

Figure 5.12: MUSIC DOA estimation error in the presence of noise with respect to array extent for a target located at (a) 0°, (b) 45°, and (c) 60° in azimuth.

The effect of array positioning error on the DOA estimation performance of MUSIC is also studied. It was found that MUSIC is most susceptible to the accuracy of the radial position of the array elements with respect to the pipe, i.e. the distance from the transmitter to the pipe. To simulate array positioning error, the radial positions of the

array elements are randomized about a mean radius of 45cm and the data are processed with a set of bases that assumes the array is located exactly on the 45cm circle. The array element positions are varied by selecting from a set of normally distributed random numbers with a variance that varies from 0 to a wavelength, λ. As before, the DOA estimation performance with respect to radius, array sampling, and array extent are explored through Monte Carlo simulations using the same simulation parameters. Fig. 5.13 shows the simulation results for the performance of MUSIC in the presence of positioning errors with respect to pipe radius. The key result from Fig. 5.13 is that when the positioning error is above 0.2λ, the results degrade tremendously. Therefore, in order to have any chance of accurately detecting the target, positioning errors should be kept below 0.2λ. In Fig. 5.13(a), when the target is located at 0° in azimuth, the DOA estimation error decreases with increasing pipe size and for a sufficiently large pipe there is negligible error. However, when the target is moved away from boresight, as in Figs. 5.13(b) and 5.13(c), the position error has a more substantial effect on DOA estimation error. It is also observed that the pipe radius affects the maximum error observed, but does not improve the amount of positioning error MUSIC will tolerate.

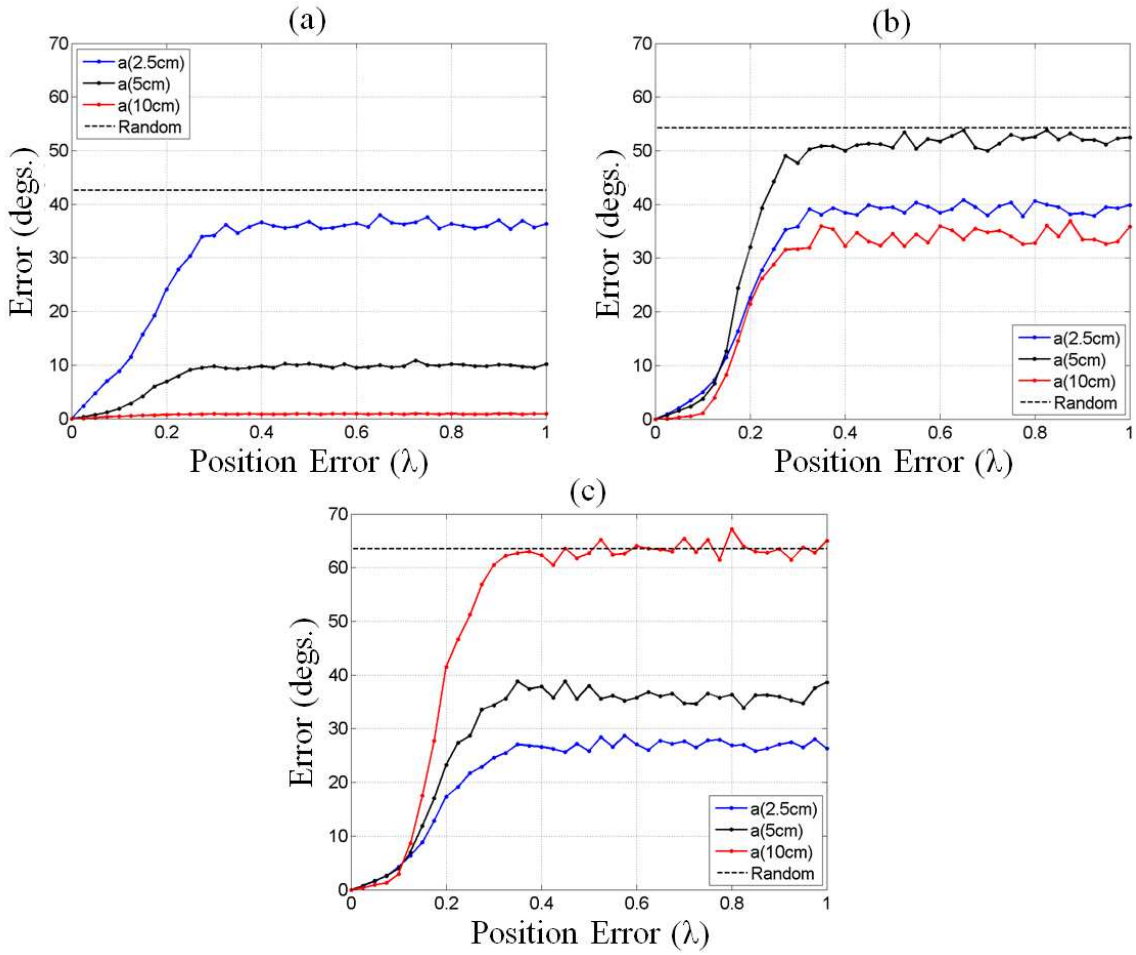

Figure 5.13: MUSIC DOA estimation error in the presence of positioning error with respect to pipe radius for a target located at (a) 0°, (b) 45°, and (c) 60° in azimuth.

Next, the effect of array sampling on the DOA estimation performance of MUSIC with positioning errors is simulated. Fig. 5.14 shows the results for the three target positions. In Fig. 5.14, when the positioning error is above 0.2λ there is little chance of accurately acquiring the target position. When the positioning error is below 0.2λ, it is observed that increasing the number of samples improves the DOA performance.

Therefore, increasing the number of elements improves the DOA estimation accuracy in the presence of position errors when using MUSIC.

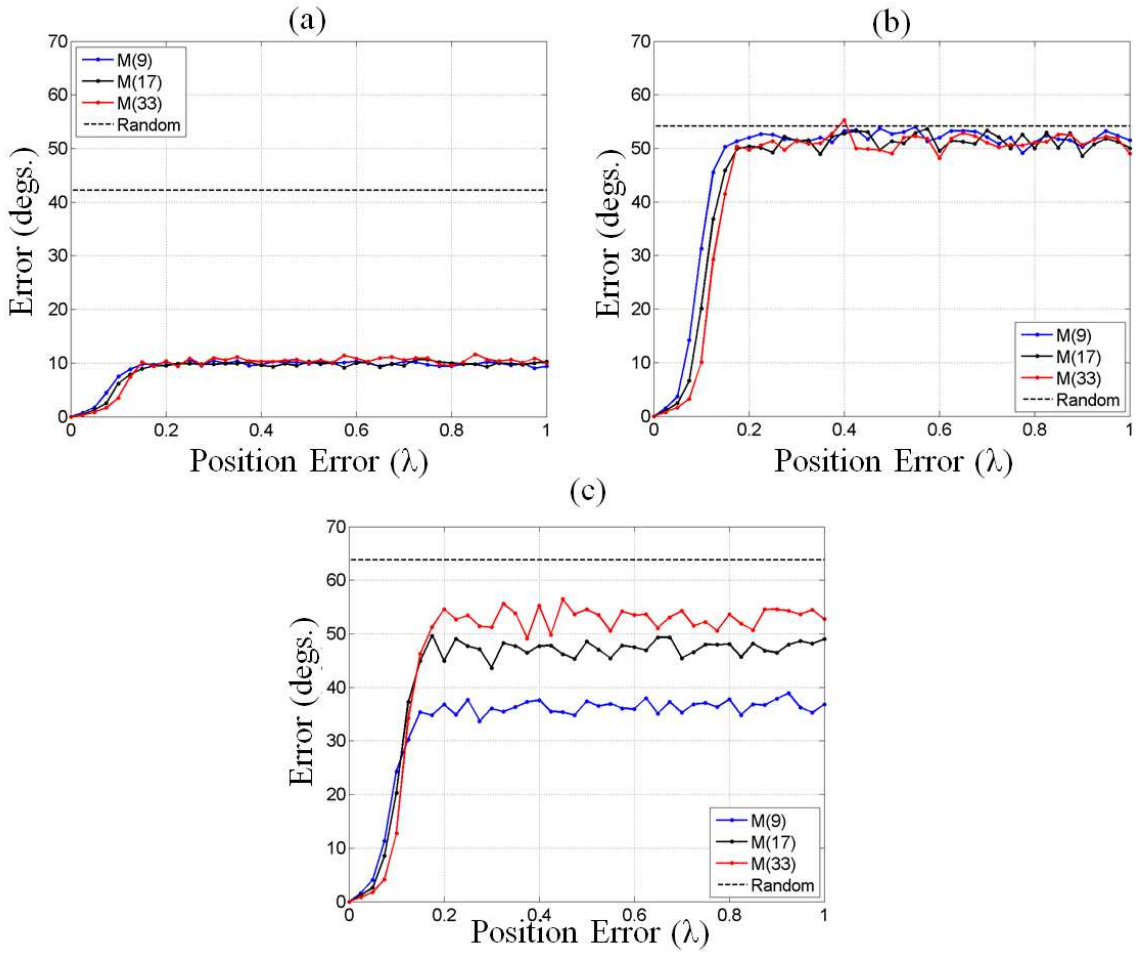

Figure 5.14: MUSIC DOA estimation error in the presence of positioning error with respect to array sampling for a target located at (a) 0°, (b) 45°, and (c) 60° in azimuth.

The final simulation shows the effect of the array extent on MUSIC's performance with positioning error. The Monte Carlo simulation results are shown in Fig. 5.15. In Fig. 5.15(a), when the target is at boresight, it noted that the DOA estimation error is acceptable for a sufficiently large array. When the target is away from boresight,

Figs. 5.15(b) and 5.15(c), changing the extent of the array effects the maximum error observed, but does not necessarily lead to improved DOA estimation accuracy.

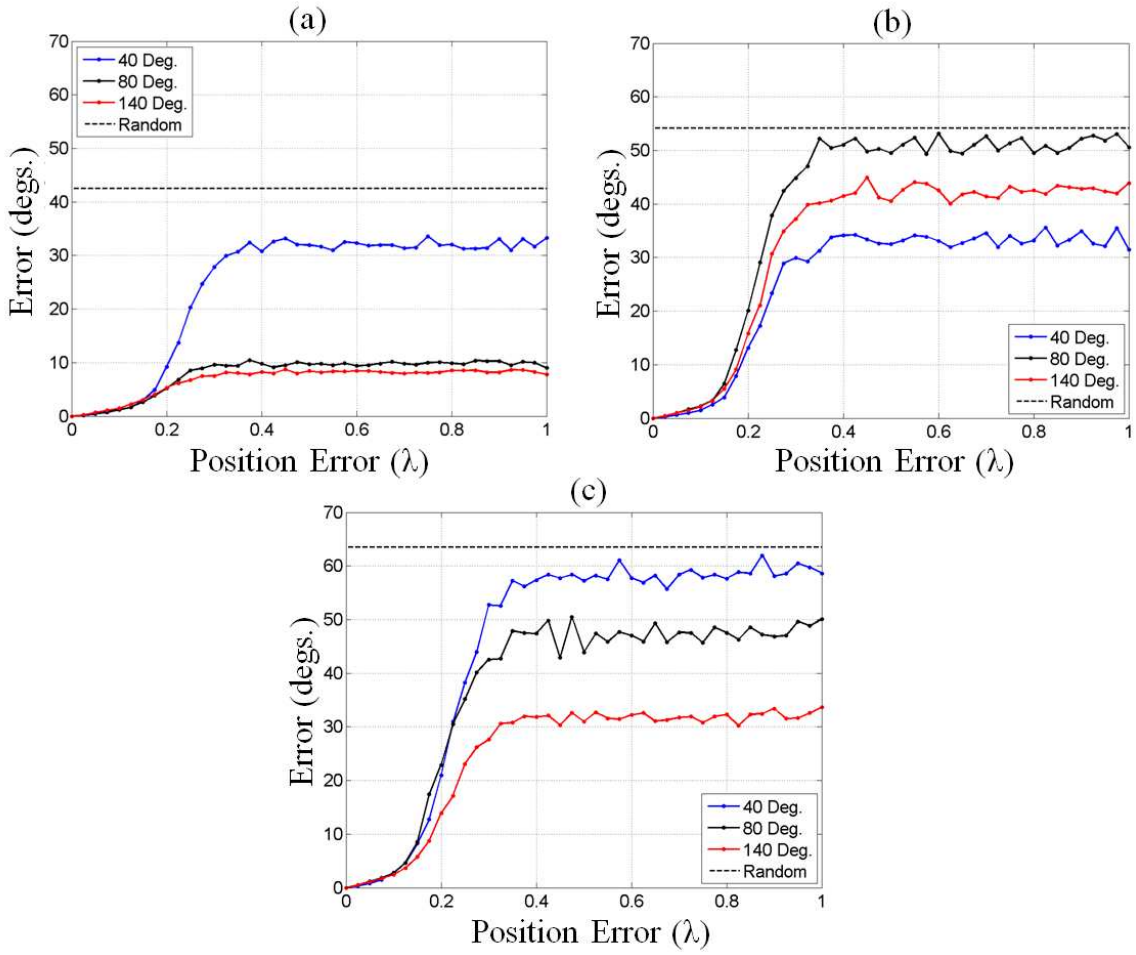

Figure 5.15: MUSIC DOA estimation error in the presence of positioning error with respect to array extent for a target located at (a) 0°, (b) 45°, and (c) 60° in azimuth.

5.6 CONCLUSIONS

In this chapter the MUSIC algorithm was applied to improve the azimuth resolution while imaging through a pipe. The presence of the pipe channel was found to influence the MUSIC algorithm in two ways. First, the number of targets MUSIC can

detect is limited by the number of propagating modes in the pipe. Second, spatial smoothing cannot be used to decorrelate targets, therefore, it is necessary to collect bistatic backscattering data to decorrelate targets. The imaging method was then demonstrated on simulated and measurement backscattering data, using a simulated set of bases to process all of the data. It was shown that MUSIC provides superior resolution in comparison with a matched filter.

Finally, the effects of noise and positioning errors on MUSIC's DOA estimation performance were explored through Monte Carlo simulations. It was found that additive noise makes it more difficult to detect targets that are at wide angles with respect to the boresight of the pipe. To combat the negative effects of additive noise it was found that using a pipe with a larger radius, increasing the array sampling, and increasing the array extent all help improve the DOA estimation performance of MUSIC. In the presence of positioning errors, it was found that MUSIC does not tolerate errors above 0.2λ. Below an error of 0.2λ it was found that larger radius and array sampling improve DOA estimation performance. However, it was found the array extent had little influence.

Chapter 6: Application of Compressed Sensing Techniques to Imaging Through a Pipe

6.1 INTRODUCTION

In the previous chapter, MUSIC was applied to the problem of DOA estimation through a pipe to achieve enhanced resolution and localization in comparison with a matched filter method. However, due to the need to decorrelate the backscattering from multiple targets, the MUSIC method required the collection of bistatic data. This is true for any algorithm that falls into this class of subspace methods, which are based on the covariance matrix. Recently, a solution framework known as compressed sensing (CS) has been proposed in the signal processing community that has shown superior localization to matched filter and least-squares solutions [63][64]. CS solutions are not based on the covariance matrix and therefore monostatic backscattering data can be used for processing. In this chapter, CS is applied to the problem of DOA estimation through a pipe in order to improve the cross-range resolution of the radar image using monostatic data. First, an overview of CS and its application in radar imaging is given in Section 6.2. Then, a method for applying CS to the problem of imaging through a pipe is presented in Section 6.3. Simulation and measurement results using the proposed method are presented in Section 6.4. The effect of noise on the performance of CS is explored in Section 6.5. Finally, a summary of the findings and conclusions are given in Section 6.6.

6.2 COMPRESSED SENSING OVERVIEW

We begin with an overview of CS and its application to radar imaging. In early 2006 Candès, Romberg, and Tao showed that exact image recovery could be achieved using sparse regularization operating on an incomplete set of Fourier samples [63]. At the time, sparse regularization of inverse problems had been previously demonstrated [65], however the key contribution from Candès et al. was that they were able to significantly undersample the data, effectively beating the Nyqust sampling criterion. A few months later Donoho coined the term compressed sensing and provided further theoretical insight and a framework for CS [64]. The motivation for CS was to reduce the number of measurements needed for exact recovery. To this end, CS was proposed with the goal of accurately solving an underdetermined inverse problem of the form

$$y = Ax \tag{6.1}$$

where $A \in \mathbb{C}^M$ is a matrix with dimensions $M < N$ and the solution to $x \in \mathbb{C}^N$ is sought from the measurements $y \in \mathbb{C}^M$. In addition it is assumed that the columns of A are normalized to unit L2-norm. Since the problem is underdetermined there exist multiple solutions that are equally correct, i.e. a solution space. One solution commonly used is the least-squares solution, which is equivalent to the minimum energy or L2-minimization of the form

$$\min_{\hat{x}} \|\hat{x}\|_2 \text{ subject to } A\hat{x} = y. \tag{6.2}$$

While the least squares solution provides a solution $\hat{x}$, it is generally not the exact solution to the x in (6.1), i.e. $\hat{x} \neq x$. If it is known a priori that x is sparse then it would be useful to pose the problem as the linear program

$$\min_{\hat{x}} \|\hat{x}\|_0 \text{ subject to } \|A\hat{x} - y\|_2 = 0 \tag{6.3}$$

where $\|\cdot\|_0$ is the L0 quasi-norm, which is equal to the number of non-zero elements in $\hat{x}$. The linear program in (6.3) would find a solution that contains the fewest number of non-zero elements. The key contribution from the CS literature [63][64] showed that, provided the matrix A obeys certain properties, the sparsest solution is the exact solution, i.e. $\hat{x} = x$. Therefore, (6.3) is well suited for finding the exact solution to problems where the solution is known or expected to be sparse. However, the linear program in (6.3) is an NP-hard algorithm, i.e. the solution can only be found through a brute force search over the solution space. In [66] it was shown through convex relaxation that the solution to (6.3) can be equivalently solved using the following L1-minimization:

$$\min_{\hat{x}} \|\hat{x}\|_1 \text{ subject to } \|A\hat{x} - y\|_2 = 0 \tag{6.4}$$

where $\|\cdot\|_1$ is the L1-norm. The advantage of posing the problem as an L1-minimization is that the problem is now a convex optimization problem that can be solved in practice [67]. There exist a variety of solution methods to solve the linear program in (6.4), e.g. basis pursuit [65], orthogonal matching pursuit [68], and Bayesian methods [69].

As previously mentioned, the solution to the linear program in (6.4) is the exact solution, $\hat{x} = x$, with high probability if the matrix A satisfies certain properties. The key property that A must satisfy is the restricted isometry property (RIP) [70]. The RIP is verified for a matrix A by considering all x such that $\|x\|_0 \leq s$ and finding the restricted isometry constant $\delta_s > 0$ that satisfies the following inequality:

$$(1 - \delta_s)\|x\|_2^2 \leq \|Ax\|_2^2 \leq (1 + \delta_s)\|x\|_2^2. \tag{6.5}$$

For sufficiently small δ_s, the matrix A is said to satisfy the RIP. For larger restricted isometry constants δ_s, exact recovery is less probable. In other words, the RIP says that every subset of the matrix A behaves approximately as an orthonormal basis. The RIP is a useful mathematical property, however, it is not practical to verify the RIP for large arbitrary matrices. A more useful property that is correlated with the RIP is the mutual coherence [71] of A which is defined as

$$\mu = \max_{i \neq j} \left| \langle a_i, a_j \rangle \right| \tag{6.6}$$

where a_i is the *i*th column of the matrix A and the mutual coherence is bounded by $0 \leq \mu \leq 1$ assuming normalization to unit L2-norm. Small values of the mutual coherence μ indicate that the matrix A is likely to satisfy the RIP. The computation of the mutual coherence in (6.6) is far more tractable that verifying the RIP.

With the theory and framework of CS in place, CS is a tool that could be used for a variety of applications. Recently, there has been considerable interest in both compressive measurement schemes and sparse regularization within the field of radar imaging. Some recent work on the application of compressed sensing (CS) to radar imaging can be found in [72]-[77]. As pointed out earlier, using an L1-minimization will recover the exact solution when the problem satisfies the RIP. The key issue for radar is whether the physical propagation channel will result in a matrix that satisfies the RIP. In free-space inverse synthetic aperture radar (ISAR) imaging, it is known that the imaging problem can be posed as a two-dimensional Fourier transform. In CS, it has been established that the Fourier basis satisfies the RIP [63], hence CS is directly applicable to free-space ISAR imaging. When the propagation channel is more complex and not modeled by a Fourier basis, it is not clear how well CS will perform. Nonetheless, good results using CS for radar imaging have been reported in ground penetrating radar [74] and through-wall imaging [75][77]. However, the bases used are only slight deviations of the Fourier basis. In this chapter, CS is applied to the pipe imaging problem, where the propagation characteristics of the pipe deviate significantly from the Fourier basis.

6.3 COMPRESSED SENSING THROUGH A PIPE

Fig. 6.1 shows the problem geometry where backscattering data are collected on the left-side of a pipe from a target on the right-side of the pipe. As before, it is assumed that the pipe is operated in an over-moded region and that it is embedded in an opaque wall. The target is modeled as a point scatterer that is described by polar coordinates $\bar{r}(r,\theta)$ with respect to the right-end of the pipe. Wideband monostatic data are collected along a baseline at N positions to form a synthetic aperture. The position of the transceiver at each data collection point is described by polar coordinates $\bar{r}_n(r_n,\theta_n)$ where the origin is located at the left-end of the pipe.

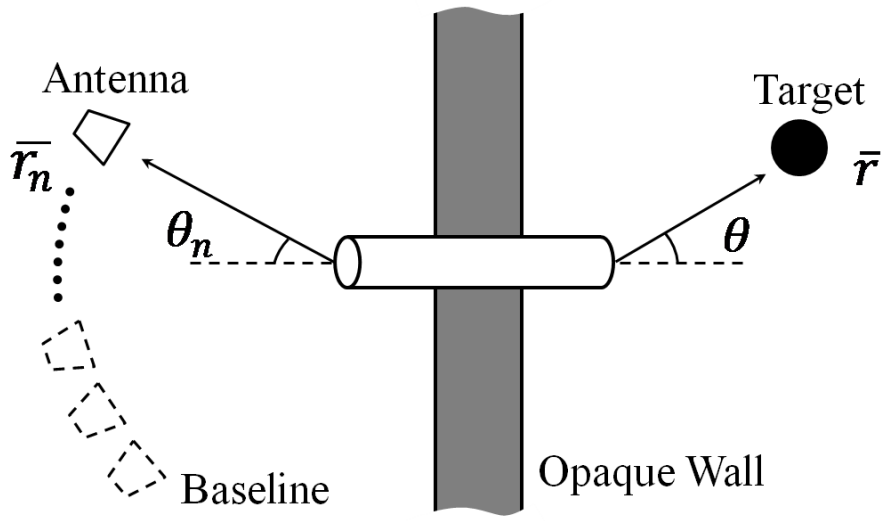

Figure 6.1: Problem geometry for imaging through a pipe using CS.

To image through the pipe, the azimuth, θ, and range, r, positions of the target are sought. As in the previous chapter, our method entails first estimating the azimuth direction of arrival (DOA) using CS for each frequency, and then applying an inverse

Fourier transform to obtain the range position. To apply CS to the DOA estimation problem, single-frequency backscattered data collected through the pipe are modeled using the following linear equation:

$$y = Ax + v \tag{6.7}$$

where the vector y represents the backscattered data at each transceiver position, the vector x contains the target strength for each azimuth direction of interest, the matrix A is our basis, and v is additive noise. The basis A accounts for the two-way propagation from the radar to the pipe and the two-way propagation through the pipe. For DOA estimation, the goal is to recover x from y in (6.7). If we assume x is sparse, i.e. there are few targets present in azimuth, and the noise is bounded by $\|v\|_2 \leq \epsilon$ then the DOA estimation problem can be solved using the linear program

$$\min_{\hat{x}} \|\hat{x}\|_1 \text{ subject to } \|A\hat{x} - y\|_2 \leq \epsilon \tag{6.8}$$

where $\hat{x}$ is the DOA estimation. Provided A satisfies the RIP, the linear program in (6.8) is solved exactly with high probability according to CS theory [78]. Our method for imaging through a pipe can thus be summarized in four steps: 1) Monostatic wideband backscattering data are collected for each transceiver position. 2) The basis, A, for the pipe channel is computed based on the transceiver position $\bar{r}_n(r_n, \theta_n)$ and known pipe dimensions. The columns of the basis are then normalized to unit L2-norm. 3) For each frequency, the direction of arrival, $\hat{x}$, is computed by solving (6.8) and the results are

stacked to form a frequency-azimuth matrix. 4) For each azimuth position of interest, the inverse Fourier transform is performed along frequency to generate the range information of the target image. The result is a two-dimensional image in range and azimuth.

6.4 COMPRESSED SENSING IMAGING RESULTS

The imaging method is demonstrated using simulated and measured backscattering data collected through a pipe. For each set of data the image is formed using CS and compared to an image formed using a matched filter. In the latter case, the DOA estimation, step 3 of our method, is replaced with a matched filter. To solve the linear program in (6.8) requires a solver. Many solvers capable of solving (6.8) are available including the l1Magic toolbox [79], CVX [80], and SPGL1 [81]. Some of the solvers, such as l1Magic operate on real data, therefore it is necessary to pose the linear problem in (6.7) in terms of its real and imaginary components via the following linear equation:

$$\begin{pmatrix}\mathrm{Re}\{y\}\\ \mathrm{Im}\{y\}\end{pmatrix} = \begin{bmatrix}\mathrm{Re}\{A\} & -\mathrm{Im}\{A\}\\ \mathrm{Im}\{A\} & \mathrm{Re}\{A\}\end{bmatrix}\begin{pmatrix}\mathrm{Re}\{x\}\\ \mathrm{Im}\{x\}\end{pmatrix} + \begin{pmatrix}\mathrm{Re}\{v\}\\ \mathrm{Im}\{v\}\end{pmatrix}. \tag{6.9}$$

For the remainder of this chapter, the SPGL1 Matlab toolbox is used. It was found that the solvers that operate on real data were more likely to produce phase errors due to quantization, which causes high sidelobes and false targets in range. Therefore, SPGL1 was chosen because it operates on complex data natively resulting in less phase error. The pipe used for simulation and measurement has a radius of 2.55 cm and a length of 76.5 cm and data are collected for 12-18 GHz. The backscattering data are observed at 9

positions, equally spaced in azimuth from -40° to 40° and 45 cm from the mouth of the pipe. To test the imaging method, monostatic backscattering data are simulated for a single point target at $\bar{r}(2.5\text{m}, 0°)$ using the modal approach. The basis, *A*, is also computed using the modal approach with 69 points from -85° to 85° in azimuth. For the linear program in (6.8), ϵ is set to $0.01\|y\|_2$. Figs. 6.2(a) and 6.2(b) show the results of the DOA estimation at all frequencies for a CS and matched filter respectively. Both provide valid azimuth estimations, however it is clear that CS gives better localization. Figs. 6.2(c) and 6.2(d) show the results after applying the inverse Fourier transform after CS and matched filter DOA estimations respectively. The final point scatterer response shows that CS gives better performance in terms of localization and sidelobe response. More importantly, despite the fact that it is not known whether our basis, *A*, satisfies the RIP, the results in Fig. 6.2 indicate that L1-minimization can be used to obtain a high-resolution image through a pipe.

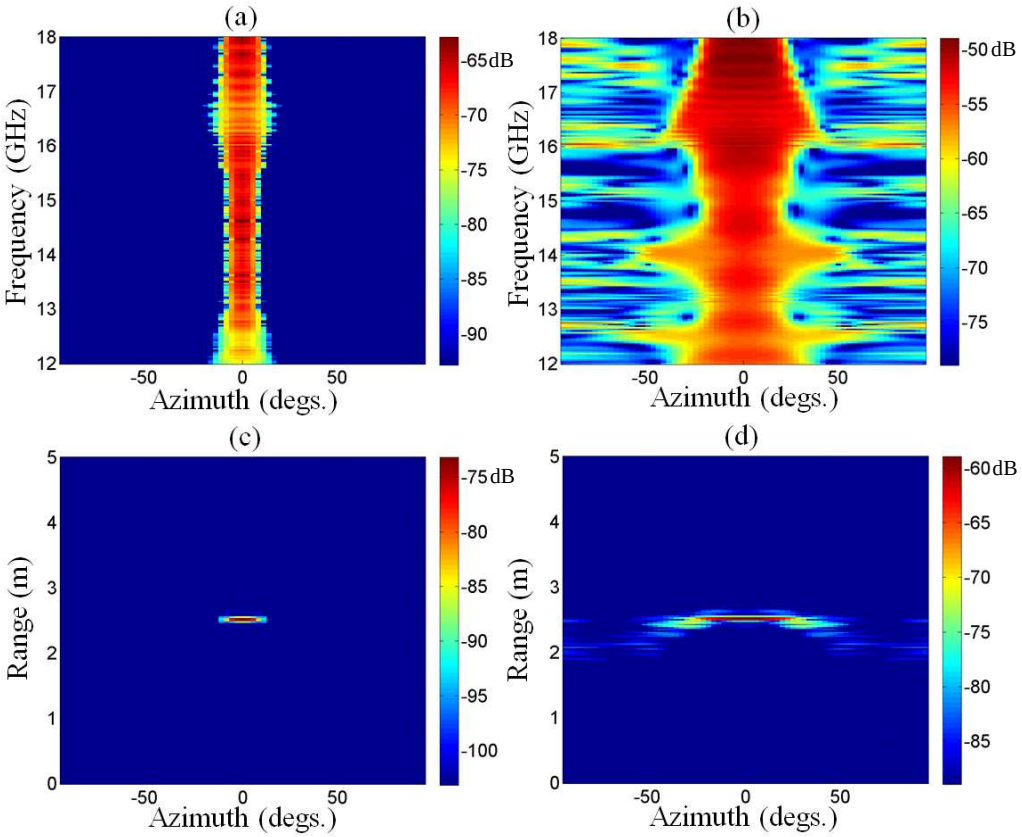

Figure 6.2: Simulated backscattering data with DOA estimation and image using (a) & (c) CS and (b) & (d) a matched filter.

Next, measured monostatic backscattering data are collected through a pipe as described in Appendix A. The pipe and measurement parameters are the same as in simulation. A corner reflector with an edge length of 5 cm is placed at $\bar{r}(2.5\text{m}, 20°)$. The basis, *A*, is computed using the modal approach with the same parameters as before. For the linear program in (6.8), ϵ is set to $0.1\|y\|_2$ to account for the higher noise level in the measurement as compared with simulation, which was noiseless. Figs. 6.3(a) and 6.3(b) show the results of the DOA estimation at all frequencies from the CS and matched filter respectively. Figs. 6.3(c) and 6.3(d) show the CS and matched filter images respectively.

In Fig. 6.3(a) the localization deteriorates in two frequency bands around 14 GHz and then above 16 GHz. These frequencies are at the cutoff of additional propagating modes that get excited within the pipe. Since it is difficult to model the propagation exactly around cutoff the result is mismatched between the simulated basis and actual pipe channel. This causes the loss of localization in these frequency bands, however there is little effect on the final image in Fig. 6.3(c). The results in Fig. 6.3 confirm that the CS imaging procedure is applicable to measured data and again illustrates the superior localization over matched filter processing. In addition this also shows that the measurement data can be processed using CS with a simulated basis.

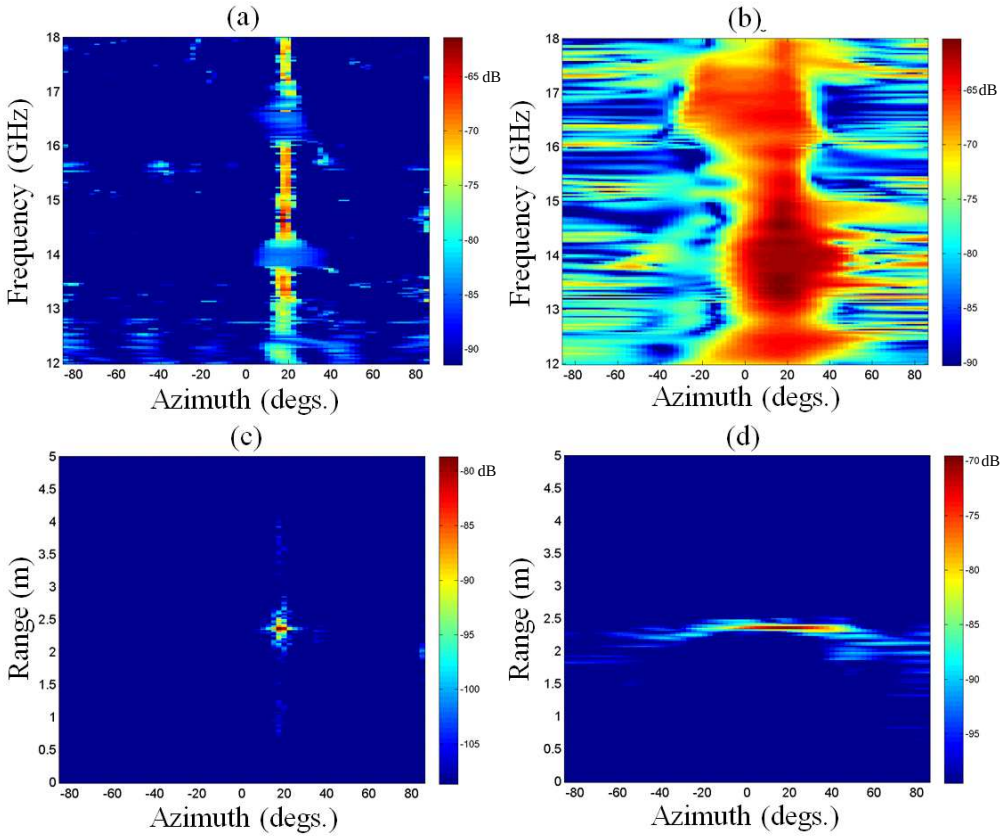

Figure 6.3: Single target measured backscattering data with DOA estimation and image using (a) & (c) CS and (b) & (d) a matched filter.

Finally, measurements are made with two targets to demonstrate the resolution performance of CS. Two corner reflectors of equal size are placed 2.5 m down-range at 15° and -15° in azimuth. Figs. 6.4(a) and 6.4(b) show the results of the DOA estimation using CS and matched filter processing. From the results it is clear that matched filter processing cannot resolve the two targets while CS successfully detects the presence of two targets. This is further confirmed in Figs. 6.4(c) and 6.4(d), where the CS image shows two targets at their expected locations and the matched filter shows only one

target. These results also demonstrate that CS can distinguish between correlated radar targets, unlike MUSIC.

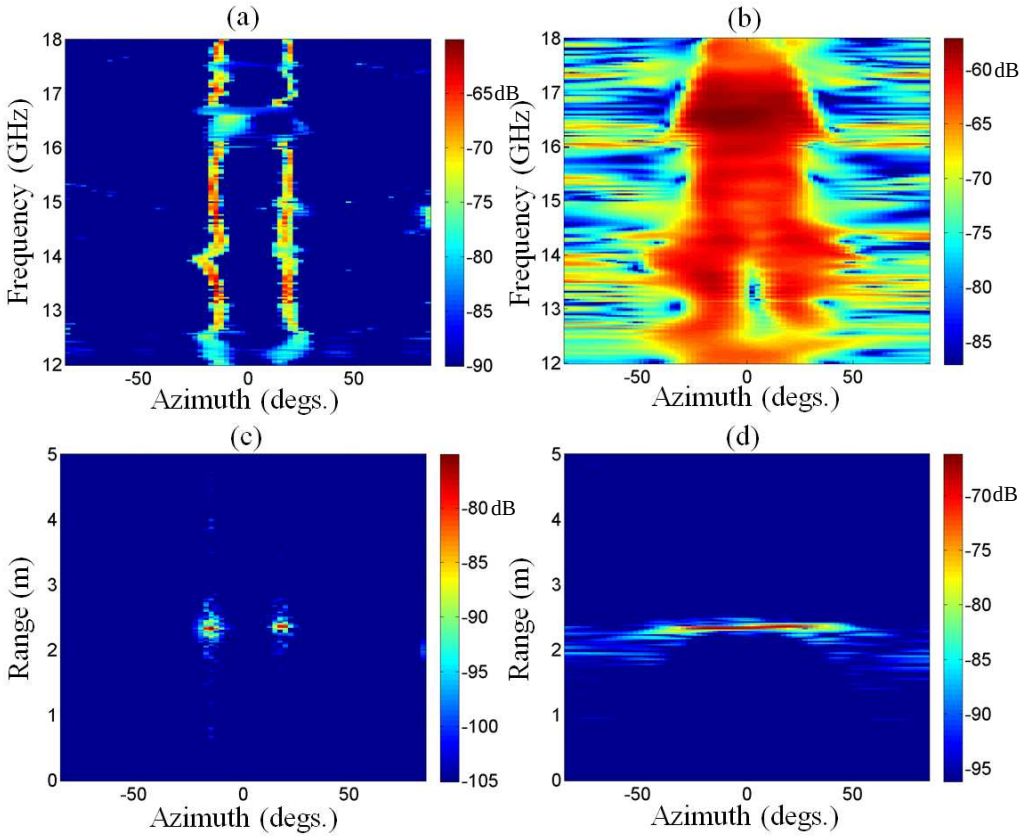

Figure 6.4: Two target measured backscattering data with DOA estimation and image using (a) & (c) CS and (b) & (d) a matched filter.

6.5 UNCERTAINTY EFFECTS ON COMPRESSED SENSING

Similar to the study of uncertainty effects of MUSIC in the previous chapter, the effects of uncertainty on the performance of CS are explored through simulation. The effects of additive noise on DOA estimation are investigated. To model additive noise, white Gaussian noise is added to the simulated backscattering data. First, the noise performance of CS with respect to pipe radius is simulated. The simulation consists of a

single target with three different positions of 0°, 45°, and 60° in azimuth and 1m from the right end of the pipe in each case. The array for each simulation contains 9 elements equally spaced in azimuth from -40° to 40° and 45cm from the left pipe opening. Pipes with a length of 50cm and with radii of 2.5cm, 5cm, and 10cm are simulated. A Monte Carlo simulation is run with 1000 simulations for each noise power level ranging from -80 to 0 dB normalized to the transmit power of each array element. The power of each array element is set to unity. For the linear program in (6.8), ϵ is set to $0.1\|y\|_2$. The DOA estimation error is measured for each run and averaged over all the runs for each noise power level. The results of the Monte Carlo simulations are shown in Fig. 6.5. Figs. 6.5(a), 6.5(b), and 6.5(c) are for a target at 0°, 45°, and 60° respectively. In addition to the DOA estimation error for CS, the DOA estimation error of a random guess is also simulated and shown as a dashed line in the figures. Several observations can be made from Fig. 6.5. First, a target closer to 0° is easier to detect in the presence of noise and becomes increasingly more difficult to detect as the target moves off boresight. Second, a larger pipe improves the detection performance in the presence of noise. These same trends were observed in the previous chapter when using MUSIC. Also, it is important to point out that while the CS performance degradation may appear to be worse than that of MUSIC when comparing Fig. 6.5 to Fig. 5.9, the CS results were generated based on monostatic data while the MUSIC results were based the larger bistatic data set.

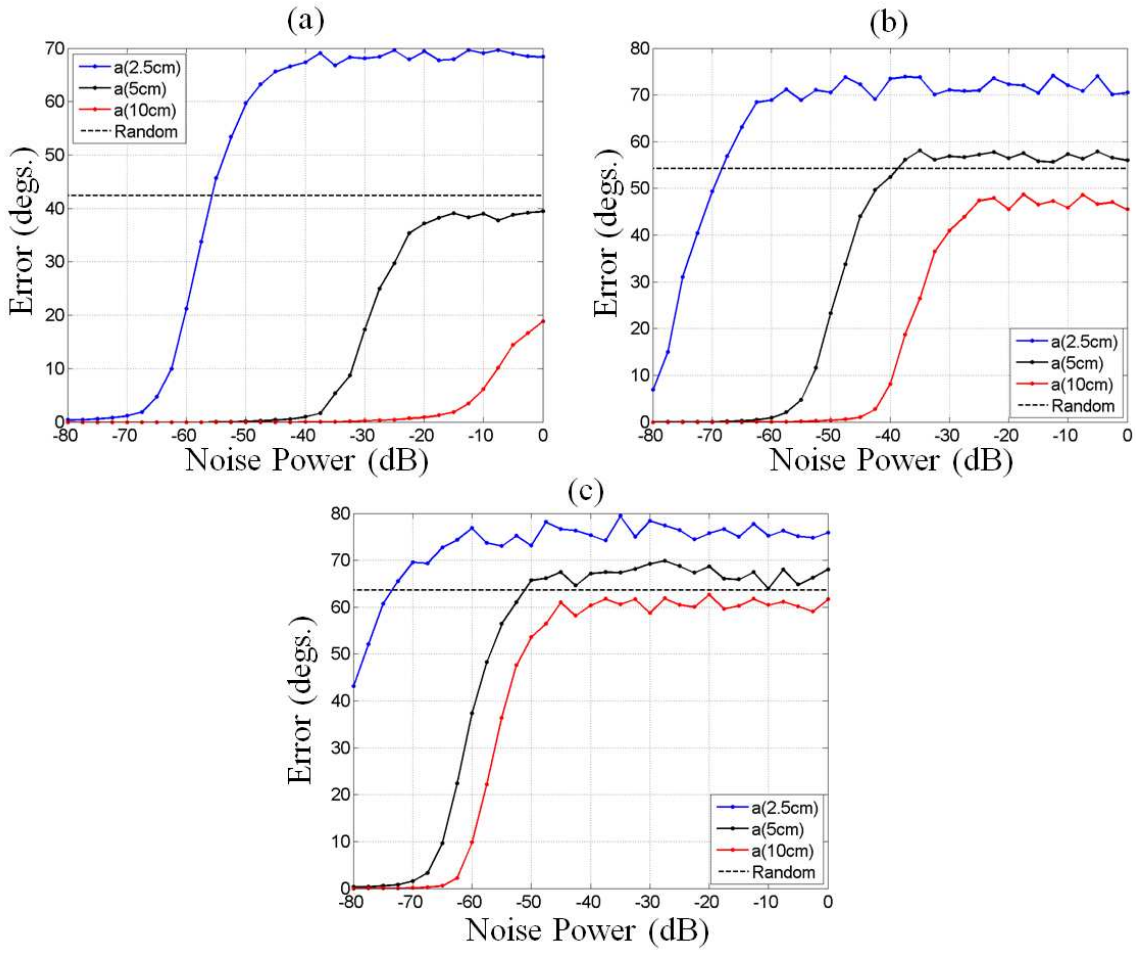

Figure 6.5: CS DOA estimation error in the presence of noise with respect to pipe radius for a target located at (a) 0°, (b) 45°, and (c) 60° in azimuth.

Next, the effect of array sampling on the noise performance of CS is simulated. The Monte Carlo simulation is performed the same as before. However, the pipe radius is set to 5cm with a length of 50cm and the extent of the array in azimuth is set from -40° to 40° while the number of elements in the array was varied. The array elements are equally spaced in azimuth and the number of array elements is set to 9, 17, and 33. The Monte Carlo simulation results are shown in Figs. 6.6(a), 6.6(b), and 6.6(c) for a target at 0°,

45°, and 60° in azimuth respectively. Again it is observed that the detection of targets as they move away from boresight is increasingly more difficult in the presence of noise. However, contrary to intuition it is observed that increasing the number of elements slightly hurts DOA estimation performance. This is most likely due to the choice of ϵ. As the number of elements is increased it becomes more difficult to match the data for the same ϵ.

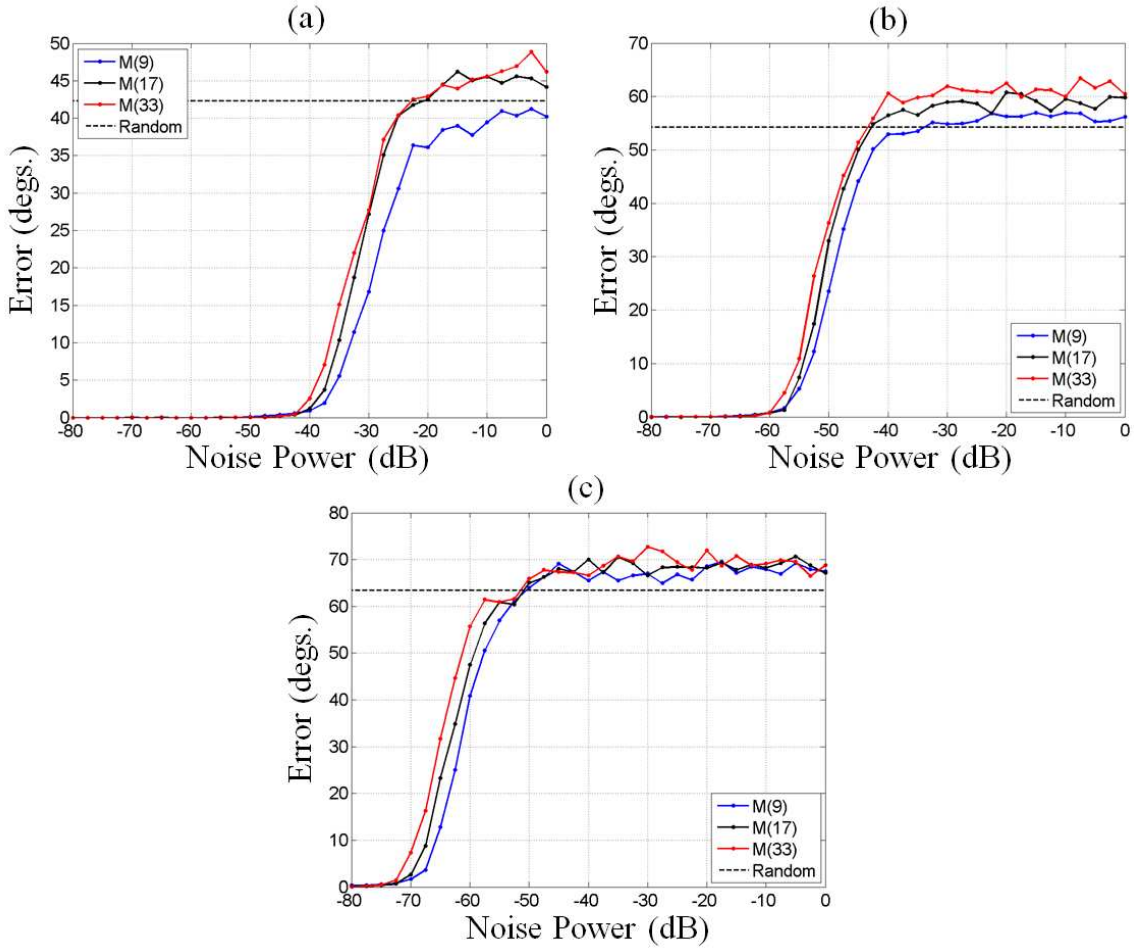

Figure 6.6: CS DOA estimation error in the presence of noise with respect to array sampling for a target located at (a) 0°, (b) 45°, and (c) 60° in azimuth.

The third and final Monte Carlo simulation is to determine the effect of the array extent on noise performance. Here, the number of elements in the array is set to 17 and the elements are equally spaced in azimuth from -20°:20°, -40°:40°, and -70°:70°. The pipe radius is remains 5cm and the length is 50cm. Figs. 6.7(a), 6.7(b), and 6.7(c) show the simulation results for a target at 0°, 45°, and 60° in azimuth respectively. The results show, that in general, increasing the extent of the array improves the performance of CS in the presence of noise.

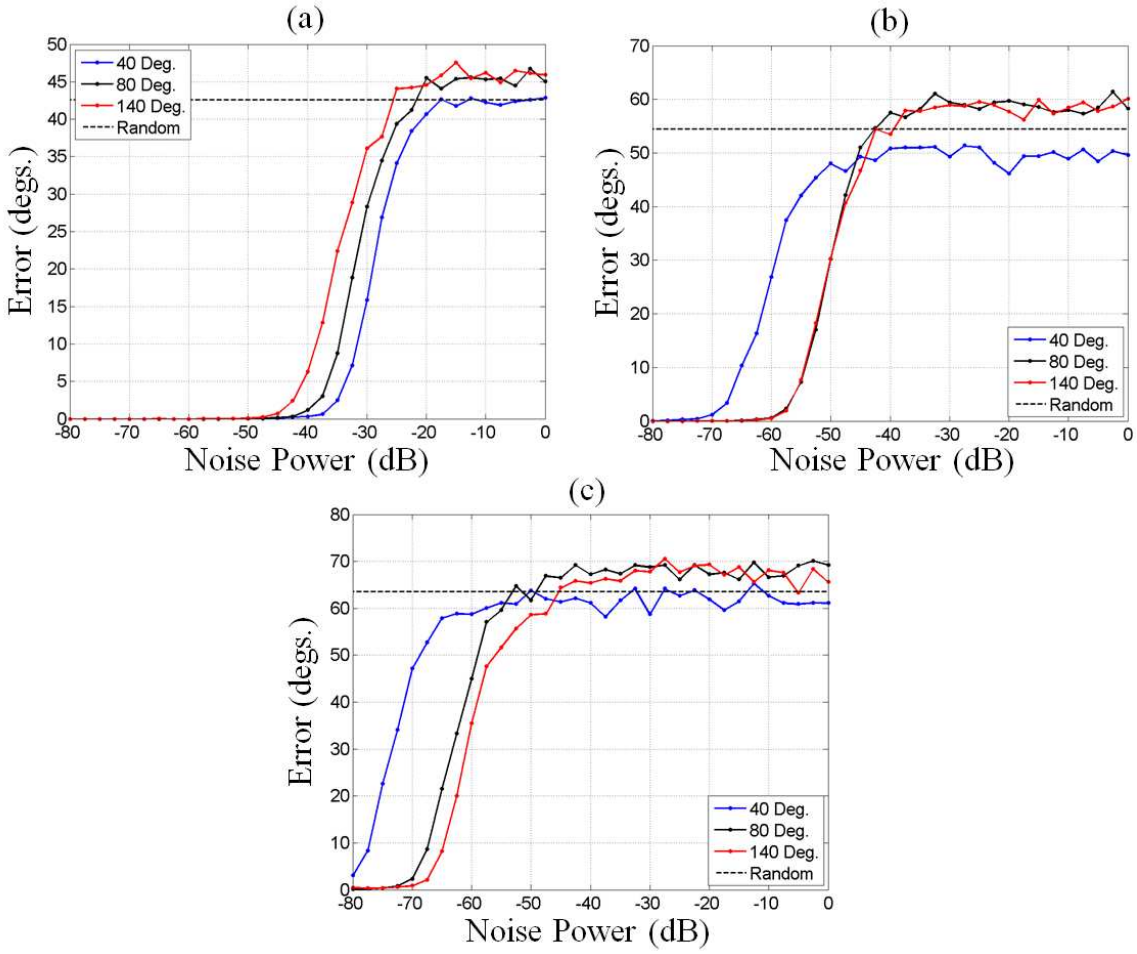

Figure 6.7: CS DOA estimation error in the presence of noise with respect to array extent for a target located at (a) 0°, (b) 45°, and (c) 60° in azimuth.

6.6 CONCLUSIONS

In this chapter a technique for obtaining radar images through a pipe based on compressed sensing has been developed and demonstrated. By assuming the image is sparse in azimuth it is possible to apply CS theory to obtain a high-resolution DOA estimation. To apply CS, an L1-minimization was solved using the SPGL1 solver to obtain the DOA for the target. While it is not possible to ascertain whether the pipe channel satisfies the restricted isometry property, it was shown that an L1-minization can still be applied to obtain high-resolution images through a pipe. The imaging method was demonstrated through simulation and measurement and it was shown that measurement data can be processed using a basis simulated using the modal approach. Since a robust sampling criteria does not exist for the pipe, it is not clear whether any compression or reduction in the number of data samples was achieved. Nonetheless, the resolution achieved with CS is certainly better than the resolution achieved using matched filter processing. In addition, contrary to MUSIC, CS operates on monostatic data, which is easier to collect in practice using synthetic aperture data collection. Finally, the performance with respect to noise was investigated. It was found that increasing the radius of the pipe and angular extent of the array improves performance and, contrary to intuition, increasing the sampling slightly hurts performance.

Chapter 7: Propagation Through an Arbitrary Pipe Channel

7.1 INTRODUCTION

Up to this point in the dissertation it has been assumed that the pipe channel consists of a straight pipe. Propagation through straight sections of circular waveguides is well understood. It is simply a phase delay of each mode down the length of the section based on the corresponding propagation constant. In this chapter, we extend our propagation analysis to deal with more complex pipe structures that include discontinuities such as bends and junctions. The presence of discontinuities in the pipe complicates the transmission, especially in an over-moded pipe. In a straight pipe, due to the orthogonality of waveguide modes there is no cross coupling between modes. However, it is known that mode conversion takes place, i.e. there is cross coupling between modes, when propagating through waveguide discontinuities [46][27]. The implication is that unlike a straight section of waveguide, the strength of the modes on the output aperture will not necessarily be equal to the strength of modes on the input aperture, which complicates the computation of the transmission through the pipe. Many numerical methods exist that are capable of computing the transmission of a field through a pipe. In order to continue using the closed-form solution for radiation and coupling from a circular waveguide, it is necessary to compute the transmitted field in terms of the modal components. Therefore, a generalized scattering matrix (GSM) approach to transmission through a pipe channel will be used [46][82][83].

In this chapter an approach for computing the transmission through an arbitrary pipe channel using the GSM is proposed. The remainder of this chapter is divided into four sections. In Section 7.2 a review of the generalized scattering matrix will be given followed by a description of how the GSM is used to compute transmission through a pipe. In Section 7.3, the computation of the GSM for a 90° bend using the commercial software package FEKO [46] is discussed. Section 7.4 presents simulation and measurement results for transmission through a pipe with a 90 degree bend. The final section discusses conclusions.

7.2 GSM METHOD FOR TRANSMISSION THROUGH COMPLEX PIPE STRUCTURES

The scattering matrix is a useful tool in microwave network analysis to characterize two-port networks that relates the incident waves propagating into the network to the reflected/transmitted waves propagating out of the network. This provides a complete electromagnetic description of the network. In the simplified definition for scattering parameters there is a single mode on each port. The generalized scattering parameters extends the scattering matrix definition to handle multiple modes [46]. Therefore, a section of waveguide can be described by a multi-port generalized scattering matrix [82]. Each propagating and evanescent mode is allocated an entry in the GSM, which results in a matrix of infinite dimensions. Therefore, a single reflection or transmission coefficient is replaced by an infinite sub-matrix in this construct. In theory, such an infinite-size matrix can fully describe a waveguide discontinuity in an over-moded waveguide. For practical implementations, only a finite number of evanescent

modes are needed since higher order modes decay rapidly away from the discontinuity. The GSM for a section of waveguide describes the modes propagating away from a waveguide segment from the set of incident modes. This makes the GSM approach useful for interfacing with the closed-form modal approach.

For an interconnected waveguide network consisting of straight sections and discontinuities like bends and other junctions the individual GSMs associated with each section can be cascaded to form a total GSM description of the waveguide network [82]. This is a useful property of the GSM. To cascade two GSMs, consider the two networks shown in Fig. 7.1. The two networks in Fig. 7.1 are described by the following GSMs:

$$\begin{pmatrix} R^{(A)} \\ R^{(B)} \end{pmatrix} = \begin{bmatrix} S_{11} & S_{12} \\ S_{21} & S_{22} \end{bmatrix} \begin{pmatrix} I^{(A)} \\ I^{(B)} \end{pmatrix} \tag{7.1}$$

$$\begin{pmatrix} R^{(C)} \\ R^{(D)} \end{pmatrix} = \begin{bmatrix} S_{33} & S_{34} \\ S_{43} & S_{44} \end{bmatrix} \begin{pmatrix} I^{(C)} \\ I^{(D)} \end{pmatrix} \tag{7.2}$$

where $I^{(\cdot)}$ represents incident field strengths, $R^{(\cdot)}$ represents reflected field strengths, and S_{mn} are the scattering parameter sub-matrices. The two networks in Fig. 7.1 are connected via port B and C to form a GSM description of the cascaded network. The cascaded GSM has the form:

$$\begin{pmatrix} R^{(A)} \\ R^{(D)} \end{pmatrix} = \begin{bmatrix} S_{AA} & S_{AD} \\ S_{DA} & S_{DD} \end{bmatrix} \begin{pmatrix} I^{(A)} \\ I^{(D)} \end{pmatrix}. \tag{7.3}$$

The parameters in (7.3) are found using the following four equations:

$$S_{AA} = S_{11} + S_{12}(I - S_{33}S_{22})^{-1}S_{33}S_{21} \tag{7.4}$$

$$S_{AD} = S_{12}(I - S_{33}S_{22})^{-1}S_{34} \tag{7.5}$$

$$S_{DA} = S_{43}(I - S_{22}S_{33})^{-1}S_{21} \tag{7.6}$$

$$S_{AA} = S_{44} + S_{43}(I - S_{22}S_{33})^{-1}S_{22}S_{34}. \tag{7.7}$$

The ability to cascade GSMs is a useful property because it makes it possible to decompose a complex network into a set of simple or primitive elements. In the case of a complex pipe channel, the pipe can be decomposed into a set of simple primitives such as straight sections, bends, and junctions. Each of the primitives can then be characterized by their GSM. Transmission through the channel is then computed by cascading the primitive elements together. The advantages to this approach are two-fold. First, by reducing the problem into small sections the computations are more practical than solving the full pipe channel. Second, once the GSM for the primitive elements have been computed they can be used to model complex pipe channels comprised of these primitives.

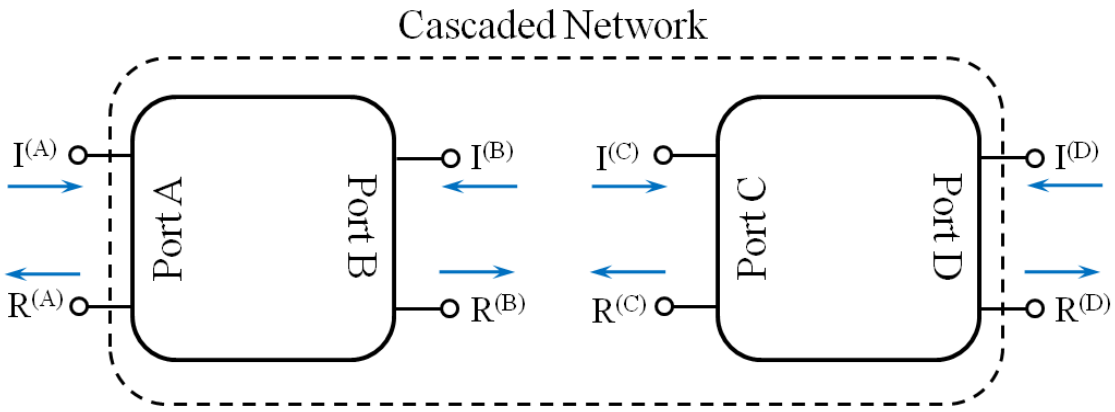

Figure 7.1: Two microwave networks.

As mentioned above, the GSM for a waveguide includes both propagating and evanescent modes. The modal approach for coupling and radiation from the waveguide only considers the propagating modes, therefore ideally the GSM would only consider the propagating modes as well. However, when propagating through a discontinuity it is known that energy from the propagating modes will couple into the evanescent modes and vice-versa [27]. Therefore, using only the propagating modes in the GSM will give inaccurate results. If we assume that all discontinuities are separated by a straight section of waveguide of sufficient length to allow the evanescent modes to decay then it is possible to only consider the propagating modes of the GSM. This assumption will be adopted here and only the propagating modes will be considered in the GSM computations.

The approach to compute the transmission through an arbitrary pipe channel is summarized as follows. First, the complex channel is divided into primitive elements and

each primitive element is characterized by its GSM. Second, the complete GSM description of the pipe channel is formed by cascading the GSMs together. Third, the strength of the modes excited by the incident field are found using the closed-form solution and the results are used with the GSM cascade to compute the transmission of the modes through the pipe channel. The final step is to solve the radiation problem for the given mode strengths.

7.3 GSM RESULTS FOR PIPE SEGMENTS

To compute the GSM for a pipe discontinuity structure requires a full-wave simulation. To perform this simulation, FEKO's method of moments solver is chosen. FEKO allows the user to define waveguide ports and impress TE and TM circular-waveguide field distributions as incident fields. The computation of the GSM using FEKO is demonstrated through an example. The GSM for a 90° bend in a circular pipe is sought. The geometry of the bend is shown in Fig. 7.2(a). The radius of the pipe is a and the radius of the bend is r. The bend is modeled in FEKO and the CAD model is shown in Fig. 7.2(b).

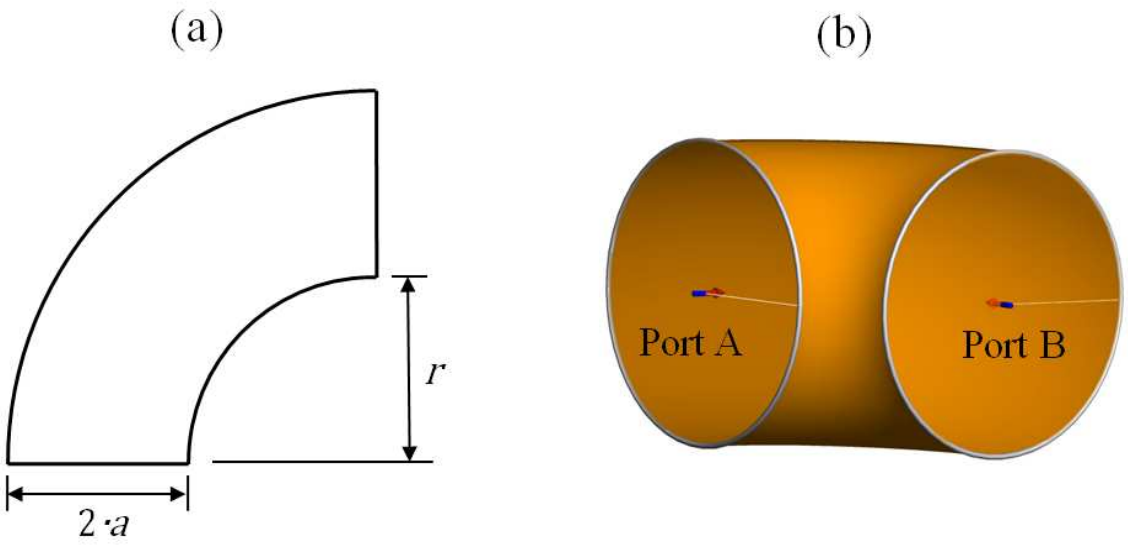

Figure 7.2: Bend (a) geometry (b) FEKO CAD model.

Unfortunately, FEKO does not natively compute the GSM for a given waveguide section, therefore it is necessary to derive the GSM from near-field simulations. The procedure for computing the GSM for the S_{21} sub-matrix using FEKO is summarized in three steps. 1) For each propagating mode the incident mode is excited on Port A of Fig. 7.2(b) and the electric and magnetic fields on Port B are observed. 2) The strengths of the propagating modes on Port B are then found by projecting each mode into the near field results using [46]:

$$a_{ij} = \frac{1}{2Q_j}\left[\iint \bar{E}_t^{Feko} \times \bar{H}_t^j \cdot d\bar{s} + \iint \bar{E}_t^j \times \bar{H}_t^{Feko} \cdot d\bar{s}\right] \tag{7.8}$$

where a_{ij} is the strength of the jth mode on Port B excited by the ith mode on Port A, $\bar{E}_t^{Feko}$ and $\bar{H}_t^{Feko}$ are the transverse electric and magnetic fields from FEKO, $\bar{E}_t^j$ and $\bar{H}_t^j$

are the transverse electric and magnetic fields for the jth propagating mode, and Q_j is defined as follows:

$$Q_j \triangleq \iint \bar{E}_t^j \times \bar{H}_t^j \cdot d\bar{s}. \tag{7.9}$$

3) Once the strength of each mode is determined, the S-parameters are computed by normalizing to unit power using

$$S_{ij} = \frac{a_{ij}}{\iint \bar{E}_t^i \times \bar{H}_t^i \cdot d\bar{s}} \tag{7.10}$$

where S_{ij} is the scattering parameter and $\bar{E}_t^i$ and $\bar{H}_t^i$ are the transverse electric and magnetic fields for the ith mode impressed on Port A. A similar method is used to find the S_{11} and S_{22} sub-matrices, but the near fields are observed on the same port as the excitation instead of the opposite port. The final sub-matrix S_{12} is already known since S_{12} is equal to S_{21} through reciprocity.

To test the method for computing the GSM using FEKO, a straight section is simulated and compared with theory. The straight section of waveguide has a radius of 2.54cm and length of 3cm. The waveguide is lossless and the GSM is calculated using the method outlined above for a frequency of 6 GHz. The magnitude of the GSM in decibels is shown in Fig. 7.3. There are a total of 5 propagating modes present in the pipe, with TE_{11} and TE_{21} each having a vertically and horizontally polarized mode. For a straight section of waveguide it is expected that the S_{12} and S_{21} sub-matrices are diagonal with ones on the diagonal, which is the case in Fig. 7.3. To further verify the GSM result

for the straight section of waveguide the phase of the S_{21} sub-matrix if compared to the phase expected from theory. The theory results are found by computing the phase delay using the propagation constant for each mode. The phase of the FEKO and theory results are shown in Fig. 7.4. From Fig. 7.4 it is clear that FEKO and theory are in agreement. The results for the straight section verify that the method for computing the GSM using FEKO is valid.

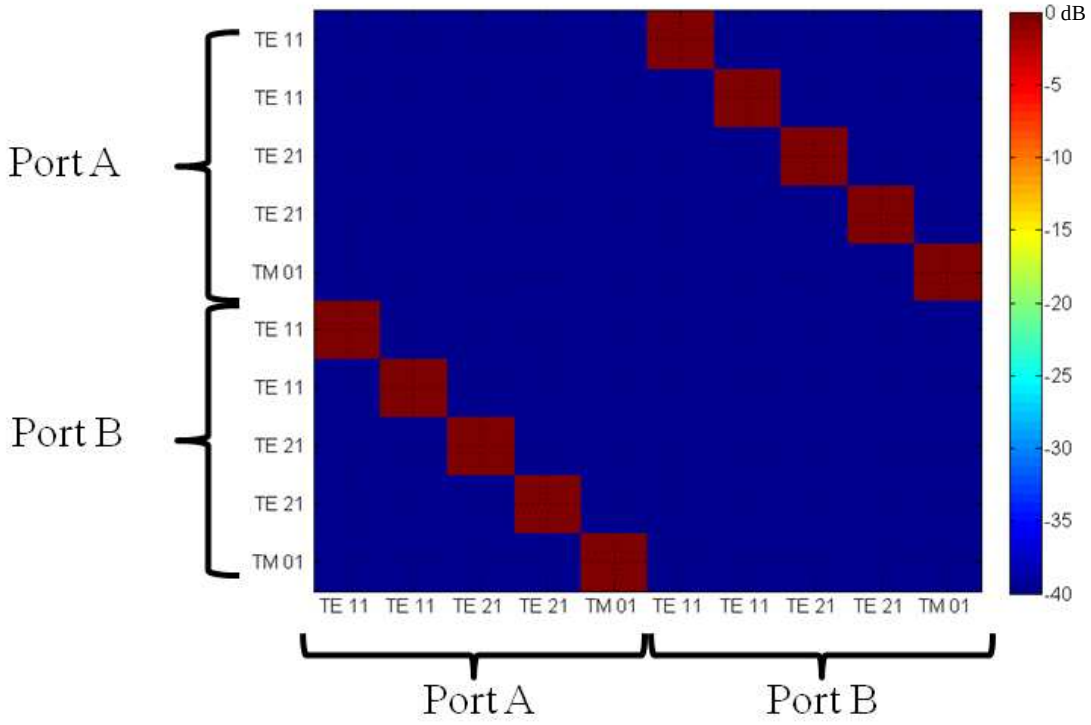

Figure 7.3: Magnitude of GSM for straight section of circular waveguide.

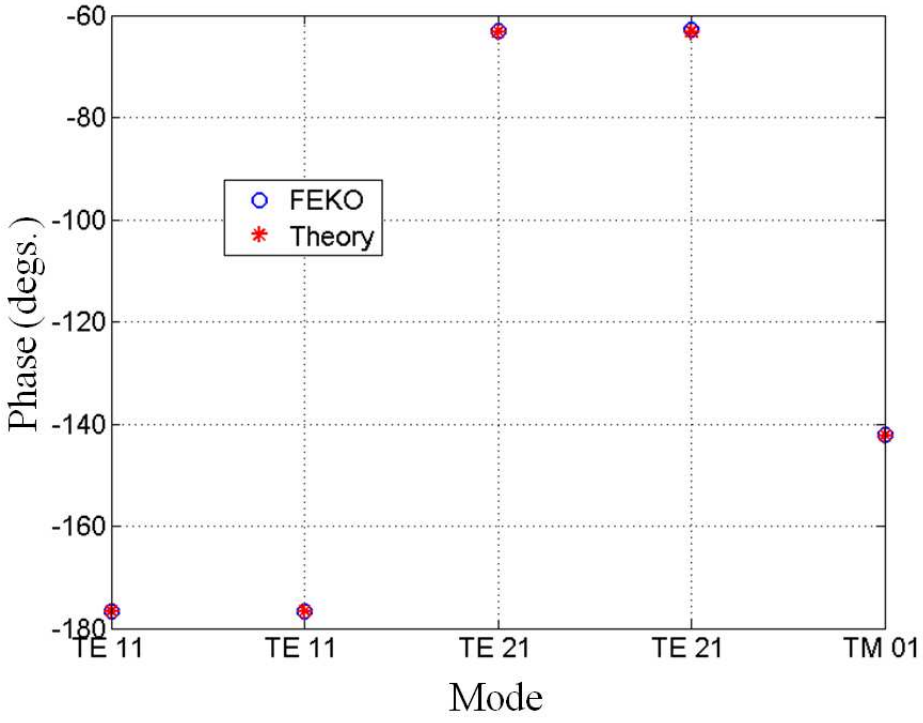

Figure 7.4: Phase for S_{21} sub-matrix of GSM for a straight circular waveguide section.

Now, the GSM for the bend in Fig. 7.2(b) is computed for a pipe radius of 2.54cm and bend radius 1.5cm at 6 GHz. The fields are simulated in FEKO and the GSM is computed using the approach above. The magnitude of the GSM entries are shown in Fig. 7.5. As in the straight section of Fig. 7.3, there are a total of 5 propagating modes present in the pipe. From the results in Fig. 7.5 it is clear that mode conversion takes place through the pipe. For example, when the vertically polarized TE_{11} mode is incident on Port A (first column of the GSM), the vertically polarized TE_{11} and TE_{21} modes are transmitted to Port B. In addition, it is seen that the reflection sub-matrices, S_{11} and S_{22}, have small entries, indicating that most of the energy is transmitted through the bend.

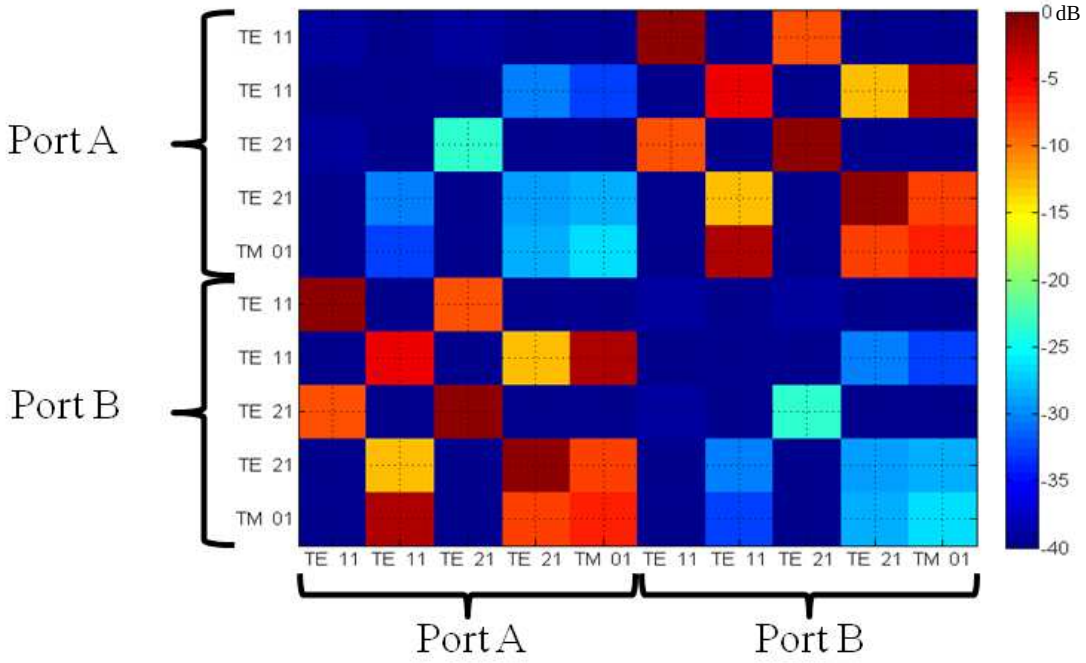

Figure 7.5: Magnitude of the GSM for a 90° bend.

7.4 TRANSMISSION RESULTS THROUGH A PIPE BEND

The method described above for computing the transmission through a pipe is tested on a pipe channel that consists of a 90° bend. The pipe to be measured is shown in Fig. 7.6. The pipe has a radius of 2.4cm. To apply the GSM method to compute the transmission, the pipe is divided into three segments, two straight sections 10.2 cm in length and a 90° bend with a bend radius of 5.08 cm. The segmentation of the pipe is shown in Fig. 7.7.

Figure 7.6: Pipe with 90° bend.

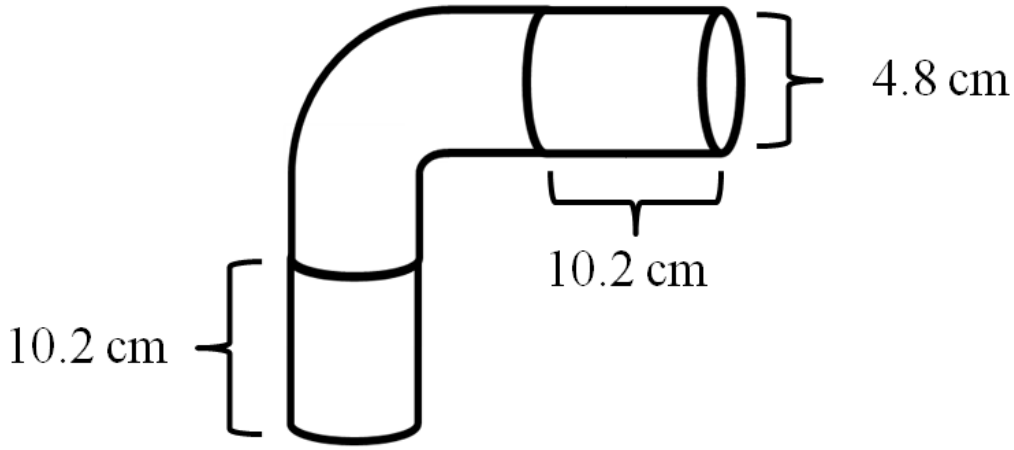

Figure 7.7: Segmentation of pipe channel.

Transmission through the pipe in Fig. 7.7 is simulated using the GSM approach. The GSM for the bend is computed using FEKO and the GSMs for the straight sections are computed from theory. The GSMs for each section are cascaded together using (7.4)-(7.7) to find the complete GSM description of the pipe. The complete GSM description is

used with the closed-form solutions for coupling into and radiation from the pipe to find the transmission through the pipe. First, the pipe is simulated from 3 to 12 GHz, the transmitter is placed at boresight or 0° in azimuth, and the receiver is swept from -62° to 62° in azimuth. Measurements are then made using the same parameters as simulation. The simulation and measurement results are shown in Figs. 7.8(a) and 7.8(b), respectively. From the results in Fig. 7.8 the simulation is seen to agree fairly well with the measurement. In particular, below 3.65 GHz no transmission is seen in both simulation and measurement because the pipe is below cutoff. Above cutoff the pipe begins to transmit. At 10.6 GHz in the simulation data, the TE_{12} mode is excited and results in the distinct interference pattern seen. In the measurement result, this frequency is shifted up slightly to around 11GHz. The effects of the bend are very apparent in Fig. 7.8. For a straight pipe and a transmitter at boresight, the radiation pattern would be symmetric about 0° azimuth. However, from Fig. 7.8 it is clear that the pattern is not symmetric when the bend is present.

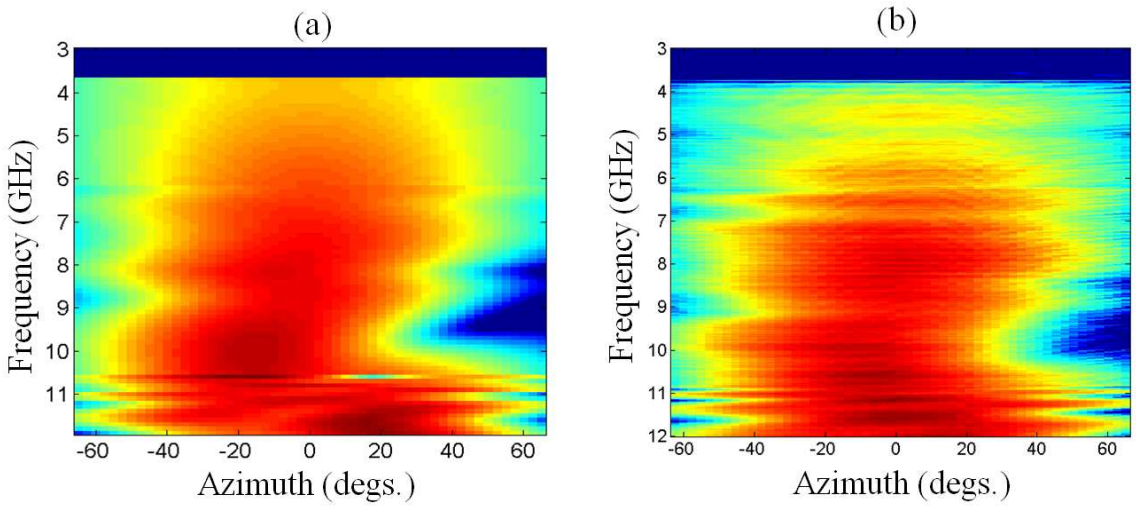

Figure 7.8: Radiation pattern through a pipe channel with 90° bend (a) simulated and (b) measured for transmitter at 0° in azimuth.

Next, simulation and measurement are performed using the same pipe, but the data are measured from 6 to 11 GHz and the transmitter is placed at 25° in azimuth. The simulation and measurement results are shown in Figs. 7.9(a) and 7.9(b), respectively. The radiation patterns in simulation and measurement show fairly similar patterns, although the detailed agreement is not perfect. This could be due to the difference between the CAD model used in the simulation and the actual pipe used in the measurement. Moreover, the strong interference above 10.5 GHz that is seen in simulation is not observed in the measurement plot. This feature is due to a mode near cutoff. This discrepancy can be attributed to the fact that in simulation the reflection of the mode from end of the pipe is ignored, while in the measurement the mode is strongly reflected near cutoff.

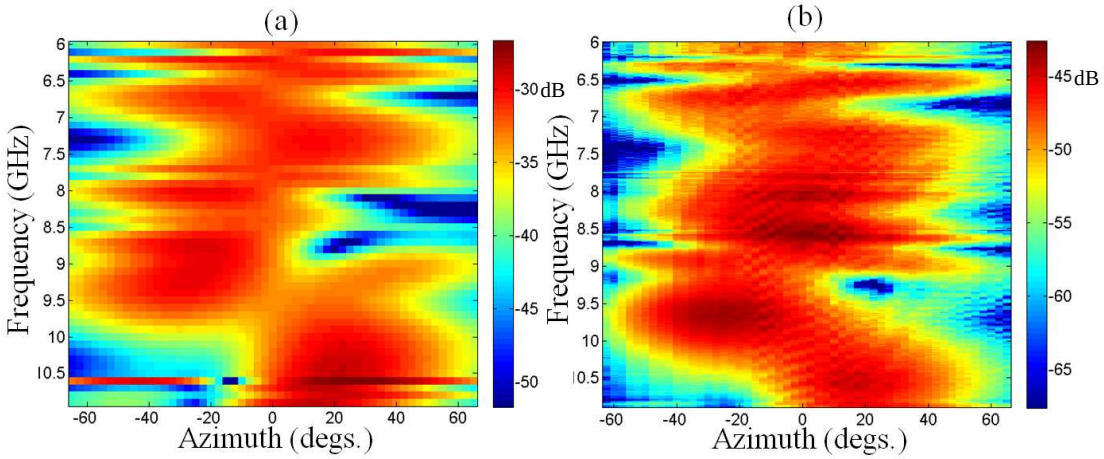

Figure 7.9: Transmission through a pipe channel with 90° bend (a) simulated and (b) measured for transmitter at 25° in azimuth.

7.5 CONCLUSIONS

In this chapter a method for characterizing the propagation through an arbitrary pipe channel was proposed. In order to continue to use the closed-form solutions for the coupling and radiation from a pipe, it was necessary to compute the transmission through the pipe in such a way that keeps track of the propagation of each mode. The GSM approach is well suited for this purpose. In addition, by segmenting a complex channel into primitive elements the GSM for the elements can be reused for modeling more complex channels. The computation of the GSM for a waveguide section using FEKO was discussed and demonstrated for a 90° bend. Then, the transmission through a bent pipe was simulated and shown to agree with measurement data at lower frequencies. At higher frequencies the agreement was not as strong; discrepancies were observed between simulation and measurement. Implementing this method at higher frequencies comes with two difficulties. First, as the frequency increases the computation time using

a full-wave analysis increases exponentially. Second, the modeling accuracy becomes more stringent, which is believed to be the source of mismatch between simulation and measurement. The methods and results in this chapter lay a framework for the study of propagation and imaging through complex pipe channels.

Chapter 8: Joint Time-Frequency Distribution Using Compressed Sensing

8.1 INTRODUCTION

In Chapter 2, the spectrogram, computed from the short-time Fourier transform (STFT), was used to analyze the transmission through a pipe and the backscattering from a target observed through a pipe. In general, joint time-frequency representations are a useful tool in the analysis of scattering mechanisms present in radar signature data from complex structures [43]-[45]. Two standard time-frequency distributions are the STFT and the Wigner-Ville distribution (WVD). The STFT is a linear time-frequency distribution based on a moving window Fourier transform in time or frequency. Therefore, there exists a tradeoff between frequency and time localization. The WVD is a quadratic distribution that provides excellent simultaneous time and frequency localization. However, for multicomponent signals the WVD exhibits cross terms. Reduced interference distributions based on the WVD, such as the Choi-Williams distribution [85], are well established. These distributions suppress cross terms at the expense of decreased localization. Recently, Flandrin and Borgnat [86] proposed a distribution that leverages advances in compressed sensing (CS) to suppress interference terms while maintaining the localization of the WVD. In this Chapter, applicability of Flandrin and Borgnat's distribution, henceforth denoted as the CSJTF, to radar signature analysis is explored. In Section 8.2, an overview of the CSJTF algorithm is presented. Then, in Section 8.3, the CSJTF distribution from simulated and measured radar

signatures of typical structures are compared to the STFT and the WVD. Section 8.4 gives conclusions.

8.2 CS-BASED TIME-FREQUENCY DISTRIBUTION

This section provides a brief description of Flandrin and Borgnat's distribution. The WVD for a signal is defined as:

$$W(t,\omega) = \frac{1}{2\pi}\int_{-\infty}^{+\infty} S^*\left(\omega + \frac{1}{2}\theta\right) S\left(\omega - \frac{1}{2}\theta\right) e^{-jt\theta} d\theta \tag{8.1}$$

where $W(t, \omega)$ is the WVD and $S(\omega)$ is the signal in the frequency domain. Alternatively the WVD can be found from the ambiguity function, $A(\theta, \tau)$:

$$\begin{aligned} A(\theta,\tau) &= \int_{-\infty}^{+\infty} S^*\left(\omega + \frac{1}{2}\theta\right) S\left(\omega - \frac{1}{2}\theta\right) e^{j\tau\omega} d\omega \\ &= \mathcal{F}^{-1}\{W(t,\omega)\}. \end{aligned} \tag{8.2}$$

As shown in (8.2), the WVD can be computed by taking the two-dimensional Fourier transform of the ambiguity function. It has been observed that for many common signals, the signal energy exists around the origin of the ambiguity plane and the cross-term energy exists away from the origin [86]. Reduced interference distributions take advantage of this property by weighting the domain around the origin of the ambiguity plane before taking the Fourier transform to suppress cross terms in the WVD [85]. Flandrin and Borgnat use the same concept; however, instead of taking a Fourier transform, they apply compressed sensing [63][64]. Their CSJTF method for computing a new distribution consists of three steps. First the ambiguity function of the signal is

computed using (8.2). Second, a subdomain, Ω, around the origin of the ambiguity plane is extracted. The subdomain, Ω, represents a fraction of the entire ambiguity domain. By taking a sufficiently small subdomain around the origin of the ambiguity plane, the signal energy is captured while the cross-term energy is not. The third and final step is to apply CS by solving the following linear program:

$$\min_{P} \|P\|_1 \text{ subject to } \|A_\Omega - \mathcal{F}^{-1}\{P\}\|_2 \leq \epsilon \tag{8.3}$$

where A_Ω is the subdomain, Ω, of the ambiguity function A, $\mathcal{F}^{-1}\{\cdot\}$ is the two-dimensional inverse Fourier transform, $\|\cdot\|_1$ is the 1-norm, $\|\cdot\|_2$ is the 2-norm, and P is the resulting CSJTF distribution. The effect is that the cross terms are suppressed while maintaining the localization of the original WVD. It should be noted that while many applications of CS deal with reconstructing a signal from sparse measurements, Flandrin and Borgnat aim to construct a new time-frequency distribution from limited samples of the ambiguity function. The CSJTF relies on two key elements to be successful: 1) the number of components in the distribution must be small, and 2) the signal energy and cross-term energy must be well separated in the ambiguity plane. For practical signals encountered in radar scattering, this may not always be the case and must be examined in more detail.

8.3 EXAMPLES USING CSJTF

The applicability of the CSJTF for radar signature analysis is tested using two examples, wideband scattering from an open-ended circular pipe and time-dependent

scattering from a rotating blade. In the first case, wideband backscattering from a metal circular pipe is examined. The pipe is 60 cm long with a radius of 1.8 cm and has one end open and the other end terminated with a short. Monostatic backscattering data are simulated using a modal approach for a frequency range of 2-18 GHz at boresight incidence. Fig. 8.1(a) shows the WVD, Fig. 8.1(b) shows the STFT, and Fig. 8.1(c) shows the CSJTF. To solve the linear program in (8.3), the L1-MAGIC TOOLBOX is used [79]. In Fig. 8.1 the early-time vertical line is scattering from the rim of the pipe at the open end. The two curved features are due to the dispersive modal propagation of energy inside the pipe. In the WVD, cross terms are clearly present and indicated in the figure. In the STFT, the cross terms are not present, however it is clear that the localization of the time-frequency components is inferior to that of the WVD. The CSJTF shows suppressed cross terms and localization comparable to the WVD.

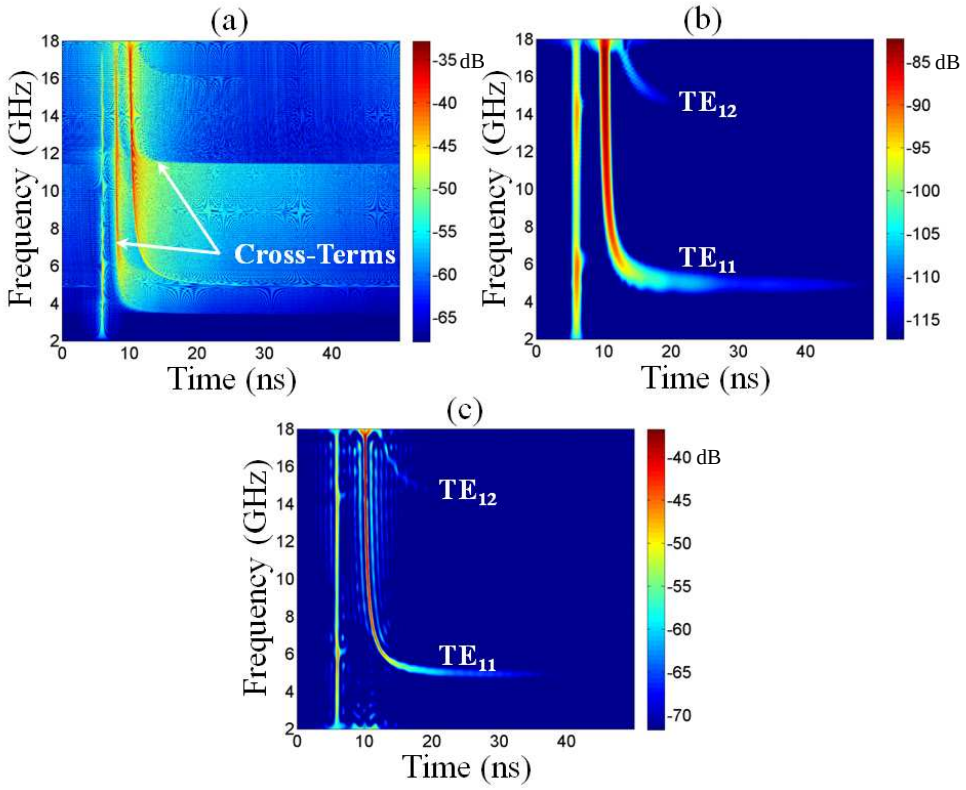

Figure 8.1: (a) WVD, (b) STFT, and (c) CSJTF for simulated backscattering from an open-ended pipe.

The results based on measured pipe data are shown in Fig. 8.2. The STFT is shown in Fig. 8.2(a) and the CSJTF is shown in Fig. 8.2(b). Again, for measurement data, the CSJTF shows suppressed cross terms and superior localization to the STFT.

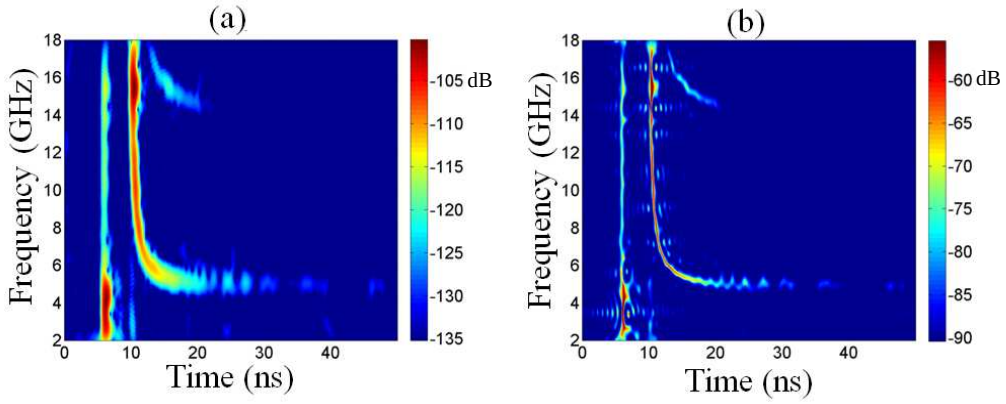

Figure 8.2: (a) STFT and (b) CSJTF for measured backscattering data from a pipe.

In the second example, time-dependent scattering from a rotating blade is examined. The time-dependent scattering from a single blade, 60 cm in length, rotating around one end is simulated one snapshot at a time at 14 GHz using the method of moments solver in FEKO. The resulting time-frequency distribution shows the time-varying Doppler behavior of the target. Fig. 8.3(a) shows the WVD, Fig. 8.3(b) shows the STFT, and Fig. 8.3(c) shows the CSJTF. The largest contribution to the Doppler scattering from the blade is known to be the blade-flashes [87]. For a single blade and one revolution, two blade-flashes are expected as indicated in Fig. 8.3(b). In the WVD, the blade-flashes are obscured by cross terms. In the CSJTF, the cross terms are suppressed, the blade-flashes are clearly observed, and the localization is improved compared with the STFT.

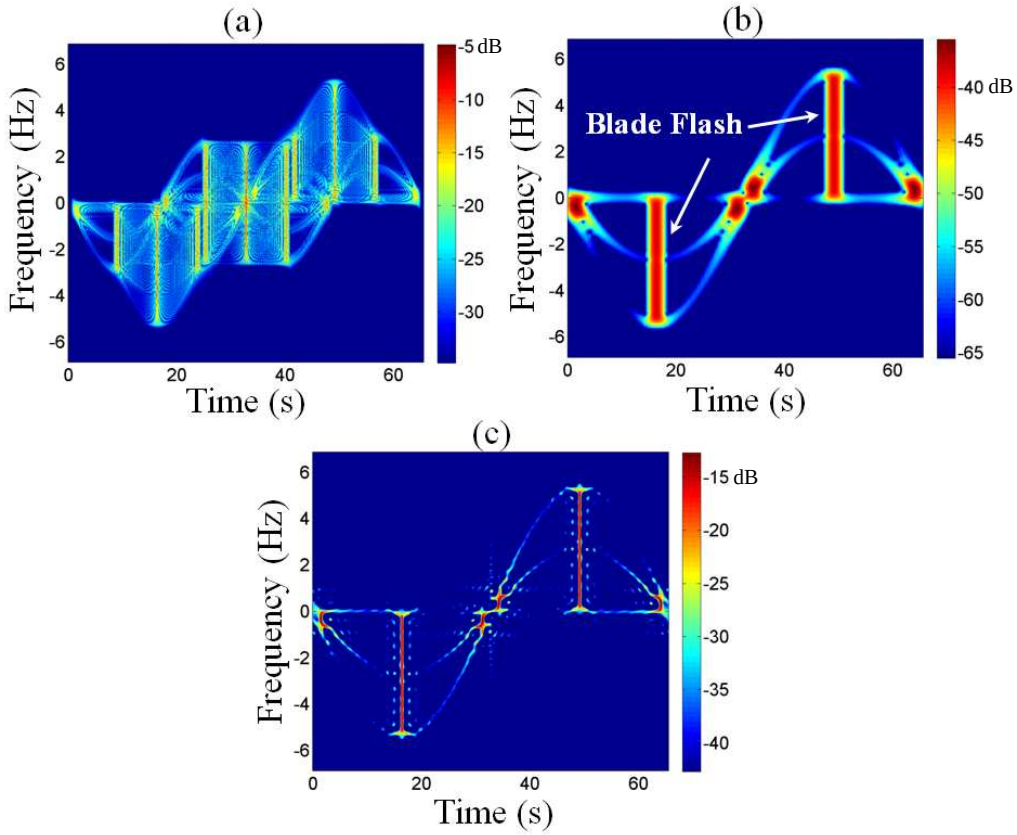

Figure 8.3: (a) WVD, (b) STFT, and (c) CSJTF for simulated Doppler scattering from a single rotating blade.

8.4 CONCLUSIONS

The CSJTF distribution provides the localization of the WVD without the troublesome cross terms. The method is based on the assumption that the signal and cross-term energies are well separated in the ambiguity plane. In this Chapter, it was shown that the CSJTF results in a useful time-frequency distribution for wideband scattering from a pipe and time-dependent scattering from a rotating blade. However, a careful choice of the ambiguity region was required to achieve good results. Other types

of radar signatures must also be examined to reach a more definitive assessment of the method.

Chapter 9: Conclusions and Future Work

In this dissertation, the ability to form radar images through a circular pipe was investigated. First, a mode-based method that was previously used for computing the RCS from a circular duct was adapted for modeling the transmission through a pipe in Chapter 2. The mode-based method is an approximation, but was verified through measurement to capture the essential physics of the pipe. The main advantage of the mode-based method is that it has a closed-form solution, therefore it is computationally fast. The mode-based method was then used to model two-way transmission through a pipe in order to simulate the backscattering from targets as seen through a pipe. The mode-based analysis of the pipe assumes the pipe is lossless and that there are no reflections from the ends of the pipe. The reflections and losses were seen to have limited effects on the transmission; nonetheless, methods for accounting for reflections and conductor losses were suggested. From the simulation and measurement data two key properties of the pipe channel were observed. First, a pipe channel acts as a high-pass channel, i.e. the transmission improves as the frequency increases. Second, the backscattering from a target can be seen through a pipe.

Extending from the observations in Chapter 2, the next four chapters dealt with forming radar images through a pipe. Four different algorithms that had been previously demonstrated for free-space imaging were applied to the problem of imaging through a pipe. The key difference between imaging in free space and imaging through a pipe is that the physics of the pipe must be properly accounted for in order to get a correctly focused image. In all the imaging methods, frequency diversity was used to obtain the

range to the target. The remaining challenge was to find the cross-range position of the target. To this end four different methods were explored.

Arguably the simplest method for determining cross-range position in free space is using delay-and-sum beamforming. In Chapter 3, a method based on similar principles was devised. Beams were found through a least squares solution and tested against bistatic scattering data to obtain a DOA estimate. This scheme requires the availability of bistatic scattering data, which make the data collection logistics more complex. In Chapter 4, a method using synthetic aperture radar (SAR) techniques was devised. In SAR, monostatic data are collected along a baseline and processed using a matched filter. In the case of the pipe, the matched filter was the complex conjugate of the pipe channel. It was also shown that matching pursuit could be applied to improve the localization of the final image when processing with a matched filter. In beamforming and matched filter processing it was found that the pipe size severely limited the cross-range resolution, therefore the remaining two chapters applied methods that offered superior resolution. In Chapter 5 the MUSIC algorithm was applied and shown to provide excellent resolution. However in order to apply MUSIC it was necessary to collect bistatic data in order to decorrelate multiple targets. In Chapter 6, compressed sensing (CS) was applied. CS was shown to provide good resolution and worked for either monostatic or bistatic scattering data.

From the four methods applied for imaging through a pipe, the tradeoffs are summarized in Table 9.1. Four performance metrics are compared: resolution, data collection, computational complexity, and noise performance. The first metric is

resolution. As previously discussed, beamforming and matched filter had poor resolution, which was the motivation for investigating methods that offer superior resolution, such as MUSIC and CS. Therefore, beamforming and matched filter processing should only be used when the size of the pipe is large enough to provide the desired resolution. For data collection, monostatic is preferred due to the simpler logistics of the data collection. Bistatic data collection provides more information, which is useful in its own right, but requires more time to collect and a more complicated collection processes. If simplicity is desired, either matched filter or CS must be used. CS seems to be the algorithm of choice when it comes to resolution and simplicity in data collection. However, CS was found to be computationally slow. The solvers used in CS are iterative and take a significant amount of time to run. MUSIC is less complex, as it involves an eigen decomposition and a set of projections. Projections involve solving a set of linear equations, which are solved efficiently and have low computational complexity. The simplest methods are the beamforming and matched filter methods, which only involve projections. However, if matching pursuit is used with matched filter processing the algorithm becomes iterative, which increases the complexity on par with CS. The final metric is the noise performance of the algorithm. Matched filter has the best performance, because typical matched filter processing involves coherently processing a large number of data samples, which suppresses incoherent noise. If the same number of samples were used with the other three methods, similar noise performance should be expected. However, the other three methods typically operate on a smaller number of data samples due to more complex data collection for beamforming and MUSIC, and the computational complexity of CS.

Reducing the number of data samples processed hurts the noise performance. Overall, it is not possible to state that one method is the best overall. All the methods work well and the best method for the job will depend on the operational scenario.

Table 9.1: Imaging Tradeoffs.

	Resolution	**Data Collection**	**Computational Complexity**	**Noise Performance**
Beamforming	Poor	Bistatic required	Fast	Moderate
Matched Filter	Poor	Monostatic/bistatic	Fast	Good
MUSIC	Good	Bistatic required	Moderate	Moderate
Compressed Sensing	Good	Monostatic/bistatic	Slow	Moderate

The final two chapters of the dissertation represent some exploratory work to extend the topic of through-pipe imaging. Chapter 7 discusses a proposed method for computing the transmission through a pipe channel with an arbitrary structure. The method employs the generalized scattering matrix in order to continue using the closed form solutions for the coupling into and radiation from a pipe. While results for low frequencies showed promise, it was difficult to get convincing agreement with measurement data for higher frequency transmission. This is attributed to the more stringent modeling and meshing requirement for the geometry at higher frequencies.

Chapter 8 discussed the application of a new joint time-frequency (JTF) distribution to the analysis of electromagnetic backscattering data. This new JTF is derived from the Wigner-Ville distribution and leverages the recent advances in CS. The CS-based JTF was applied to backscattering data from a pipe and compared to the STFT. The time and frequency localization achieved using the CS based approach was shown to

be superior to the STFT. In addition to the pipe, the method was also demonstrated on backscattering data from a rotating blade. This showed the broader application of this JTF method to other signals often encountered in radar signature analysis.

There are several directions that research could follow from the work reported here. Following directly from the work done in Chapter 7, a better way of modeling the transmission through complex pipe channels should be explored. It may be too difficult to accurately model the higher-order modes using a full-wave solver. Therefore, it may be more reasonable to explore higher-frequency methods such as SBR for computing the transmission through a complex pipe. We restricted ourselves in the initial work because it was desirable to continue using the closed-form solutions for the radiation from and coupling into a pipe. However, it may not be practical to continue using those solutions for large pipes at high frequencies.

From an imaging perspective, a straightforward extension would be to generalize the two-dimensional methods presented here to three-dimensions. This would involve obtaining the elevation DOA, in addition to the range position and azimuth DOA. Each of the four imaging methods can be extended to extract the elevation DOA. It would also be useful to develop robust sampling criteria for imaging through a pipe. It is understood that the number of propagating modes inside the pipe dictates the degrees of freedom, which directly translates to the maximum number of non-redundant transceivers. However, it is unclear where the transceivers should be placed for optimal control. In the imaging examples of this dissertation, the position of the transceivers did not have a detrimental effect on the imaging performance. But it would still be useful to explore

optimal positioning. Chapter 6 introduced the concept of mutual coherence, which determines whether CS will work properly for a given set of bases. Mutual coherence also has implications in the other three methods, such as the sidelobe levels in beamforming and matched filter processing, and ambiguities in MUSIC. Therefore, moving forward it would be useful to explore the best transceiver configurations to minimize the mutual coherence. From the experience gained in this research it can be foreseen that the sampling criteria will be a function of the pipe size.

Throughout this dissertation, when imaging through a pipe, it has been assumed that the pipe structure is known. However, in a real-world scenario this may not be the case. Therefore, it would be useful to find a method for predicting the pipe channel. One possible approach would be to use an adaptive imaging procedure. An adaptive approach would be an iterative procedure that would first form an image with assumed channel parameters. Then a set of metrics would determine the quality of the image and an updated set of channel parameters would be produced. The procedure would be repeated until a stop condition was reached based on image quality. The primary challenge here is finding a set of metrics that would successfully discriminate between the correct channel parameters and all the other possibilities. A successful approach here would also be applicable to mapping out unknown tunnel or cave networks.

It would also be interesting to explore other waveguide structures. The ideas and methods here easily translate to waveguide-like structures with different cross-sections, such as rectangular waveguides. More interesting would be modal propagation through hollow dielectric structures. In the case of hollow dielectric waveguides, there are

approximate modal series that can be used to describe the propagation through the waveguide [85][89]. It would be interesting to explore these modes and determine the transmission characteristics and explore the potential for imaging through a tunnel or cave network.

Using pipes as a channel for collected backscattering data and forming images offers a new set of challenges and interesting applications. In this dissertation it was shown that radar imaging through a pipe is indeed possible. There are two primary contributions of this work. First, the ability to use a pipe to collect backscattering data and methods for imaging that data were successfully demonstrated through simulation and measurement. Second, it was shown that many imaging algorithms devised for free space can be adapted to backscattering data collected through a waveguide channel in an efficient and robust manner.

Further investigation and work are needed before an operational implementation of building interior reconnaissance through pipes and ducts can be achieved. However, the work done in this dissertation establishes an initial framework for how to collect building interior reconnaissance through a waveguide-like structure such as a pipe or duct. The research done here, on imaging through a pipe, lays the ground work for moving forward and works well as a proof of concept for imaging through real-world pipes or ductwork. In addition, this work is not necessarily limited to building interior reconnaissance and there are perhaps more ingenious applications of this work that will be devised in the future.

Appendix A

This appendix discusses measurement equipment and techniques used in this dissertation. First, the equipment used is described. Then, the techniques used to collect backscattering data are discussed.

Measurements are made using a vector network analyzer (VNA). In particular, the Agilent PNA-L N5230A 2-port VNA is used for all measurements. The Agilent PNA-L can operate from 10 MHz to 20 GHz. The output power of the VNA is adjustable up to 25 dBm, but for measurement the power is typically set to 9 dBm. For data collection, the VNA has two modes of operation, Continuous Wave (CW) and Frequency-Sweep. In CW mode the VNA emits a constant frequency waveform and collects time-domain data. In the Frequency-Sweep mode, the VNA uses a linear stepped-frequency waveform to collect frequency-domain data.

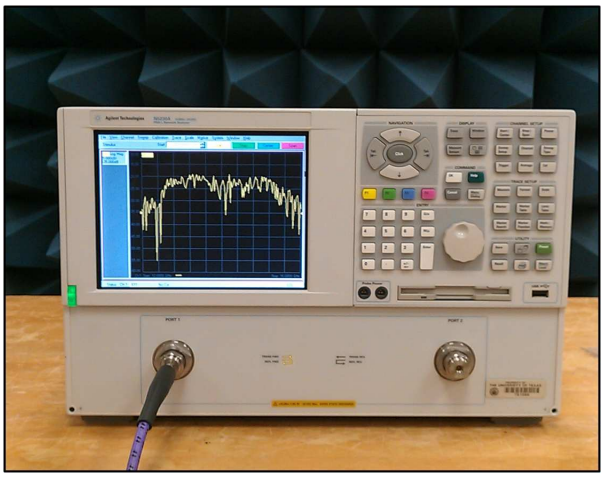

Figure A.1: Agilent PNA-L N5230A PNA-L VNA.

For propagation and backscattering measurements, horn antennas are used. Two different sets of horn antennas were available. For broadband measurements TDK HRN-

0118 horns were used. The TDK horn operates from 1 to 18 GHz, with an average gain of 12 dB. In addition to the TDK horns, at set of Narda model 639 Ku band horns were also available. These horns operate from 12 to 18 GHz and have an average gain of 16.5 dB. Whenever possible the Narda horns were used over the TDK horns, due to the superior gain of the Narda horns. The horns are connected to the VNA through coaxial cable with SMA connections.

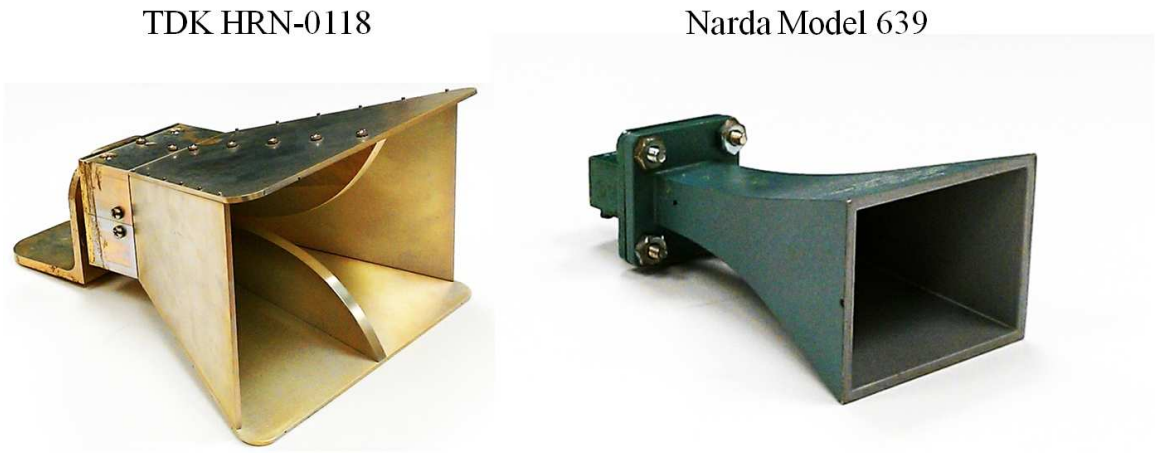

Figure A.2: Horn antennas used for measurements.

Making backscattering measurements using the equipment above is discussed here. The VNA measures two-port S-parameter data. Monostatic data are collected by measuring S11 or S22, depending on which port the horn is connected to. Bistatic data are collected by taking S12 or S21 data and using two horns for measurement. Backscattering data are collected in the far field region of the target and horn antennas. However, in some instances it is not possible to collect far field data. In these cases a method for converting near-field backscattering data into far-field backscattering data can

be used, which is described in Appendix B. For all backscattering measurements, background subtraction is used to suppress backscattering from clutter. Background subtraction involves taking two measurements. First, backscattering data are collected of the scene with clutter and target presents. Second, the target is removed and data of the scene are collected, which only includes the clutter now. The two data sets are subtracted, which results in backscattering data with clutter removed. Background subtraction helps suppress backscattering from the horn antennas itself when making measurements though S11 or S22 and reduces coupling when measuring through S12 or S21. In the backscattering measurement, a corner reflector is used as a target, as shown in Fig. A.3. The corner reflector is used because it serves as a good point scatterer.

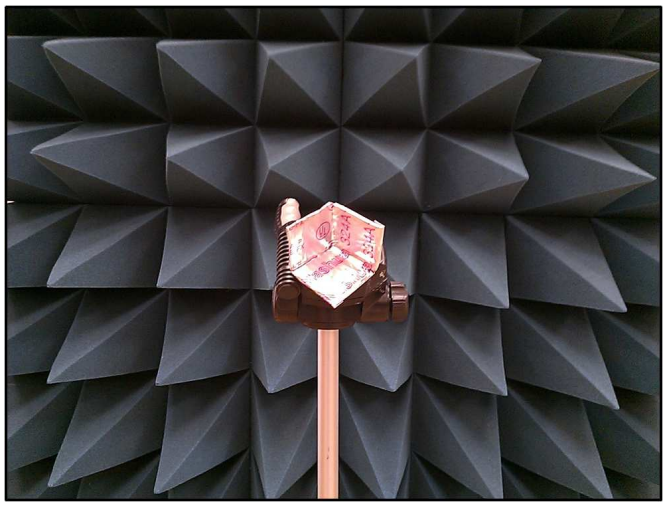

Figure A.3: Corner reflector used as a point scatterer in measurement.

In this dissertation the two-port VNA is used to make all backscattering measurements. Two collection schemes are used, synthetic aperture and phased array. In synthetic aperture measurements, monostatic backscattering data are collected along a

baseline. The procedure for synthetic aperture measurements is to collect S11 data at each array position and then move the horn antenna to the next position. For phase array measurements bistatic data are collected for each transmitter/receiver position. The procedure for phase array measurements involves two steps. First, the transmitter is positioned. Second, the bistatic data are measured for each receiver position, which involves moving the horn to each receiver position and measuring S12 or S21. The transmitter is moved to each transmit position and the measurements are repeated. The measurement setup used for collected backscattering data through a pipe is shown in Fig. A.4. The pipe is embedded in absorbers to be sure that transmission only takes place through the pipe. The target is placed on the right-side of the pipe and backscattering data are collected on the left-side of the pipe using the procedures described in this Appendix.

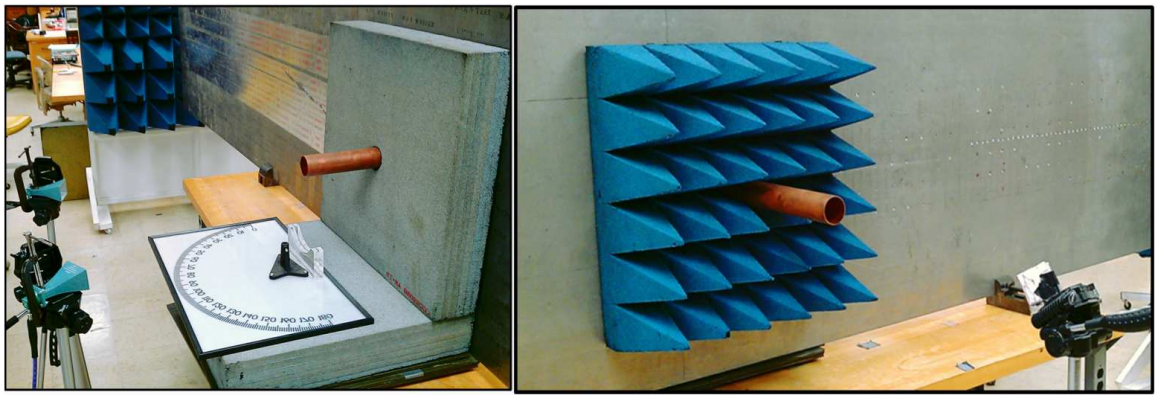

Figure A.4: Backscattering through a pipe measurement setup.

Appendix B

B.1 INTRODUCTION

This Appendix discusses a near-field to far-field transformation and its application to Doppler backscattering from wind turbines. The growth in the number of wind farms for power generation has caused concern within the radar community on the effect of wind turbines on existing radar infrastructure [90][91]. The large size and rotational movement of wind turbines generate significant radar cross section (RCS) and Doppler clutters, which may interfere with the detection of moving targets such as storms and aircraft. In 2006 the Department of Defense commissioned a study to measure and simulate the time-varying RCS from a 1.5 MW GE windmill [92][93]. In the study it was found that the largest contribution to the Doppler signatures was from the blade flashes. Other weaker features such as tip returns and multiple interactions were noted. These Doppler features were recently examined in more detail through simulations and scaled model measurements [94]. It was reported that the blade shape can give rise to rather unique Doppler features. A problem that is difficult to overcome when making measurements of wind turbines, even for scaled models, is the satisfaction of the far-field criterion. This is due to the very large physical and electrical size of wind turbines at typical radar frequencies of interest. For example, the measurement of a 1 m scaled model at 15GHz requires a distance on the order of $2(D^2/\lambda)$=100m to satisfy the far-field criterion. Since it was not possible to satisfy this criterion in [94], some near-field effects were observed. The most notable distortion was the tilting of the blade flashes in the

Doppler spectrogram. Therefore, it would be useful to apply a near-field to far-field transformation (NFFFT) algorithm to obtain a true picture of the Doppler features of turbines in the far field.

Many NFFFT algorithms have been proposed to date [95]-[99]. The most well-known is the algorithm developed by LaHaie et al. [95][96]. The algorithm is theoretically rigorous but requires the frequency derivative of the near-field RCS data, which necessitates the collection of multi-frequency data. Other image-based algorithms [97][98] also require multi-frequency, multi-angle data collection in the near field. A simpler algorithm was proposed earlier by Mensa and Vaccaro [99] (hereafter referred to as Mensa's algorithm for brevity) that transforms *single-frequency*, monostatic near-field data to the far-field RCS of the target. This algorithm is physically intuitive and well suited for our Doppler signature study. However, while this algorithm has been used in a number of applications to date, the angular sampling requirement for near-field data collection is not well documented in the literature.

The objectives of this Appendix are twofold. First, we set out to derive a set of angular sampling criteria for Mensa's algorithm. Second, we aim to apply Mensa's algorithm with the newly derived sampling criteria to obtain the far-field Doppler signatures of wind turbines based on near-field measurement data. This Appendix is organized as follows. In Section B.2, we provide a summary of Mensa's algorithm based on Huygens' principle and the stationary phase approximation. In Section B.3, we derive a set of angular window and sampling criteria for Mensa's algorithm in terms of the near-field distance and target size. In Section B.4, we present results from both simulation and

measurement of wind turbine models after applying Mensa's algorithm. It will be shown that the Doppler features due to blade shapes can be significantly different between the near field and far field. Conclusions are given in Section B.5.

B.2 MENSA'S NEAR-FIELD TO FAR-FIELD ALGORITHM

We begin with a review of Mensa's algorithm, which was originally motivated by the compact range concept. Here, we reformulate Mensa's algorithm more explicitly in terms of Huygens' (or the equivalence) principle and the stationary phase approximation, which will enable us to address the angular window and sampling criteria in Section B.3. In the original work of [99], a few simplifying assumptions were made in the formulation and will be adopted here: (i) scalar wave theory, (ii) point scatterer model of the target scattering with no multiple interactions among the point scatterers, (iii) one-dimensional angular RCS data collection in the waterline plane of the target, and (iv) correcting the phase of the near-field data is of primary concern (as this corresponds to correcting the position of the point scatterers in the final radar image). Fig. B.1 shows the problem geometry, where a plane wave field $E^{i,ff}$ is incident on a point target and the scattered far field $E^{s,ff}$ is observed in the direction of the incident field. The objective of Mensa's algorithm is to relate the scattered far field $E^{s,ff}$ to the incident and scattered fields in the near-field region of the target.

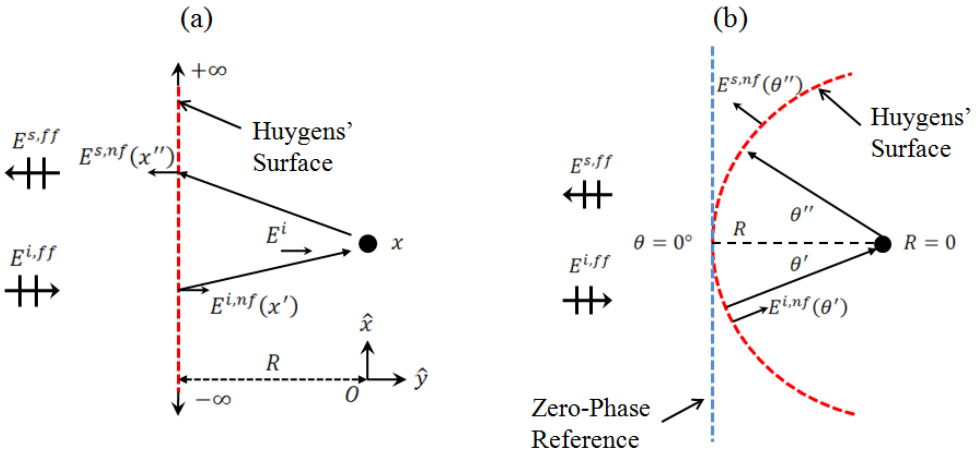

Figure B.1: Problem geometry for single point scatterer with a: (a) linear Huygens' surface (b) circular Huygens' surface.

Based on the equivalence principle, a Huygens' surface can be chosen in the near-field region of the target and an equivalent source can be placed on this surface to produce the same incident field on the target E^i as the original plane wave $E^{i,ff}$. By choosing a planar Huygens' surface (Fig. B.2(a)) at a distance R from the origin, the incident field on the target E^i is expressed in terms of the equivalent source according to

$$E^{i,ff} = E^i = \int_{-\infty}^{\infty} E^{i,nf}(x') e^{-jk\sqrt{R^2+(x-x')^2}} dx' \tag{B.1}$$

where x is the position of the target and $E^{i,nf}$ is the incident plane wave $E^{i,ff}$ observed on the Huygens' surface, which is in the near-field region of the target. Similarly, Huygens' principle relates the scattered far field $E^{s,ff}$ to the scattered near field $E^{s,nf}$ observed on the same planar Huygens' surface through the expression

$$E^{s,ff} = \int_{-\infty}^{\infty} E^{s,nf}(x'') dx'' \tag{B.2}$$

where $E^{s,nf}$ is the scattered field from the target observed on the Huygens' surface, which is in the near-field region of the target. Finally, using the point scatterer model [100], the scattered near field $E^{s,nf}$ is related to the incident field E^{i} through the expression

$$E^{s,nf}(x'') = S \cdot E^{i} e^{-jk\sqrt{R^2+(x-x'')^2}} \tag{B.3}$$

where the phase factor accounts for the phase delay from the scatterer back to the Huygens' surface and S denotes the scattering strength of the point target. By combining (B.1)-(B.3), the scattered far field $E^{s,ff}$ is given by:

$$E^{s,ff} = \int_{-\infty}^{\infty} e^{-jk\sqrt{R^2+(x-x'')^2}} dx'' \int_{-\infty}^{\infty} e^{-jk\sqrt{R^2+(x-x')^2}} dx' \tag{B.4a}$$

$$\cong e^{-jkR}\sqrt{\frac{2\pi R}{jk}} e^{-jkR}\sqrt{\frac{2\pi R}{jk}} = e^{-j2kR}\frac{2\pi R}{jk} \tag{B.4b}$$

In deriving (B.4a), both S and $E^{i,nf}$ have been set to unity for simplicity. The latter is done since for an incident plane wave, the field on the planar Huygens' surface is equi-phase and uniform in magnitude. By applying the method of stationary phase [101] to the integrals in (B.4a), an approximate closed form expression for the scattered far field $E^{s,ff}$ is obtained and shown in (B.4b). The implication of (B.4a) is that the backscattered far field $E^{s,ff}$ can be found by measuring the backscattered near field at each location on the Huygens' surface $E^{s,nf}(x'')$, due to an incident field from each location $E^{i,nf}(x')$, also on the Huygens' surface. The measurements required to realize this scenario are the full bistatic response of the target, i.e. for each incident location x' the scattered field at all locations x'' on the Huygens' surface must be measured.

Acquiring full bistatic data is a laborious measurement to make in practice, therefore a monostatic expression is much preferred.

We next consider monostatic backscattering data collected along the planar Huygens' surface for the point target in Fig. B.1. Scattering from the target is still described by (B.3) where E^i is now the field incident from the observation position x''. The incident field E^i includes a phase delay from the Huygens' surface to the point target, and is exactly equal to the phase delay due to the return trip shown in (B.3). If we choose to integrate this monostatic backscattered field along the Huygens' surface while again setting the scattering strength S of the target and the strength of the incident field to unity, the following expression is obtained:

$$\int_{-\infty}^{\infty} e^{-j2k\sqrt{R^2+(x-x'')^2}}\,dx'' \tag{B.5a}$$

$$\cong e^{-j2kR}\sqrt{\frac{2\pi R}{j2k}} \tag{B.5b}$$

It should be noted that the integration of the monostatic backscattering, (B.5a), is not an application of Huygens' principle, but a chosen mathematical operation on the backscattering data. By the method of stationary phase, (B.5a) can again be evaluated approximately in closed form as indicated in (B.5b). Lastly, the observation is made that, except for an unimportant scaling constant, the stationary phase solution, e^{-j2kR}, to the scattered far field $E^{s,ff}$ in (B.4b) is identical to that in (B.5b). Since obtaining the correct far field phase is the primary concern, (B.5a) is in fact an NFFFT that operates on monostatic data. That is, by simply integrating monostatic near-field data collected along a planar Huygens' surface, the desired far field data are recovered.

To further simplify the data collection, the same derivation in (B.1)-(B.5) is applied to a circular Huygens' surface, shown in Fig. B.1(b). The point target in Fig. B.1(b) is placed at the center of the circle for simplicity in derivation, although this is not a necessary condition. The field incident on the target E^i is expressed in terms of the fields on the Huygens' surface $E^{i,nf}(\theta')$ according to:

$$E^{i,ff} = E^i = \int_{-\pi}^{\pi} E^{i,nf}(\theta') e^{-jkR} R d\theta' \tag{B.6}$$

In the case of the planar Huygens' surface the incident field $E^{i,nf}$ was equi-phase and uniform in magnitude. However, for the circular Huygens' surface the incident field in the near-field region $E^{i,nf}(\theta')$ for a plane wave incident is given by

$$E^{i,nf}(\theta') = e^{-j2kR \sin^2\left(\frac{\theta'}{2}\right)} \tag{B.7}$$

where the zero-phase reference is indicated in Fig. B.1(a). By using (B.7) and the same procedure outlined in (B.1)-(B.4) the scattered far field is given by:

$$E^{s,ff} = \int_{-\pi}^{\pi} e^{-j2kR \sin^2\left(\frac{\theta''}{2}\right)} e^{-jkR} R d\theta'' \int_{-\pi}^{\pi} e^{-j2kR \sin^2\left(\frac{\theta'}{2}\right)} e^{-jkR} R d\theta' \tag{B.8a}$$

$$\cong e^{-jkR} \sqrt{\frac{2\pi R}{jk}} e^{-jkR} \sqrt{\frac{2\pi R}{jk}} = e^{-j2kR} \frac{2\pi R}{jk} \tag{B.8b}$$

Since Huygens' principle is equivalent for any arbitrary surface, (B.8a) must result in the same answer as (B.4a). Therefore, the integrals in (B.8a) have the same solutions as the integrals of (B.4a). The closed form stationary phase approximation for

(B.8a) is shown in (B.8b) which is a repeat of (B.4b). The implication of (B.8a) is that the far field can be recovered from full bistatic measurements of the target made on a circular Huygens' surface. However, as in the case of the planar Huygens' surface, an NFFFT that operates on monostatic backscattering data is much preferred. Following the same argument used for the planar Huygens' surface, the monostatic data along the circular Huygens' surface are integrated. The integration of monostatic backscattering from the point scatterer along the circular arc, combined with the phase delay of (B.7) results in the following:

$$\int_{-\pi}^{\pi} e^{-j2kR\sin^2\left(\frac{\theta'}{2}\right)} e^{-j2kR} R d\theta' \tag{B.9a}$$

$$= e^{-j2kR}\sqrt{\frac{2\pi R}{j2k}} \tag{B.9b}$$

The integral in (B.9a) is similar to the integrals of (B.8a) and can be approximated using the method of stationary phase, with the closed form solution indicated in (B.9b). As before, it is observed that the stationary phase solution in (B.9b) is identical to that of the far field $E^{s,ff}$ of (B.8b), except for a constant. Therefore, the far field can be reconstructed by simply integrating the monostatic near-field data collected on a circular arc weighted by $e^{-j2kR\sin^2(\theta/2)}$. In practice, such monostatic data are more conveniently collected by keeping the radar stationary and rotating the target, i.e., in the inverse synthetic aperture radar (ISAR) mode.

B.3 ANGULAR WINDOW AND SAMPLING CRITERIA

While Mensa's algorithm is very simple to implement, one open question that is yet to be addressed is the angular window and sampling criteria in the integration of the monostatic near-field data. Since Mensa's algorithm is based on Huygens' principle, it may appear that the near field should be integrated over a completely closed surface in order to accurately recover the far field. However, it is recognized that the dominant contribution to the integral occurs around the stationary phase points. In fact, the integrand becomes highly oscillatory away from the stationary phase points such that it would require very fine angular sampling to achieve an accurate numerical integration. Therefore, it is important to determine the proper angular window and the corresponding angular sampling that can ensure an accurate numerical implementation of Mensa's NFFFT. We begin the discussion with a linear collection aperture and the evaluation of (B.5a). Sampling criteria are sought that will establish an expression for the integration window and sampling interval in the stationary phase integral

$$\int_{-X_{win}}^{X_{win}} e^{-j2k\sqrt{R^2+x^2}}dx = \sum_{x=-X_{win}}^{X_{win}} e^{-j2k\sqrt{R^2+x^2}}\Delta x \tag{B.10}$$

where the integration window $2X_{win}$ is centered around the stationary phase point. We postulate that the integration window X_{win} must be large enough to capture an integral number of oscillations of the integrand. By taking the first two terms of the Taylor series expansion of the phase function in (B.10), the number of oscillations captured by X_{win} is given by:

$$n = \frac{k{X_{win}}^2}{2\pi R} \tag{B.11}$$

Once the number of oscillations n is chosen, X_{win} can be determined from (B.11). As an example, the window size of the integration is varied and compared to the approximate closed form solution of (B.10), found using the stationary phase method. Fig. B.2 shows the magnitude and phase of evaluating (B.10) for various window sizes (normalized to R). For comparison, the magnitude and phase of the stationary phase solution to (B.10) is also shown in Fig. B.2. The sampling interval is chosen to be very small to ensure convergence. From Fig. B.2, it is found that the minimum window-size/R that guarantees at most 10° of phase error is 0.25, which corresponds to approximately three oscillations. This lower bound for n is relatively independent of R, and will be used as a guideline to derive the sampling interval next.

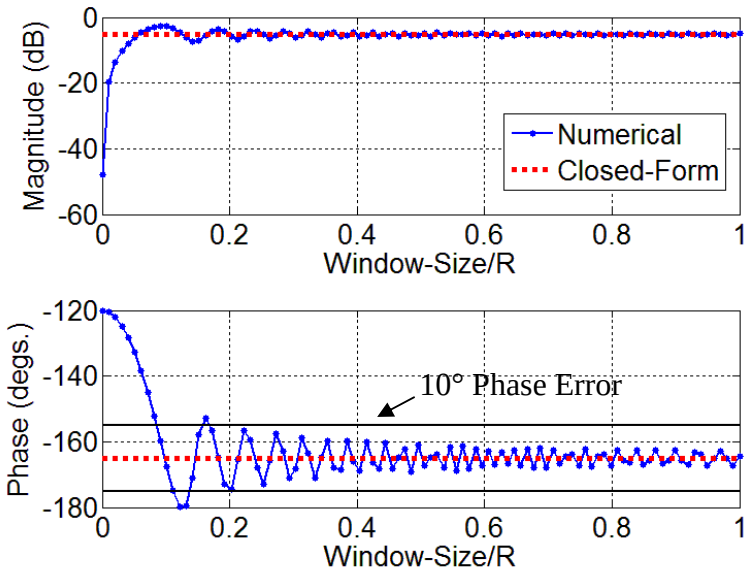

Figure B.2: Numerical integration of (10) at 10GHz for R = 10 m and Δx = 2 mm.

The proper sampling interval Δx can be determined by finding the highest spatial frequency component, K_{max}, of the integrand in (B.10) such that

$$\Delta x = \frac{2\pi}{2K_{max}} \tag{B.12}$$

K_{max} is determined by first solving for the instantaneous spatial frequency k_{inst} of the integrand in (B.10) as follows:

$$k_{inst} = \frac{\partial \Psi(x)}{\partial x} \tag{B.13}$$

where $\Psi(x)$ is the phase function of the exponential. Using the phase function $2k\sqrt{R^2 + x^2}$ from (B.10) the instantaneous spatial frequency k_{inst} is:

$$k_{inst} = -2k\frac{x}{\sqrt{R^2+x^2}} \cong -2k\frac{x}{R} \;\; for \;\; R \gg x \tag{B.14}$$

By recognizing that the highest spatial frequency K_{max} occurs at $x = X_{win}$ and using (B.12), the following expression for the proper sampling interval is obtained:

$$\Delta x = \frac{\lambda R}{4X_{win}} \tag{B.15}$$

We test the sampling criterion in (B.15) through a numerical example at a frequency of 10 GHz and . Using and applying (B.11) sets the integration window size to $X_{win} = 1.34\, m$. Fig. B.3 shows the numerical results of evaluating (B.10) for various sampling intervals. Equation (B.15) dictates that the sampling interval Δx should be 0.22 m which corresponds to 12 samples. Indeed, the solution is seen to be at the onset of

convergence at the sampling interval defined by (B.15) in Fig. B.3. Therefore (B.15) sets an approximate upper bound on the necessary sampling interval.

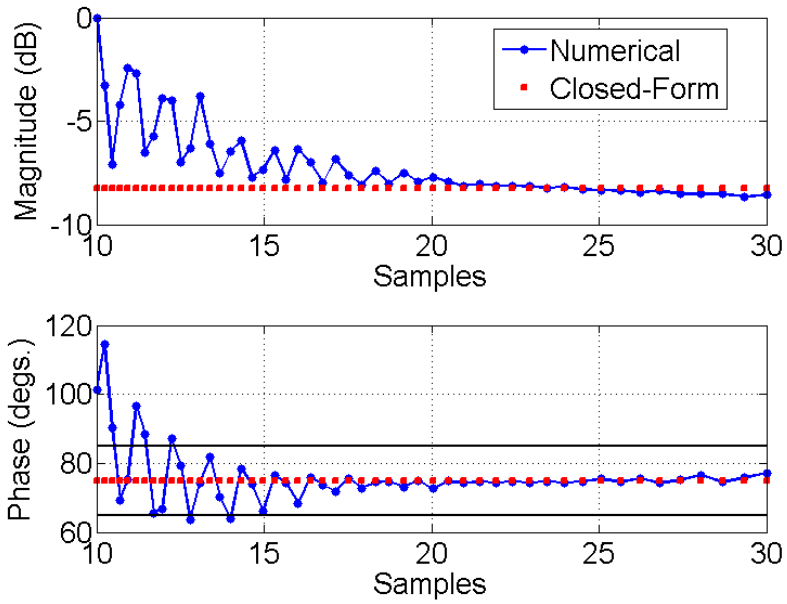

Figure B.3: Test sampling interval for a frequency of 10 GHz and Xmax = 1.34 m.

To establish sampling criteria for a circular collection aperture, the sampling criteria for numerical evaluation of (B.10) are converted from Cartesian to polar coordinates. The conversion is performed by applying $X_{win} = R\theta_{win}$ and $\Delta x = R\Delta\theta$ under the small angle assumption. The final sampling criteria to transform monostatic near-field data collected on either a linear or circular aperture to the far field are summarized in Table B.1. An example is illustrated in applying the circular aperture sampling criteria of Table B.1. A plate target was simulated using an array of points spaced 0.1 cm apart spanning 20 cm in length at a frequency of 10 GHz. Fig. B.4 shows the monostatic far-field backscattering of the plate and the monostatic near-field

backscattering simulated at a distance of $R = 1\,m$ from the center of the plate. The sampling criteria in (B.11) and (B.15) were established for a single point scatterer. To determine the sampling criteria for a target made up of a collection of point scatterers, the total extent of the target must be considered. Based on the dimensions of the plate the integration window is determined to be $\theta_{win} = 17.2°$ from Table B.1. This is the angular window required to capture each stationary phase point and must be centered around each point scatterer. The full integration window θ_{max} used for the NFFFT should therefore extend θ_{win} beyond the last point scatterer. To find the proper θ_{max}, the maximum angular extent θ_{ext} of the target in either direction needs be found; for the plate example. Consequently, $\theta_{max} = \theta_{win} + \theta_{ext} = 22.9°$ To determine the proper sampling interval $\Delta\theta$ the point scatterer with the largest integration window must be considered. This will be the point scatterer at one edge of the target as it will have an integration window that extends beyond the other edge of the target with a total angular distance of $2\theta_{ext} + \theta_{win}$. For the plate this total angular distance is, $2\theta_{ext} + \theta_{win} = 28.6°$, leading to a sampling interval of $\Delta\theta = 1.7°$. Fig. 7 shows the result of applying $\Delta\theta = 3.4°$ (0.25x sampling), $\Delta\theta = 1.7°$ (0.5x sampling), and $\Delta\theta = 0.85°$ (1x sampling). In all three cases the full integration window θ_{max} is kept the same. From Fig. B.5 it is seen that at 0.5x sampling, the result is rather poor, while at 1x sampling, the result is very good. Therefore, the sampling criteria of Table B.1 establish a good lower bound for the sampling required to recover the far field from monostatic near-field data.

Table B.1: Sampling Criteria For Single Point Scatterer

	Linear Aperture	Circular Aperture
Monostatic Data	$X_{win} = \sqrt{3\lambda R}$ $\Delta x = \frac{\lambda R}{4(2X_{ext} + X_{win})}$	$\theta_{win} = \sqrt{\frac{3\lambda}{R}}$ $\Delta\theta = \frac{\lambda}{4R(2\theta_{ext} + \theta_{win})}$

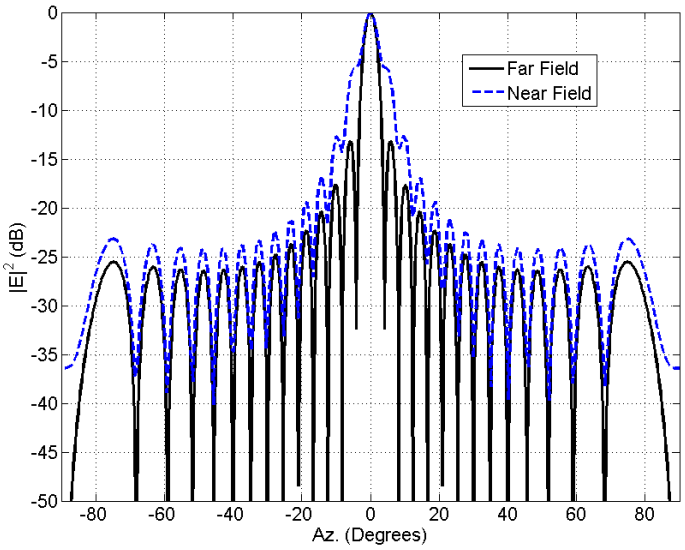

Figure B.4: Near field and far field backscattering from 20 cm plate modeled with point scatterers at 10 GHz.

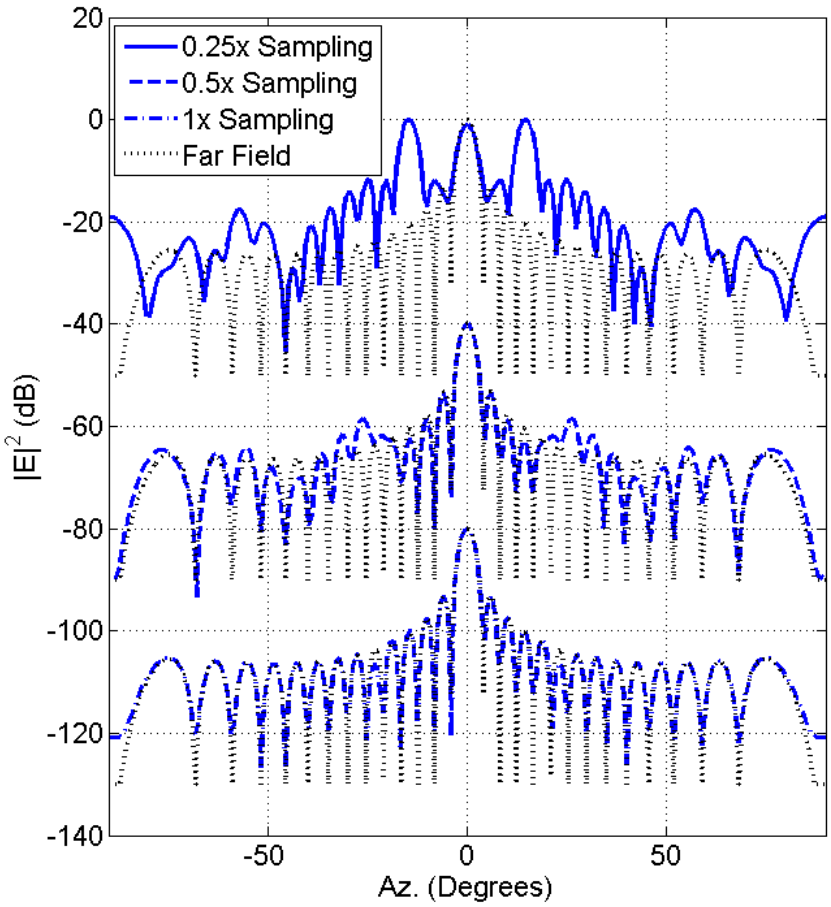

Figure B.5: Monostatic near field backscattering data transformed to far field data.

B.4 TURBINE MEASUREMENTS

Mensa's NFFFT algorithm with the proper window/sampling requirement is applied to two targets. The first target is a simplified three-arm wire model of a turbine, where both full-wave simulations and near-field laboratory measurements have been carried out. The second is a commercial turbine from Bergey Windpower with 2 ft. blades. Near-field measurement data on both targets were reported in [94]. In the first target, the wires are 60 cm in length and backscattering is simulated and measured at 14

GHz. Simulations are first run using FEKO [46] for a single wire positioned along the y-axis with one end at the origin over aspect angles θ=90°, ϕ=[0°, 360°] and θ=90°. The resulting data are then considered as a cyclic time series as the wire spins about one of the ends with a rotation rate of 0.0153 rps. Its short-time Fourier transform is taken for a full cycle, ϕ=[0°, 360°], using a sliding Hamming window. Fig. B.6(a) shows the resulting Doppler spectrogram for the far-field backscattering plotted on a 40 dB dynamic range. In Fig. B.6(a) two strong flashes from the wire are clearly seen, one containing negative Doppler frequencies (as the wire rotates away from the radar) at 16.4 s and one with positive Doppler frequencies (as the wire rotates toward the radar) at 49.1 s. Additional tracks due to scattering from the tips are also evident. The outer track is due to scattering from the outer tip and the zero-Doppler track is due to scattering from the stationary tip. In between these two tracks exists another Doppler track, which is the result of a traveling wave between the two ends of the wire. These Doppler tracks were examined in [94].

Near-field backscattering data for the single wire is simulated on a circular arc at a distance of $R = 3\,m$. Fig. B.6(b) shows the spectrogram for the near-field data processed in the same manner as the far-field data. The most notable effect of collecting data in the near field is the slanting of the flashes. As in the plate example from the previous section, the integration window is determined to be, $\theta_{win} = 8.4°$ and $\theta_{ext} = 11.5°$ therefore, $\theta_{max} = 19.9°$. From the total integration window the sampling interval is determined to be $\Delta\theta = 0.37°$. Since this establishes an upper bound, the sampling interval is chosen to be $\Delta\theta = 0.2°$ in order to obtain more robust results. Fig. B.6(c)

shows the result of transforming the near-field backscattering data of Fig. B.6(b) to the far field. It is clear in Fig. B.6(c) that the flashes from the blade have been corrected and the results agree well with the far field simulation data in Fig. B.6(a). We note that Mensa's derivation assumes single-bounce scattering events. This implies the theory does not apply to the in-between Doppler track resulting from multiple interactions between the ends of the wire. Surprisingly, the in-between track in Fig. B.6(c) and the same track in Fig. B.6(a) still show good agreement.

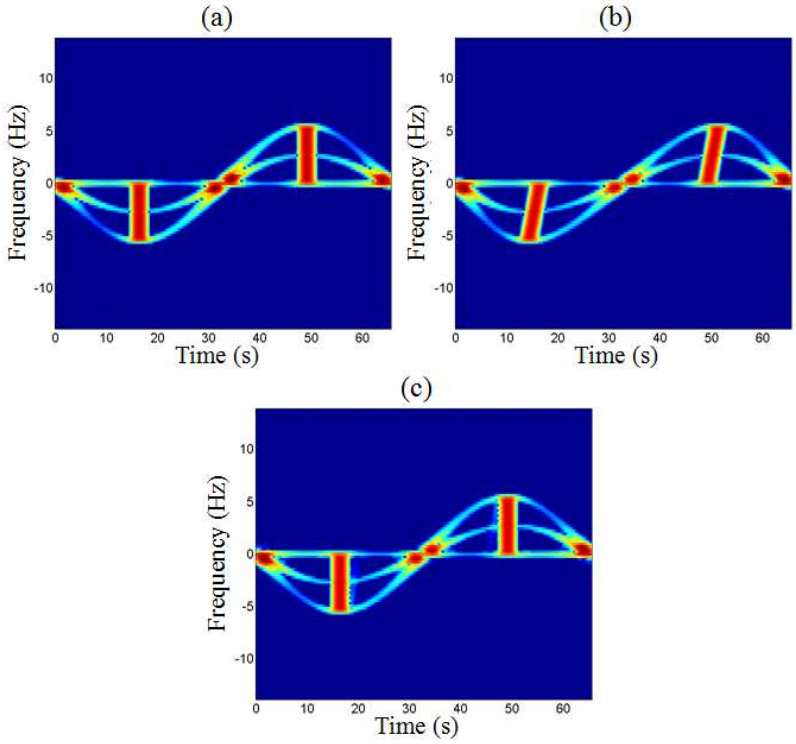

Figure B.6: Spectrogram of simulated backscattering data from a single wire for: (a) far-field backscattering (b) near-field backscattering (b) near-field transformed to far-field backscattering.

Next, a three-arm wire model is measured in the laboratory at 14 GHz. The radar is placed at $R = 1.65\,m$, which for a wire length of 60 cm is in the near-field region of

the target. Data are collected for 360° of target rotation and the spectrogram is shown in Fig. B.7(a) plotted on a 40 dB dynamic range. The strong DC line is due to stationary background clutter. The spectrogram contains three times the number of flashes as that in Fig. B.6(b) due to the three wire arms. The Doppler flashes are again tilted due to the near-field data collection. Next, we apply the NFFFT to the data. The integration window and sampling interval are determined in the same manner as before with $\theta_{win} = 11.3°$ and $\theta_{ext} = 21.3°$ therefore, $\theta_{max} = 32.6°$ and .and $\Delta\theta = 0.4°$. Again, a sampling interval of $\Delta\theta = 0.2°$ is used for more robust results. Fig. B.7(b) shows the result of transforming the near-field data to the far field using the established integration window and sampling interval. It is seen that the flashes are straightened in the far-field results, consistent with the simulation data. Two weak extraneous features are observed in Fig. B.7(b) at the two ends of the spectrogram. This is a result of collecting data for a single rotation of the model and considering the data to be cyclic when applying the NFFFT. A discontinuity at the wraparound point of the data due to slight misalignment generated these extraneous features.

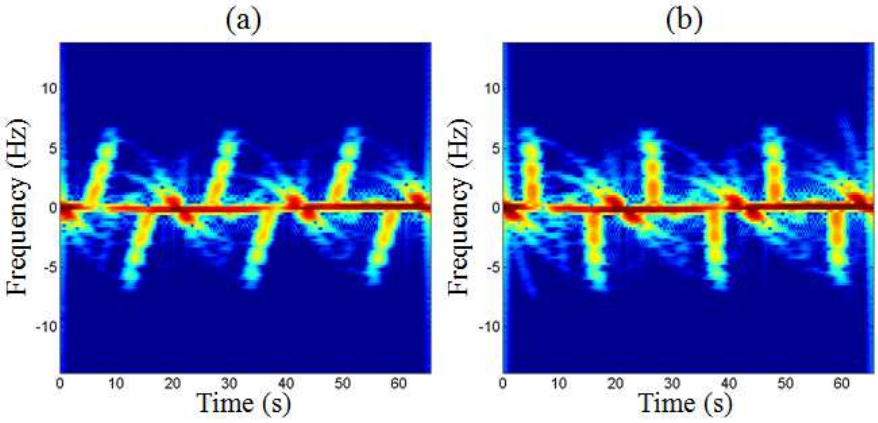

Figure B.7: Measurement data for 3 wire backscattering in (a) near field (b) near field transformed to far field.

Next, we consider the data from a commercial Bergey Windpower turbine shown in Fig. B.8(a). It has approximately the same blade length as the wire model, but the blades are made of carbon fiber material and have a rather complex shape. The data are again collected at 14 GHz on a turntable over 360° of rotation in the near field at $R = 1.65\ m$. The spectrogram of the near field results are shown in Fig. B.9(a). The wire model and Bergey turbine have the same dimensions, therefore the same window and sampling interval are used. The transformed results after the NFFFT are shown in Fig. B.9(b). Interestingly, we observe that for the Bergey turbine the blade flashes become more slanted in the far field, which is contrary to what would be expected based on the simulations and measurements for the straight-wire model in Figs. B.6 and B.7. The same extraneous features as in the wire model are again present at the two ends of the spectrogram of Fig. B.9(b), but they do not impact the key observations.

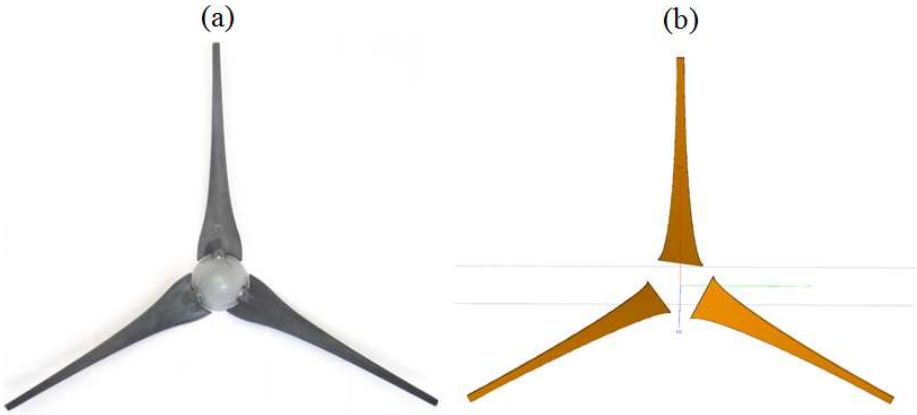

Figure B.8: Bergey Winpower turbine (a) real turbine (b) FEKO model of the turbine.

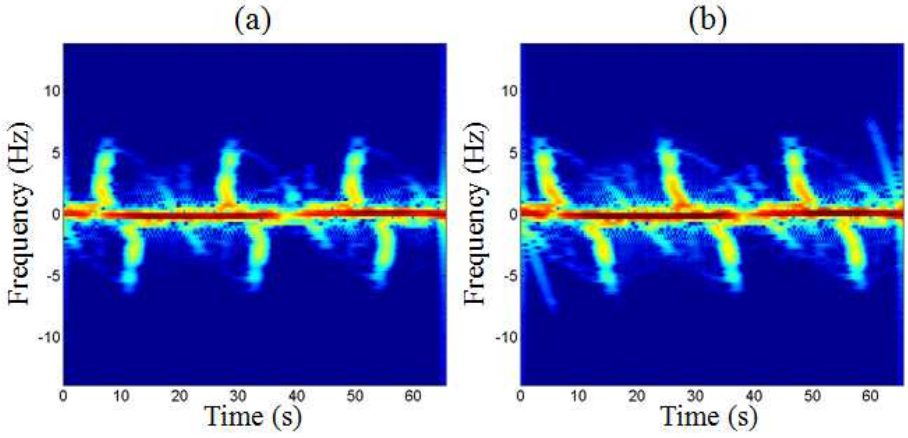

Figure B.9: Measurement data for the Bergey windpower turbine in (a) near field (b) near field transformed to far field.

To further corroborate the measurement data of Fig. B.9, the Bergey turbine is simulated approximately using FEKO's physical optics (PO) solver. The computer model used for the Bergey turbine is shown in Fig. B.8(b). The model is built to take into account the shape, width, and pitch of the blades. While PO is only an approximate solution, it does provide a first-order answer to the problem at hand, especially considering the model inaccuracy, unknown material parameters and large problem size.

Fig. B.10(a) shows the spectrogram from the near-field PO simulation data collected for $R = 1.65\,m$. Fig. B.10(b) shows the spectrogram for the far-field PO simulation. It is noted that the same shape and slant of the blade flashes observed in the measurement in Figs. B.9(a) and B.9(b) are reproduced by the simulation. From the results of the measurement and simulation of the Bergey turbine, it is evident that the shape of the blade can give rise to rather unique Doppler features, and that they are significantly different in the near field and far field.

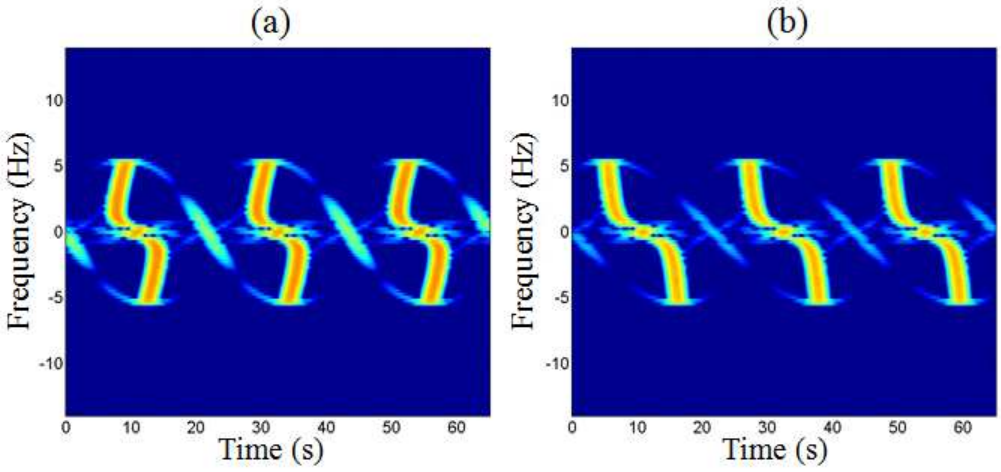

Figure B.10: FEKO simulation of Bergey turbine model (a) near field data (b) far field data.

B.5 CONCLUSION

In this Appendix Mensa's algorithm for transforming near-field backscattering data to the far field was used to derive the Doppler features of wind turbines, where satisfaction of the far-field criterion was infeasible in our measurements. The theoretical basis of Mensa's algorithm was first discussed using Huygens' principle and the stationary phase approximation. Next, angular window size and sampling criteria were

established for a robust implementation of the numerical near-field integration. Mensa's algorithm and the derived sampling criteria were then applied to two wind turbine structures. First, a simplified wire model turbine was simulated using FEKO in the near field and the far field. It was shown that the near field data could be successfully transformed to the far field based on the NFFFT and the derived sampling criteria. Good results were also found using measured data. Next, near-field measurement data from a Bergey Windpower turbine were transformed to the far field. The far field results showed that, in contrast to the wire model, the blade Doppler flashes slant more in the far field. The counter-intuitive results were corroborated by FEKO simulation. The two key findings from this study are: (i) the Doppler flashes are quite different between near-field observation and far-field data, (ii) such differences are strongly dependent on the actual blade shape. These findings are of importance if we want to design signal filtering techniques to remove the Doppler clutters from turbine scattering.

References

[1] E. Baranoski, "Through-wall imaging: historical perspective and future directions," *Journal of the Franklin Institute*, vol. 345, pp. 556-569, Sept. 2008.

[2] S. Ram, L. Yang, A. Lin, and H. Ling, "Doppler-based detection and tracking of humans in indoor environments," *Journal of the Franklin Institute*, vol. 345, pp. 679-699, Sept. 2008.

[3] A. R. Hunt, "A wideband imaging radar for through-the-wall surveillance," *SPIE Proceedings*, vol. 5403, pp. 590-596, 2004.

[4] A. R. Hunt and R. D. Hogg, "A stepped-frequency, CW radar for concealed weapon detection and through the wall surveillance," *SPIE Proceedings,* vol. 4708, pp. 99-105, 2002.

[5] S. Nag, M. A. Barnes, T. Payment, and G. W. Holladay, "An ultra-wideband through-wall radar for detecting the motion of people in real time," *SPIE Proceedings,* vol. 4744, pp. 48-57, 2002.

[6] G. Franceschetti, J. Tatoian, D. Giri, and G. Gibbs, "Timed arrays and their application to impulse SAR for through-the-wall imaging," *IEEE Antennas Propag. Soc. Int, Symp. Digest*, vol. 3, pp. 3067-3070, June 2004.

[7] A. M Attiya, A. M. Bayram, A. Safaai-Jazi, and S. M. Raid, "UWB applications for through wall detection," *IEEE Antennas Propag. Soc. Int, Symp. Digest*, vol. 3, pp. 3079-3082, June 2004.

[8] Y. Yang and A. E. Fathy, "See-through-wall imaging using ultra-wideband short-pulse radar system," *IEEE Antennas Propag. Soc. Int, Symp. Digest*, vol. 3B, pp. 334-337, July 2005.

[9] Y. Wang, Y. Yang, and A. E. Fathy, "Reconfigurable ultra-wide band see-through-wall imaging radar system," *IEEE Antennas Propag. Soc. Int, Symp. Digest*, pp. 1-4, June 2009.

[10] T. B. Gibson and D. C. Jenn, "Prediction and Measurement of Wall Insertion Loss," *IEEE Trans. Antennas Propag.*, vol. 47, no.1, pp. 55-57, Jan. 1999.

[11] S. S. Ram, C. Christianson, Y. Kim, and H. Ling, "Simulation and analysis of human micro-dopplers in through-wall environments," *IEEE Trans. Geosci. Remote Sens.*, vol. 48, no. 4, pp. 2015-2023, April 2010.

[12] R. J. Burkholder, R. J. Marhefka, and J. L. Volakis, "Radar imaging through cinder block walls and other periodic structures," *IEEE Antennas Propag. Soc. Int, Symp. Digest,* pp. 1-4, July 2008.

[13] M. Dehmollaian and K. Sarabandi, "An approximate solution of scattering from reinforced concrete walls," *IEEE Trans. Antennas Propag.*, vol. 56, no. 8, pp. 2681-2690, August 2008.

[14] V. Schejbal, P. Bezousek, D. Cermak, Z. Nemec, O. Fiser, and M. Hajek, "UWB propagation through walls," *Radioengineering,* vol. 15, no.1, pp. 17-24, April 2006.

[15] A. Muqaibel and A. Safaai-Jazi, "Characterization of wall dispersive and attenuative effects on UWB radar signals," *Journal of the Franklin Institute,* vol. 345, pp.640-658, Sept. 2008.

[16] G. Greneker and E. O. Rausch, "Wall characterization for through-the-wall radar applications," *SPIE Proceedings,* vol. 6947, pp. 1-11, 2008.

[17] M. Dehmollaian and K. Sarabandi, "Refocusing through building walls using synthetic aperture radar," *IEEE Antennas Propagat. Soc. Int, Symp. Digest*, pp. 1465 – 1468, June 2007.

[18] M. Dehmollaian, M. Thiel, and K. Sarabandi, "Through-the-wall imaging using differential SAR," *IEEE Trans. Geosci. Remote Sens.*, vol. 47, no. 5, pp 1289-1296, May 2009.

[19] F. Ahmad and M. G. Amin, "High-resolution imaging using Capon beamformers for urban sensing applications," *Proc. IEEE Int. Conf. Acoustics, Speech Signal Processing,* pp. 985-988, April 15-20, 2007, Honolulu, HI.

[20] F. Ahmad, M. G. Amin, and S. A. Kassam, "Synthetic aperture beamformer for imaging through a dielectric wall," *IEEE Trans. Aerosp. Electon. Syst.,* vol. 41, no. 1, pp. 271-283, January 2005.

[21] D. D. Stancil, O. K. Tonguz, A. Xhafa, A. Cepni, P. Nikitin, and D. Brodtkorb, "High-speed internet access via HVAC ducts: a new approach," *Proc. IEEE Global Telecomm. Conf. (GLOBECOM'01)*, vol. 6, pp. 3604-3607, San Antonio, TX, Nov. 2001.

[22] O. Heaviside, *Electromagnetic Theory*. London: Benn, 1893, p. 399.

[23] Lord Rayleigh, "On the passage of electric waves through tubes, or the vibrations of dielectric cylinders," *Phil. Mag.,* vol. XLIII, pp. 125-132, 1897.

[24] K. S. Packard, "The origin of waveguides: a case of multiple rediscovery," *IEEE Trans. Microw. Theory Tech.*, vol. 32, pp. 961-969, Sept. 1984.

[25] N. Marcuvitz, *Waveguide Handbook*, vol. 10 of *MIT Radiation Laboratory Series*. McGraw-Hill, New York, 1951.

[26] S. Silver, Microwave *Antenna Theory and Design*, vol. 12 of *MIT Radiation Laboratory Series*. McGraw-Hill, New York, 1949.

[27] S. E. Miller, "Waveguide as a communication medium," *Bell System Tech. Journal*, vol. 33, pp. 1209-1265, Nov. 54.

[28] H. R. Witt and E. L. Price, "Scattering from hollow conducting cylinders," *IEE Proceedings*, vol. 115, pp. 94-99, Jan. 1968.

[29] O. Einarsson, R. E. Kleinman, P. Laurin, and P. L. E. Uslenghi, "Studies in radar cross sections L-diffraction and scattering by regular bodies 4: the circular cylinder," The University of Michigan, Ann Arbor, Mich., Tech. Rep. AD635186, 1966.

[30] C. A. Chuang, C. S. Liang, and S. W. Lee, 'High frequency scattering from an open-ended semi-infinite cylinder,' *IEEE Trans. Antennas Propag.*, vol. ap-23 no. 6, pp. 770-775, Nov. 1975.

[31] T. W. Johnson and D. L. Moffatt, "Electromagnetic scattering by open circular waveguides," *Radio Sci.*, vol. 17, no. 6, pp. 1547-1556, Nov.-Dec. 1982.

[32] L. N. Medgyesi-Mitschang and C. Eftimiu, 'Scattering from wires and open circular cylinders of finite length using entire domain galerkin expansions,' *IEEE Trans. Antennas Propag.*, vol. ap-30, no. 4, pp. 628-636, July 1982.

[33] C.-C. Huang, "Simple formula for the RCS of a finite hollow circular cylinder," *Electronic Lett.*, vol. 19, no. 20, pp. 854-856, Sept. 1983.

[34] C. W. Chuang, P. H. Pathak, and R. J. Burkholder, "A hybrid asymptotic modal-moment method analysis of the EM scattering by 2-D open-ended linearly tapered waveguide cavities," Tech. Rep. 312436-1, 1988 Electrosci. Lab., Dept. Elec. Eng., Ohio State Univ.

[35] R. J. Burkholder, "High-frequency asymptotic methods for analyzing the EM scattering by open-ended waveguide cavities," Ph.D. dissertation, 1989, Ohio State University.

[36] J. J. Boonzaaier and J. A. G. Malherbe, "Electromagnetic backscatter from open-ended circular cylinder with complex termination," *Electronic Lett.*, vol. 23, no. 3, pp. 218-220, Feb. 1989.

[37] H. Ling, R. Chou, and S. W. Lee, "Shooting and bouncing rays: calculating the RCS of an arbitrarily shaped cavity," *IEEE Trans. Antennas Propag.*, vol. 37, pp. 194-205, Feb. 1989.

[38] H. Ling, S. W. Lee, and R. C. Chou, "High-frequency RCS of open cavities with rectangular and circular cross sections," *IEEE Trans. Antennas Propag.*, vol. 37, no. 5, pp. 648-654, May 1989.

[39] P. H. Pathak and R. J. Burkholder, "Modal, ray, and beam techniques for analyzing the EM scattering by open-ended waveguide cavities," *IEEE Trans. Antennas Propag.*, vol. 37, no. 5, pp. 635-647, May 1989.

[40] N. Whitelonis, ”Investigation of ducts as a high-frequency through-the-wall ‘radar pinhole’,” M.S. thesis, Univ. Texas, Austin, TX, Aug. 2009

[41] L. N. Medgyesi-Mitschang and J. M. Putnam, “Electromagnetic Scattering from Ducts with Irregular Edges: Part I – Circular Case,” *IEEE Trans. Antennas Propag*., vol. 36 no. 3, pp. 383-397, March 1988.

[42] L. J. Chu, "Calculation of the radiation properties of hollow pipes and horns," *Journal Applied Physics*, vol. 11, pp. 603-610, Sept. 1940.

[43] A. Moghaddar and E. K. Walton, “Time-frequency distribution analysis of scattering from waveguide cavities,” *IEEE Trans. Antennas Propag.*, vol. 41, no. 5, pp. 677-680, May 1993.

[44] H. Kim and H. Ling, “Wavelet analysis of radar echo from finite-size targets,” *IEEE Trans. Antennas Propag.*, vol. 41, no. 2, pp. 200-207, Feb. 1993.

[45] S. Ram and H. Ling, “Application of the reassigned joint time-frequency transform to wideband scattering from waveguide cavities,” *IEEE Antennas Wireless Propag. Lett.*, vol. 6, pp. 580-583, 2007.

[46] FEKO – Field computations involving bodies of arbitrary shape suite 5.5. Stellenbosch, South Africa: EM Software & Systems – S.A. (Pty) Ltd., 2010.

[47] C. A. Balanis, *Advanced Engineering Electromagnetics*, John Wiley & Sons, 1998.

[48] D. M. Pozar, *Microwave Engineering*, 3rd ed. New York, NY: John Wiley, 2005.

[49] J. R. Mautz and R. F. Harrington, "Computational methods for antenna pattern synthesis," *IEEE Trans. Antennas Propag.*, vol. 23, pp. 507-512, July 1975.

[50] S. Mallat and Z. Zhang, “Matching pursuits with time-frequency dictionaries,” *IEEE Trans. Signal Process.*vol. 41, no. 12, pp. 3397-3415, Dec. 1993.

[51] J. Tsao, and B. D. Steinberg, “Reduction of sidelobe and speckle artifacts in microwave imaging: the CLEAN technique,” *IEEE Trans. Antennas Propag.* vol. 36, no. 4, pp. 543-556, April 1988.

[52] J. Capon, “High-resolution frequency-wavenumber spectrum analysis,” *Proc. IEEE*, vol. 57, pp 1408-1418, Aug. 1969.

[53] J. P. Burg, “The relationship between maximum entropy spectra and maximum likelihood spectra,” *Geophysics*, vol. 37, pp. 375-376, April 1972.

[54] V. F. Pisarenko, “The retrieval of harmonics from a covariance function,” *Geophys. J. Roy. Astron. Soc.*, vol. 33, pp 347-366, 1973.

[55] R. O. Schmidt, “Multiple emitter location and signal parameter estimation,” *Proc. RADC Spectrum Estimation Workshop*, Griffiths AFB, NY, pp. 243-258, 1979

[56] R. O. Schmidt, “Multiple emitter location and signal parameter estimation,” *IEEE Trans. Antennas Propag.,* vol. 34, pp. 276-280, Mar. 1986.

[57] A. Paulray, R. Roy, and T. Kailath, “Estimation of signal parameters via rotational invariance techniques – ESPRIT,” *Proc. 19th Asilomar Conf. Circuits, Syst. Comput.,* Asilmoar, CA, Nov. 1985.

[58] E. K. Walton, A. Moghaddar, and C. DeMattio, “Superresolution radar target imaging,” *Proc. 13th Meeting and Symp. Antenna Measurement Techniques Association,* Boulder, CO, pp. 12.3-12.6, Oct. 1991.

[59] J. W. Odendaal, E. Barnard, and C. W. I. Pistorious, “Two-dimensional superresolution radar imaging using the MUSIC algorithm,” *IEEE Trans. Antennas Propag.,* vol. 42, pp. 1386-1391, Oct. 1994.

[60] Y.-S. Yoon and M. G. Amin, “High-resolution through-the-wall radar imaging using beamspace MUSIC,” *IEEE Trans. Antennas Propag.,* vol. 56, pp.1763-1774, June 2008.

[61] W. Zhang, A. Hoorfar, and L. Li, “Through-the-wall target localization with time reversal MUSIC method,” *Progress Electromagnetics Research,* vol. 106, pp 75-89, 2010.

[62] J. Li and P. Stoica (editor), *MIMO Radar Signal Processing*, Hoboken, NJ: John Wiley & Sons, 2009.

[63] E. J. Candes, J. Romberg, and T. Tao, "Robust uncertainty principles: exact signal reconstruction from highly incomplete frequency information," *IEEE Trans. Inf. Theory,* vol. 52, pp. 489-509, Feb. 2006.

[64] D. L. Donoho, "Compressed sensing," *IEEE Trans. Inf. Theory,* vol. 52, pp. 1289-1306, April 2006.

[65] S. S. Chen, D. L. Donoho, and M. A. Saunders, “Atomic decomposition by basis pursuit,” *SIAM Review,* vol. 43, no. 1, pp. 129-159, 2001.

[66] J. A. Tropp, “Just relax: convex programming methods for identifying sparse signals in noise,” *IEEE Trans. Inf. Theory,* vol. 52, pp. 1030-1051, March 2006.

[67] S. Boyd and L. Vanderberghe, *Convex Optimization.* Cambridge, U.K.: Cambridge Univ. Press, 2004.

[68] G. Davis, S. Mallat, and Z. Zhang, “Adaptive time-frequency decompositions,” *Optical Engineering,* vol. 33, pp. 2183-2191, July 1994.

[69] S. Ji, Y. Xue, and L. Carin, “Bayesian compressive sensing,” *IEEE Trans. Signal Process.,* vol. 56, pp. 2346-2356, June 2008.

[70] E. J. Candes and T. Tao, "Decoding by linear programming," *IEEE Trans. Inf. Theory,* vol. 51, no. 12, pp 4203-4215, Dec. 2005.

[71] J. A. Tropp, “Greed is good: algorithmic results for sparse approximation,” *IEEE Trans. Inf. Theory*, vol. 50, pp. 2231-2242, Oct. 2004.

[72] M. Herman and T. Strohmer, "High-resolution radar via compressive sensing," *IEEE Trans. Signal Process.*, vol. 57, no. 6, pp. 2275-2284. June 2009.

[73] L. C. Potter, E. Ertin, J. T. Parker, and M. Cetin, "Sparsity and compressed sensing in radar imaging," *Proc. IEEE*, vol. 98, no. 6, pp. 1006-1020, June 2010.

[74] A. C. Gurbuz, J. H. McClellan, and W. R. Scott, "A compressive sensing data acquisition and imaging method for stepped frequency GPRs," *IEEE Trans. Signal Process.*, vol. 57, no. 7, pp. 2640-2650, July 2009.

[75] Y.-S. Yoon and M. G. Amin, "Compressed sensing technique for high-resolution radar imaging," *Proc. SPIE*, vol. 6968, pp. 69681A.1-69681A.10, May 2008.

[76] K. Browne, R. J. Burkholder, and J. L. Volakis, "Non-linear optimization methods for enhancing through-wall radar imagery forged via a portable wideband UHF array," in *Antennas and Propagation (APSURSI), 2011 IEEE International Symposium on*, pp. 2095-2098, July 2011.

[77] Q. Huang, L. Qu, B. Wu, and G. Fang, "UWB through-wall imaging based on compressive sensing," *IEEE Trans. Geosci. Remote Sens.*, vol. 48, no. 3, pp. 1408-1415, March 2010.

[78] E. J. Candes, J. K. Romberg, and T. Tao, “Stable signal recovery from incomplete and inaccurate measurements,” *Communications Pure Applied Math.*, vol. 59, no. 8, pp. 1207-1223, 2006.

[79] E. Candes and J. Romberg, l1-Magic. [Online]. Available: http://users.ece.gatech.edu/~justin/l1magic/

[80] M. Grant and S. Boyd, CVX: Matlab software for disciplined convex programming [Online]. Available: http://cvxr.com/cvx/, April 2011.

[81] E. Van Den Berg and M. P. Friedlander, SPGL1: A solver for large-scale sparse reconstruction,. [Online]. Available: http://www.cs.ubc.ca/labs/scl/spgl1, June 2007.

[82] R. Mittra and S. W. Lee, *Analytic Techniques in the Theory of Guided Waves*, New York, NY: Macmilla, 1971.

[83] H. Ling, “RCS of waveguide cavities: a hybrid boundary-integral/modal approach,” *IEEE Trans. Atennas. Propag.* vol. 38, no. 9, pp 1413-1420, Sept. 1990.

[84] T. S. Chu and T. Itoh, “Generalized scattering matrix method for analysis of cascaded and offset microstrip step discontinuities,” *IEEE Trans. Microw. Theory Tech.*, vol. 34, pp. 280-284, Feb. 1986.

[85] L. Cohen, *Time-Frequency Analysis*, Upper Saddle River, NJ: Prentice Hall PTR, 1995.

[86] P. Flandrin and P. Borgnat, “Time-frequency energy distributions meet compressed sensing,” *IEEE Trans. Signal Process*., vol. 58, pp.2974-2982, June 2010.

[87] A. Naqvi, S.-T. Yang, and H. Ling, "Investigation of Doppler features from wind turbine scattering," *IEEE Antennas Wireless Propag. Lett.*, vol. 9, pp. 485-488, 2010.

[88] K. D. Laakmann and W. H. Steier, “Waveguides: characteristic modes of hollow rectangular dielectric waveguides,” *Applied Optics,* vol. 15, pp. 1334-1340, May 1976.

[89] D. G. Dudley, “Wireless propagation in circular tunnels,” *IEEE Trans. Antenna Propag.*, vol. 53, pp. 435-441, Jan. 2005.

[90] “Report to the congressional defense committees on the effect of windmill farms on military readiness,” Office of the Director of Defense Research and Engineering, Undersecretary for Space and Sensor Systems, 2006.

[91] J. B. Sandifer, T. Crum, E. Ciardi and R. Guenther, “A way forward: wind farm-weather radar coexistence,” Windpower, Chicago, IL, May 2009.

[92] B. M. Kent, K. C. Hill, A. Buterbaugh, G. Zelinski, R. Hawley, L. Cravens, T. Van, C. Vogel and T. Coveyou, “Dynamic radar cross section and radar Doppler measurements of commercial general electric windmill power turbines part 1 – predicted and measured radar signatures,” *IEEE Antennas and Propag. Magazine*, vol. 50, no. 2, pp. 211-219, Apr. 2008.

[93] B. M. Kent, A. Buterbaugh, K. C. Hill, G. Zelinski, R. Hawley, L. Cravens, T. Van, C. Vogel and T. Coveyou, "Dynamic radar cross section and radar Doppler measurements of commercial general electric windmill power turbines part 2 – predicted and measured doppler signatures," *Proc. AMTA Symposium*, St. Louis, MO, 2007.

[94] A. Naqvi, S.-T. Yang and H. Ling, “Investigation of Doppler features from wind turbine scattering,” *IEEE Antennas and Wireless Propagat.*, vol. 9, pp. 485-488, 2010.

[95] I. J. LaHaie, “Overview of an image-based technique for predicting far field radar cross-section from near field measurements,” *IEEE Antennas Propagat. Mag.*, vol. 45, no. 6, pp. 159-169, Dec. 2003.

[96] I. J. LaHaie, C. M. Coleman and S. A. Rice, “An improved version of the circular near field-to-far field transformation (CNFFFT),” *Proc. AMTA Symp.*, pp. 196-201, Newport, RI, 2005.

[97] H.-J. Li and F.-L. Lin, “Near-field imaging for conducting objects,” *IEEE Trans. Antennas Propagat.*, vol. 39, pp. 600-605, May 1991.

[98] T. V. Thomas and T. F. Eibert, “Comparison and application of near-field ISAR imaging techniques for far-field radar cross section determination,” *IEEE Trans. Antennas Propagat.* vol. 54, pp. 144-151, Jan. 2006.

[99] D. L. Mensa and K. Vaccaro, “Near-field to far-field transformation of RCS data,” *Proc. AMTA Symp.*, pp. 155-161, Williamsburg, VA, 1995.

[100] R. Bhalla and H. Ling, "3D scattering center extraction using the shooting and bouncing ray technique," *IEEE Trans. Antennas Propagat.*, vol. 44, pp. 1445-1453, Nov. 1996.

[101] C. A. Balanis, *Antenna Theory: Appendix VIII*, John Wiley & Sons, 2005, pp. 1089-1093.

Vita

Nicholas John Whitelonis was born on April 17th 1984 in Houston, TX. He entered The University of Texas at Austin as an undergraduate in the fall of 2002. In 2007, he completed the B.S. degree in computer engineering and then the M.S. in engineering in 2009. Since 2009 he has been working towards his PhD at The University of Texas at Austin.

Permanent email: nickwhitelonis@utexas.edu

This dissertation was typed by the author.